You Must Construct Additional Hypermassive Neutron Stars

by

Steven Fahlman

A thesis submitted in partial fulfillment of the requirements for the degree of

Doctor of Philosophy

Department of Physics
University of Alberta

Abstract

We examine the long-term evolution of accretion tori around the remnants of compact object mergers and the explosions of highly magnetized massive stars to better understand their roles in the creation of optical transients and the synthesis of r-process elements. We begin by modifying the `FLASH4.5` code to evolve magnetohydrodynamics with simple neutrino transport and a realistic equation of state in 3D spherical coordinates, and provide verification tests. With this new framework, we evolve post-merger systems of tori around black holes and hypermassive neutron stars. We find that magnetic stresses, neutrino driven winds, and thermal effects eject outflows with a broad range of electron fractions, velocities and entropies, sufficient to power kilonovae and produce up to 3rd peak r-process elements. While the ejecta from our simulations cannot match the masses and velocities inferred from two component kilonova modelling of GW170817, more detailed multidimensional kilonova models are needed to see if our outflows are consistent with observations of the blue kilonova. Finally, we detail the modifications to the neutrino scheme and treatment of gravity in `FLASH4.5` necessary to run simulations of magnetorotational supernovae, along with further verification tests.

Preface

This thesis is an original work by Steven Fahlman. Chapters 2 to 5 of this thesis were published in the Monthly Notices of the Royal Astronomical Society as "Steven Fahlman, Rodrigo Fernández, Long-term 3D MHD simulations of black hole accretion discs formed in neutron star mergers, Monthly Notices of the Royal Astronomical Society, Volume 513, Issue 2, June 2022, Pages 2689–2707". For this thesis, the introduction of "Long-term 3D MHD simulations of black hole accretion discs formed in neutron star mergers" has been removed, and a new short introduction was put in its place. The appendices have been moved to Chapters 2, 3, and 4, and Chapter 5 contains the main body of text. For this paper I developed the code with Rodrigo, and ran the simulations. The main body of text was written by me, and subjected to editing by Rodrigo.

Chapters 6 and 7 were accepted by the Monthly Notices of the Royal Astronomical Society as "Steven Fahlman, Rodrigo Fernández, Sharon Morsink, Secular Outflows from 3D-MHD Hypermassive Neutron Star Accretion Disk Systems" in August 2023. Again the introduction has been rewritten, and the appendix has been moved to Chapter 6. For this paper I developed the `FLASH` code with Rodrigo, and ran the simulations. Sharon developed the `NewtNeut` code for implementing a hypermassive neutron star in Newtonian self-gravity, with a realistic equation of state. The main body of text was written by me, and edited by Rodrigo and Sharon.

Acknowledgements

You know, the real discovery of this thesis is all the friends you make along the way. Unfortunately I didn't find any, so I'd like to instead thank my supervisor, Rodrigo Fernández, for being the best supervisor a man could ask for. I'd also like to thank my wife Sophie for being my sugar mommy while I completed my studies, and my baby Rosalyn for keeping me company at 3AM while I wrote this thesis. Shoutout to my other four wives, Colemeister, Landru, SiniJi, and Ivanov the AstroSlav, who at some point probably helped me. Don't tell them though, or it'll go to their heads.

Contents

List of Tables

List of Figures

Abbreviations

BH Black Hole

CCSN Core Collapse Supernova

CT Constrained Transport

EM Electromagnetic

EOS Equation of State

FLD Flux Limited Diffusion

GR General Relativity

GRMHD General Relativistic Magnetohydrodynamics

GW Gravitational Wave

HMNS Hypermassive Neutron Star

HSCF Hachisu Self-Consistent Field

HSE Hydrostatic Equilibrium

ISCO Innermost Stable Circular Orbit

MAD Magnetically Arrested Disk

MC Monte Carlo

MHD Magnetohydrodynamics

MRI Magnetorotational Instability

MRSN Magnetorotational Supernova

NS Neutron Star

SANE Standard And Normal Evolution

TOV Tolman-Oppenheimer-Volkoff

Chapter 1

Introduction

The rapid neutron capture process, or r-process, is thought to be an astrophysical nucleosynthesis path responsible for creating about half of the heaviest elements in the universe. In the r-process, large numbers of neutrons are captured onto seed nuclei at a rate much faster than that of β-decays. This allows the seed nuclei to reach the neutron drip line, where it becomes energetically unfavourable to add more neutrons. The neutron-rich nuclei then become unstable to β-decay, increasing the ratio of protons to neutrons and allowing for additional neutron captures, creating a characteristic chain of elements built up in the r-process (Burbidge et al., 1957). The conditions for the r-process to occur depend sensitively on the neutron richness of the material, characterized by the electron fraction, the ratio of electrons to baryons in the plasma ($Y_e = n_p/[n_p + n_n]$), as well as the entropy and expansion time scale of the material (Kasen et al., 2015; Lippuner and Roberts, 2015; Cowan et al., 2021). The entropies, electron fractions and velocities of ejecta from neutron star (NS) mergers and rare energetic supernovae are thought to match the conditions for the r-process to occur, leading to them being proposed as astrophysical sites for the production of r-process elements. (Li and Paczyński, 1998; Côté et al.,

2018; Cowan et al., 2021; Siegel, 2022).

The originally envisioned site for r-process element production in NS mergers was in "dynamical ejecta" from tidal forces and shocks from the contact interface between the two stars (Li and Paczyński, 1998; Eichler et al., 1989). The dynamical ejecta has been shown though numerical simulations to unbind $\gtrsim 10^{-3}\,M_\odot$ worth of ejecta traveling at $\lesssim 0.3c$ on timescales of ms, and the majority of this ejecta channel has an electron fraction below the cutoff necessary for lanthanide creation through the r-process (See e.g., Radice et al. 2020; Perego et al. 2020; Rosswog and Korobkin 2022; Janka and Bauswein 2022 for recent reviews).

However, depending on the NS binary properties, the post-merger system is thought to be comparable to or dominate the dynamical ejecta, (Wu et al., 2016; Radice et al., 2018; Margalit and Metzger, 2019; Krüger and Foucart, 2020; Fujibayashi et al., 2020c; Nedora et al., 2021), with simulations finding ejecta masses of $\sim 10^{-2}\,M_\odot$ on a timescale of $\gtrsim$ 1s out of initially bound material that coalesced into an accretion torus. This is often referred to as "secular ejecta", or "disk winds" (See e.g. Fernández and Metzger 2016; Siegel 2019; Radice et al. 2020; Shibata and Hotokezaka 2019; Shibata et al. 2020 for recent reviews).

If the remnant in the post-merger system is a black hole (BH), a significant portion of the matter in the accretion disk is ejected as the torus evaporates on a timescale of seconds primarily via neutrino irradiation and magnetic stresses. Simulations of post-merger BH-tori have shown neutrino self-absorption and emission to be modestly important in driving mass outflows, as well as setting the electron fraction of the disk outflows through the weak interactions (e.g., Shibata and Sekiguchi 2012; Fernández and Metzger 2013; Perego et al. 2014;

Just et al. 2015). The dominant channel of secular mass ejection in the accretion torus is turbulence induced by the magnetorotational instability (Balbus and Hawley, 1991, 1992, MRI), often referred to as "thermal" ejecta. Resolving mass ejection from the MRI requires resolving the wavelength of most unstable mode of the MRI (e.g., Hawley and Balbus 1991; Duez et al. 2006) for second long timescales, in 3D to avoid suppressing the MRI dynamo (Cowling, 1933). To reduce this high computational expense, studies have utilized various different effective viscosities to mimic the effects of angular momentum transport via the MRI (e.g., Shakura and Sunyaev 1973; Stone et al. 1999; Radice 2020; Just et al. 2023). Simulations including viscous angular momentum transport and neutrino effects in BH disks have reached a broad consensus that the disk can eject $\sim 10^{-2}\,M_\odot$ of ejecta with $v \lesssim 0.05c$ and $Y_e \sim 0.2 - 0.3$ for tori with $M_t \gtrsim 3 \times 10^{-2}$ (Fernández and Metzger, 2013; Perego et al., 2014; Just et al., 2015; Foucart et al., 2020; Fernández et al., 2020; Fujibayashi et al., 2020a; Nedora et al., 2021; Just et al., 2022, 2023). However, recent MHD studies have shown that viscous simulations represent an effective lower limit on the mass and velocity of the ejecta from the post-merger system. Including magnetic fields self-consistently tends to eject a factor of two more total ejecta in BH disk setups from initial magnetized winds in addition to the thermal outflows (e.g., Hossein Nouri et al. 2018; Siegel and Metzger 2018; Fernández et al. 2019b; Christie et al. 2019; Miller et al. 2019; Hayashi et al. 2022; Just et al. 2022; Fahlman and Fernández 2022; Curtis et al. 2023b).

Alternatively, if the total mass of the merging NSs does not exceed ~ 1.5 times the maximum mass of a cold, non-rotating NS for a given equation of state (EOS), the merger can form a hypermassive NS (HMNS) supported against gravitational collapse by differential rotation and thermal pressure (Baumgarte

et al., 2000; Kaplan et al., 2014; Hanauske et al., 2017; Iosif and Stergioulas, 2022; Radice and Bernuzzi, 2023). Due to redistribution of angular momentum through magnetic winding and the MRI, as well as the loss of thermal support via neutrino emission, the HMNS will eventually collapse to a BH on a timescale of $\sim 1-100\,\mathrm{ms}$. Simulations of post-merger HMNS-disk systems have shown the HMNS can power neutrino-driven and mechanically-driven winds in axisymmetric viscous simulations (e.g., Lippuner et al. 2017; Fahlman and Fernández 2018; Shibata et al. 2021a; Fujibayashi et al. 2023; Just et al. 2023) and additional magnetized winds in full 3D (GR)MHD (Kiuchi et al., 2012; Siegel et al., 2014; Ciolfi and Kalinani, 2020; Mösta et al., 2020; de Haas et al., 2022; Kiuchi et al., 2022; Combi and Siegel, 2023; Curtis et al., 2023a). These outflows tend to be fast, with magnetized neutrino-driven winds reaching velocities of $v \gtrsim 0.25c$. The additional neutrino irradiation from the HMNS will further raise the electron fraction of the disk, and the post-merger ejecta can therefore have a broad distribution of electron fractions, $0.1 < Y_e < 0.5$, depending on the lifetime of the HMNS and the timescale of the mass ejection mechanisms as compared to the timescale of weak interactions. After the HMNS collapses, the system then resembles those of BH tori, which will continue to eject material mostly in slower thermal outflows. The secular outflows are still thought to produce r-process elements, although the exact abundances are dependent on the binary system (e.g., Nedora et al. 2021; de Haas et al. 2022; Fahlman and Fernández 2022; Curtis et al. 2023b; Fujibayashi et al. 2023).

The outflow from the NS merger produces an observable electromagnetic (EM) counterpart powered by the radioactive decay of the elements synthesized in the ejecta, known as a kilonova. Generally, ejecta with a higher fraction of lanthanides ($Y_e \lesssim 0.25$) tends to have a large opacity caused by bound-bound

and bound-free line absorption in the large quantity of open d-shells of the lanthanide and/or actinides (Kasen et al., 2013; Tanaka and Hotokezaka, 2013; Fontes et al., 2015). This results in a light curve that peaks on a timescale of days to weeks in the infrared, colloquially referred to as the "red" kilonova. Alternatively, high electron fraction ($Y_e \gtrsim 0.25$) ejecta has a much lower opacity due to the lack of lanthanide/actinides, causing a peak in the UV/optical on the timescale of hours to days, called the "blue" kilonova (Barnes and Kasen, 2013; Kasen et al., 2017; Metzger, 2017a; Villar et al., 2017b).

The first NS-NS merger with both gravitational waves and a detectable EM counterpart, GW170817, was observed to have both a red and blue kilonova (Chornock et al., 2017; Cowperthwaite et al., 2017; Drout et al., 2017; Tanaka et al., 2017; Tanvir et al., 2017), which has been naively fit with two-component kilonova models. These models infer outflows corresponding to a mass of $0.02-0.05\,M_\odot$ in red ejecta with velocity $v \sim 0.15c$ and blue ejecta with $\sim 0.02\,M_\odot$ moving at $v \gtrsim 0.20c$ (e.g., Villar et al. 2017a,b; Kawaguchi et al. 2018; Metzger 2017b), requiring both a dynamical and secular component to explain the large mass ($\gtrsim 0.04M_\odot$) in the outflows. These inferred outflows from the kilonova broadly matched predictions from simulation and analytical theory. However, the inference of a fast blue component was in contention with MHD simulations of BH-accretion disk systems left from NS mergers, assuming a prompt collapse of the remnant. In general, it was found that the disk wind in BH-tori systems is not able to drive enough mass in high electron fraction ejecta with relativistic velocities, leading many to point to the HMNS phase of the merger as necessary component for powering the blue kilonova (e.g., Metzger et al. 2018; Fahlman and Fernández 2018; Ciolfi and Kalinani 2020; Nedora et al. 2021; Curtis et al. 2023a; Combi and Siegel 2023). 3D MHD simulations of HMNS-accretion disk

systems show that the outflows tend to be bluer and faster, but due in part to the small amount of long-term simulations, there is not yet a consensus on whether or not these are able match the kilonova of GW170817 (Kiuchi et al., 2022; Curtis et al., 2023a; Combi and Siegel, 2023). However, more recent multidimensional kilonova models that include more detailed physics show that the high electron fraction disk winds powering the blue component may only be required to be massive ($0.05\,M_\odot$), but slow ($v \sim 0.05c$) depending on many factors in the kilonova model (e.g., Kawaguchi et al. 2022; Ristic et al. 2023; Bulla 2023). Self-consistent end-to-end NS merger simulations with state-of-the-art microphysics and kilonova models are a promising, but computationally expensive, way to resolve these issues (Lopez Armengol et al., 2022; Just et al., 2023; Fujibayashi et al., 2023; Kawaguchi et al., 2023).

While NS mergers remain a confirmed site of r-process nucleosynthesis from our observations of GW170817, the amount of heavy elements that they contribute to galactic abundances is still an open question. In particular, observations of the abundances of Eu and Fe in the milky way halo show an enrichment in r-process elements in young (low metallicity) stars, as well as a large scatter that is indicative of rare, high yield events. The early time enrichment is in tension with the delay time required for NS mergers to take place, but the requirement of a rare, high yield site is inconsistent with the standard neutrino driven core collapse supernovae (CCSNe) paradigm. (e.g., Qian 2000; Argast et al. 2004; Hotokezaka et al. 2018; Côté et al. 2018; Kajino et al. 2019; Cowan et al. 2021; Siegel 2022). To circumvent these issues, rare subsets of CCSNe, such magnetorotational SNe (MRSNe) are possible candidates to explain the escape of sufficient low electron fraction material from the proto-NS. In the MRSN paradigm, one of the dominant energy contributions to the explosion

comes from magnetic fields, requiring the progenitors to be fast rotating and magnetized. These seed magnetic stresses then drive or aid in the explosion, and have the potential to launch high velocity jets from the surface of the proto-NS that can escape the neutrino weak interactions, making them neutron rich enough for the r-process to occur (Winteler et al., 2012; Nishimura et al., 2017; Mösta et al., 2018; Reichert et al., 2021).

This thesis is organized as follows. Chapters 2 and 3 of this thesis will introduce the modifications to the `FLASH4.5` code, building upon the work of Fahlman (2019) to extend the MHD solver to work on non-uniform grids in 3D spherical coordinates, and provide verification tests. Chapter 4 focuses on improvements to the neutrino leakage/absorption scheme for use with more massive tori around BHs. Chapter 5 utilizes the previously described setup to simulate long term accretion disks around BHs and their ejecta in 3D MHD. We detail changes to the EOS and neutrino leakage scheme necessary for the inclusion of the HMNS in our simulations in Chapter 6, and Chapter 7 contains long term 3D MHD simulations of HMNS-accretion disk systems. Finally, Chapter 8 details our changes to the gravity solver and neutrino source terms in `FLASH4.5` for performing simulations of MRSNe, and in Chapter 9 we summarize our results.

Chapter 2

Magnetohydrodynamics on a Three Dimensional Curvilinear Mesh

Previous work has shown than using viscous parameterization of magnetic field effects is not reliable in recreating a kilonova, due to the difference in outflow properties (mass, velocity, composition) from magnetic stresses, primarily at early times (Fahlman and Fernández, 2018; Siegel and Metzger, 2018; Fernández et al., 2019b, 2020; Nedora et al., 2021). Simulations in 3D MHD with appropriate microphysics are therefore required to robustly confirm the theoretical predictions of kilonovae. We can also use this advancement to implement a HMNS instead of a reflecting boundary condition, which has associated uncertainties difficult to quantify.

It is the best practice to use a coordinate system that reflects symmetries present in the system. In the case of a NS merger, spherical coordinates are the natural choice to describe a spherical star, and for finite volume codes like

FLASH4.5, they limit the amount of angular momentum loss from numerical diffusion which occurs at a more rapid rate when the fluxes are diagonal to the cell face. The radial coordinate allows for simple implementation of a logarithmic grid, which is used to focus the resolution of a large domain on the most complex areas near the initial torus. In this way we can avoid the large overhead required by adaptive mesh refinement simulations while also limiting the computational power expended in less important outer regions of the domain. This reasoning can also be applied to other astrophysical systems, like mergers of white dwarfs and NSs, CCSNe, and BH accretion (See e.g., White et al., 2016; Fernández, 2015; Fernández et al., 2019a; Obergaulinger and Aloy, 2020)

We can also take advantage of the polar symmetries to implement a grid which is uniformly spaced in $\cos\theta$, such that the majority of polar cells are concentrated towards the midplane. This type of grid focusing has been used successfully in NS merger setups to reduce the timestep constraints that come with spherical coordinates, while once again gaining more resolution in important regions of the flow (Fernández et al., 2019b; Miller et al., 2019).

However, the use of a spherical mesh is not always advantageous due to the large timestep constraints along the polar axes. In the case of BH accretion, the large amount of magnetic flux leads to the formation of a jet in the polar regions, which without the effects of GR quickly becomes superluminal. Switching to a cylindrical mesh requires us to excise the entire cylinder below the radius corresponding to the BH horizon, which contains the inner polar regions, removing the potential for jet formation (which would be untrustworthy, given a lack of GR effects). At large radii, this will remove a small solid angle from the grid so it should not affect the outflows drastically (See e.g.,

Fujibayashi et al. 2017, 2018 for a cylindrical structured grid in GR).

In this section we expand the work done in Fahlman (2019), where we modified the default dimensionally unsplit solver (Lee, 2013) to perform hydrodynamics in 3D spherical coordinates. Now we modify the unsplit solver to solve the MHD Euler equations in each direction simultaneously by including contributions at each face from transverse and diagonal fluxes. To ensure the divergence-free evolution of magnetic fields, `FLASH4.5` solves the induction equation via the constrained transport (CT) method of Evans and Hawley (1988) on a uniform staggered mesh. We modify the default CT method to work in non-uniform 3D spherical coordinates. Furthermore, we provide the necessary modifications to make 3D cylindrical coordinates evolve correctly, building upon the work of Tzeferacos et al. (2012), and using much of the same methodology as outlined in our modifications for 3D spherical coordinates.

2.1 Governing Equations of Magnetohydrodynamics

The ideal MHD equations are those of mass, momentum and energy conservation. These can be written (without source terms) as

$$\frac{\partial \rho}{\partial t} + \vec{\nabla} \cdot [\rho \mathbf{v}] = 0, \tag{2.1}$$

$$\frac{\partial (\rho \mathbf{v})}{\partial t} + \vec{\nabla} \cdot [\rho (\mathbf{v} \otimes \mathbf{v}) - (\mathbf{B} \otimes \mathbf{B})] + \nabla P = 0, \tag{2.2}$$

$$\frac{\partial (\rho E)}{\partial t} + \vec{\nabla} \cdot [\mathbf{v}(\rho E + P) - \mathbf{B}(\mathbf{v} \cdot \mathbf{B})] = 0, \tag{2.3}$$

where ρ is the density, $\mathbf{v}$ is the vector velocity, E is the total energy, $\mathbf{B}$ is the vector magnetic fields and P is defined as the sum of gas and magnetic pressure

$$P = P_{gas} + P_{mag}, \tag{2.4}$$

$$P_{mag} = \frac{1}{2}\Big(\mathbf{B}\cdot\mathbf{B}\Big). \tag{2.5}$$

These are supplemented by the induction equation

$$\frac{\mathrm{d}\mathbf{B}}{\mathrm{d}t} + \vec{\nabla}\cdot(\mathbf{v}\otimes\mathbf{B} - \mathbf{B}\otimes\mathbf{v}) = 0, \tag{2.6}$$

where for compactness we define the tensor

$$\mathbf{J} = (\mathbf{v}\otimes\mathbf{B} - \mathbf{B}\otimes\mathbf{v}). \tag{2.7}$$

Interestingly, in `FLASH` the induction equation is actually implemented as

$$\frac{\mathrm{d}\mathbf{B}}{\mathrm{d}t} + \vec{\nabla}\cdot(\mathbf{B}\otimes\mathbf{v} - \mathbf{v}\otimes\mathbf{B}) = 0, \tag{2.8}$$

which does not affect the evolution of variables since the tensor $\mathbf{J}$ is anti-symmetric, and it is implemented self consistently. However, this does cause considerable headache[1] when implementing source terms, because the fluxes used in constructing the magnetic parts of source terms are now the explicit negative of what the documentation dictates. For the rest of this thesis, we will use the form of the induction equation in (2.8), so that we are consistent with the implementation in `FLASH` and the available literature on `FLASH`.

The conservation equations are written in terms of a vector of conserved

[1]Personal symptoms were a $\sim$3 month migraine prior to this revelation

variables, $\mathbf{U}$, a tensor of associated fluxes, $\mathcal{F}$, and a vector of source terms, $\mathbf{S}$,

$$\frac{\partial \mathbf{U}}{\partial t} + \vec{\nabla} \cdot \mathcal{F} = \mathbf{S}. \tag{2.9}$$

Writing out the associated fluxes in the radial, polar and azimuthal direction as F, G, and H respectively, we obtain

$$\frac{\partial \mathbf{U}}{\partial t} + \frac{1}{r^2}\frac{\partial (r^2 \mathbf{F})}{\partial r} + \frac{1}{r \sin\theta}\frac{\partial (\sin\theta \mathbf{G})}{\partial \theta} + \frac{1}{r \sin\theta}\frac{\partial \mathbf{H}}{\partial \phi} = \mathbf{S}. \tag{2.10}$$

The explicit form of this system is, as written to be consistent with (Lee, 2013)

$$\mathbf{U} = \begin{pmatrix} \rho \\ \rho v_r \\ \rho v_\theta \\ \rho v_\phi \\ B_r \\ B_\theta \\ B_\phi \\ \rho E \end{pmatrix}, \quad \mathbf{F} = \begin{pmatrix} \rho v_r \\ \rho v_r^2 + P - B_r^2 \\ \rho v_r v_\theta - B_r B_\theta \\ \rho v_r v_\phi - B_r B_\phi \\ 0 \\ v_r B_\theta - v_\theta B_r = -E_\phi \\ v_r B_\phi - v_\phi B_r = E_\theta \\ v_r(\rho E + P) - B_r(\mathbf{v}\cdot\mathbf{B}) \end{pmatrix},$$

$$\mathbf{G} = \begin{pmatrix} \rho v_\theta \\ \rho v_\theta v_r - B_\theta B_r \\ \rho v_\theta^2 + P - B_\theta^2 \\ \rho v_\theta v_\phi - B_\theta B_\phi \\ v_\theta B_r - v_r B_\theta = E_\phi \\ 0 \\ v_\theta B_\phi - v_\phi B_\theta = -E_r \\ v_\theta(\rho E + P) - B_\theta(\mathbf{v}\cdot\mathbf{B}) \end{pmatrix}, \quad \mathbf{H} = \begin{pmatrix} \rho v_\phi \\ \rho v_\phi v_r - B_\phi B_r \\ \rho v_\theta v_\phi - B_\theta B_\phi \\ \rho v_\phi^2 + P - B_\phi^2 \\ v_\phi B_r - v_r B_\phi = -E_\theta \\ v_\phi B_\theta - v_\theta B_\phi = E_r \\ 0 \\ v_\phi(\rho E + P) - B_\phi(\mathbf{v}\cdot\mathbf{B}) \end{pmatrix}. \tag{2.11}$$

In conservative mesh-based codes like `FLASH`, the conserved variables are evolved by discretizing (2.10) in both time and space. This means that we evolve each variable by taking a volume average over the cell, and then advance the volume-averaged variable using the corresponding fluxes at the faces. Using the indices $\{i, j, k\}$ to enumerate cells in the radial, polar, and azimuthal directions, respectively, using half integer indices to denote values at cell faces ($\pm\frac{1}{2}$), and using the index n to denote time step, the conservative system of

equations can be written concisely as

$$\mathbf{U}^{n+1} = \mathbf{U}^{n} - \frac{\Delta t}{V}\Bigg((A_{i+1/2}\mathbf{F}_{i+1/2} - A_{i-1/2}\mathbf{F}_{i-1/2}) \\ - (A_{j+1/2}\mathbf{G}_{j+1/2} - A_{j-1/2}\mathbf{G}_{j-1/2}) \\ - (A_{k+1/2}\mathbf{H}_{k+1/2} - A_{k-1/2}\mathbf{H}_{k-1/2})\Bigg) + \Delta t\langle \mathbf{S} \rangle, \tag{2.12}$$

where $A_{\{i,j,k\}\pm\frac{1}{2}}$ is the area of the cell face perpendicular to the denoted direction, V is volume of the cell, $\langle \mathbf{S} \rangle$ is the volume-averaged source term, and $\Delta t = t^{n+1} - t^{n}$ is the timestep. We have used Gauss's Law,

$$\iiint_V \vec{\nabla} \cdot \mathbf{F} \mathrm{d}V = \oiint_A \mathbf{F} \cdot \mathrm{d}\mathbf{A}, \tag{2.13}$$

to relate volume-averaged conserved variables $\langle U \rangle$ to the face-centered fluxes. To make the conservative variable update consistent with curvilinear coordinates, we compute the discretized cell face areas and volumes for arbitrarily spaced spherical cells (Fahlman, 2019).

2.2 Geometric Source Terms in Spherical Coordinates

The geometric source terms arise from taking covariant derivatives of second rank tensors, referred to as a tensor divergence. These take the physical form of fictitious forces, and only arise in vector quantities. The scalar energy and density equations therefore do not have source terms. For a tensor, T, in spherical coordinates the divergence is written as (see Fahlman 2019, or Mignone

et al. 2005 for a separate derivation)

$$\vec{\nabla} \cdot T = \begin{pmatrix} \nabla_r T \\ \nabla_\theta T \\ \nabla_\phi T \end{pmatrix}, \tag{2.14}$$

where we can define the divergences in each individual direction as

$$\nabla_r T = \left(\frac{1}{r^2} \frac{\partial (r^2 T^{rr})}{\partial r} + \frac{1}{r \sin\theta} \frac{\partial (\sin\theta T^{\theta r})}{\partial \theta} + \frac{1}{r \sin\theta} \frac{\partial T^{\phi r}}{\partial \phi} - \frac{T^{\theta\theta} + T^{\phi\phi}}{r} \right), \tag{2.15}$$

$$\nabla_\theta T = \left(\frac{1}{r^2} \frac{\partial (r^2 T^{r\theta})}{\partial r} + \frac{1}{r \sin\theta} \frac{\partial (\sin\theta T^{\theta\theta})}{\partial \theta} + \frac{1}{r \sin\theta} \frac{\partial T^{\phi\theta}}{\partial \phi} + \frac{T^{\theta r}}{r} - \frac{T^{\phi\phi}}{r} \cot\theta \right), \tag{2.16}$$

$$\nabla_\phi T = \left(\frac{1}{r^2} \frac{\partial (r^2 T^{r\phi})}{\partial r} + \frac{1}{r \sin\theta} \frac{\partial (\sin\theta T^{\theta\phi})}{\partial \theta} + \frac{1}{r \sin\theta} \frac{\partial T^{\phi\phi}}{\partial \phi} + \frac{T^{\phi r}}{r} + \frac{T^{\phi\theta}}{r} \cot\theta \right). \tag{2.17}$$

Explicitly applying the divergences (2.15)-(2.17) to the dyads in the momentum and induction equation (5.2 and 2.8) yields the source term vector in (2.9),

$$\mathbf{S} = \begin{pmatrix} 0 \\ \dfrac{\rho(v_\theta^2 + v_\phi^2) - B_\theta^2 - B_\phi^2}{r} \\ -\dfrac{\rho v_r v_\theta - B_r B_\theta}{r} + \dfrac{\cot\theta(\rho v_\phi^2 - B_\phi^2)}{r} \\ -\dfrac{\rho v_r v_\phi - B_r B_\phi}{r} - \dfrac{\cot\theta(\rho v_\phi v_\theta - B_\phi B_\theta)}{r} \\ 0 \\ \dfrac{(B_\theta v_r - B_r v_\theta)}{r} \\ \dfrac{(B_\phi v_r - B_r v_\phi)}{r} + \dfrac{(B_\phi v_\theta - B_\theta v_\phi)\cot\theta}{r} \\ 0 \end{pmatrix}. \tag{2.18}$$

For use in (2.12), these have to be volume averaged. In the absence of the framework to do this numerically in `FLASH`, we do this analytically, via

$$\langle \mathbf{S} \rangle = \frac{1}{V} \iiint_V \mathbf{S}(r,\theta) \mathrm{d}V. \tag{2.19}$$

for use in the discretized conservative update equation (2.12). Since conservative mesh schemes store hydrodynamic variables as volume averages, we make the approximation of taking them out of the integral in equation (2.19). The remaining terms contain either a r^{-1} or $\cot\theta$ dependence, which are integrated

analytically to get the volume-averaged source term vector

$$\langle \mathbf{S} \rangle = \frac{3\Delta r^2}{2\Delta r^3} \begin{pmatrix} 0 \\ \rho(v_\theta^2 + v_\phi^2) - B_\theta^2 - B_\phi^2 \\ -\rho v_r v_\theta - B_r B_\theta + \dfrac{\Delta \sin\theta}{\Delta \cos\theta}(\rho v_\phi^2 - B_\phi^2) \\ -\rho v_r v_\phi - B_r B_\phi - \dfrac{\Delta \sin\theta}{\Delta \cos\theta}(\rho v_\phi v_\theta - B_\phi B_\theta) \\ 0 \\ (B_\theta v_r - B_r v_\theta) \\ (B_\phi v_r - B_r v_\phi) + \dfrac{\Delta \sin\theta}{\Delta \cos\theta}(B_\phi v_\theta - B_\theta v_\phi) \\ 0 \end{pmatrix}. \tag{2.20}$$

We define the finite differences across the cell used above as

$$\Delta r^2 = r_{i+1/2}^2 - r_{i-1/2}^2, \tag{2.21}$$

$$\Delta r^3 = r_{i+1/2}^3 - r_{i-1/2}^3, \tag{2.22}$$

$$\Delta \cos\theta = \cos\theta_{j+1/2} - \cos\theta_{j-1/2}, \tag{2.23}$$

$$\Delta \sin\theta = \sin\theta_{j+1/2} - \sin\theta_{j-1/2}. \tag{2.24}$$

These are the source terms which are used in the update of the conserved variables (equation 2.12).

2.3 Fluxes and Primitive Variables in Spherical Coordinates

Before the conservative update (equation 2.12) can be performed, the fluxes at the face must be known. Here we provide only the information needed to adjust the reconstruction of fluxes for spherical coordinates. The discretization and methods used in `FLASH` to extend variables to the face and construct appropriate Riemann states can be found in Lee (2013). By default, `FLASH` employs a piecewise linear MUSCL-Hancock method (Colella, 1985) to reconstruct the so-called cell-centered primitive variables,

$$\boldsymbol{\mathcal{V}} = (\rho, v_r, v_\theta, v_\phi, B_r, B_\theta, B_\phi, P_{\rm gas})^T, \tag{2.25}$$

instead of the conserved variables, to the faces (See Fahlman 2019 for a comprehensive overview of the reconstruction process in `FLASH`). The corresponding primitive system of equations is derived using the chain rule to expand the divergence in the conservative system, yielding

$$\frac{\partial \rho}{\partial t} + \mathbf{v} \cdot \nabla \rho + \rho(\vec{\nabla} \cdot \mathbf{v}) = 0, \tag{2.26}$$

$$\frac{\partial \mathbf{v}}{\partial t} + (\mathbf{v} \cdot \vec{\nabla}) \cdot \mathbf{v} + \frac{1}{\rho}\nabla P = 0, \tag{2.27}$$

$$\frac{\partial \mathbf{B}}{\partial t} - \nabla \times (\mathbf{v} \times \mathbf{B}) = 0 \tag{2.28}$$

$$\frac{\partial P}{\partial t} + \mathbf{v} \cdot \nabla P + \gamma P(\vec{\nabla} \cdot \mathbf{v}) = 0. \tag{2.29}$$

The primitive system is utilized because it has a quasi-linear form, which is written out as

$$\frac{\partial \boldsymbol{\mathcal{V}}}{\partial t} + \mathbf{M}_r \frac{\partial \boldsymbol{\mathcal{V}}}{\partial r} + \mathbf{M}_\theta \frac{1}{r} \frac{\partial \boldsymbol{\mathcal{V}}}{\partial \theta} + \mathbf{M}_\phi \frac{1}{r \sin\theta} \frac{\partial \boldsymbol{\mathcal{V}}}{\partial \phi} = \mathbf{S}_p, \tag{2.30}$$

where the matrices $\mathbf{M}_r, \mathbf{M}_\theta, \mathbf{M}_\phi$ can be written as (see Lee and Deane 2009 for a full derivation)

$$\mathbf{M}_r = \begin{pmatrix} v_r & \rho & 0 & 0 & 0 & 0 & 0 & 0 \\ 0 & v_r & 0 & 0 & -B_r/\rho & B_\theta/\rho & B_\phi/\rho & 1/\rho \\ 0 & 0 & v_r & 0 & -B_\theta/\rho & -B_r/\rho & 0 & 0 \\ 0 & 0 & 0 & v_r & -B_\phi/\rho & 0 & -B_r/\rho & 0 \\ 0 & 0 & 0 & 0 & 0 & 0 & 0 & 0 \\ 0 & B_\theta & -B_r & 0 & -v_\theta & v_r & 0 & 0 \\ 0 & B_\phi & 0 & -B_r & -v_\phi & 0 & v_r & 0 \\ 0 & \gamma P & 0 & 0 & (\gamma-1)(\mathbf{v}\cdot\mathbf{B}) & 0 & 0 & v_r \end{pmatrix} \tag{2.31}$$

$$\mathbf{M}_\theta = \begin{pmatrix} v_\theta & 0 & \rho & 0 & 0 & 0 & 0 & 0 \\ 0 & v_\theta & 0 & 0 & -B_\theta/\rho & B_r/\rho & 0 & 0 \\ 0 & 0 & v_\theta & 0 & B_r/\rho & -B_\theta/\rho & B_\phi/\rho & 1/\rho \\ 0 & 0 & 0 & v_\theta & 0 & -B_\phi/\rho & -B_r/\rho & 0 \\ 0 & -B_\theta & B_r & 0 & v_\theta & -v_r & 0 & 0 \\ 0 & 0 & 0 & 0 & 0 & 0 & 0 & 0 \\ 0 & 0 & B_\phi & -B_\theta & 0 & -v_\phi & v_\theta & 0 \\ 0 & 0 & \gamma P & 0 & 0 & (\gamma-1)(\mathbf{v}\cdot\mathbf{B}) & 0 & v_\theta \end{pmatrix} \tag{2.32}$$

$$\mathbf{M}_\phi = \begin{pmatrix} v_\phi & 0 & 0 & \rho & 0 & 0 & 0 & 0 \\ 0 & v_\phi & 0 & 0 & -B_\phi/\rho & 0 & -B_r/\rho & 0 \\ 0 & 0 & v_\phi & 0 & 0 & -B_\phi/\rho & -B_\theta/\rho & 0 \\ 0 & 0 & 0 & v_\phi & 0 & -B_\phi/\rho & -B_r/\rho & 1/\rho \\ 0 & -B_\phi & 0 & B_r & v_\phi & 0 & -v_r & 0 \\ 0 & 0 & -B_\phi & B_\theta & 0 & v_\phi & -v_\theta & 0 \\ 0 & 0 & 0 & 0 & 0 & 0 & 0 & 0 \\ 0 & 0 & 0 & \gamma P & 0 & 0 & (\gamma-1)(\mathbf{v}\cdot\mathbf{B}) & v_\phi \end{pmatrix} \tag{2.33}$$

Explicitly expanding all the spatial and temporal derivatives of the conservative equations (2.1, 2.2, 2.3, 2.8) in spherical coordinates results in a source term vector for the primitive system of variables given by

$$\mathbf{S}_p = \begin{pmatrix} -\rho\left(\dfrac{2v_r + v_\theta \cot\theta}{r}\right) \\ \dfrac{(v_\theta^2 + v_\phi^2) - (B_\theta^2 + B_\phi^2)/\rho}{r} \\ -\dfrac{v_r v_\theta - B_r B_\theta/\rho}{r} + \dfrac{\cot\theta(v_\phi^2 - B_\phi^2/\rho)}{r} \\ -\dfrac{v_r v_\phi - B_r B_\phi/\rho}{r} - \dfrac{\cot\theta(v_\phi v_\theta - B_\phi B_\theta/\rho)}{r} \\ -\dfrac{\cot\theta(B_\theta v_r - B_r v_\theta)}{r} \\ -\dfrac{(B_\theta v_r - B_r v_\theta)}{r} \\ \dfrac{(B_\phi v_r - B_r v_\phi)}{r} \\ -c_s^2\rho\left(\dfrac{2v_r + v_\theta \cot\theta}{r}\right) \end{pmatrix}, \tag{2.34}$$

where $c_s = P/\rho$ is the local sound speed. These are the source terms implemented in the reconstruction of cell centered variables to the faces.

2.4 Constrained Transport

Magnetic fields require an update method different from conserved quantities, as the induction equation does not explicitly require that the solenoidal constraint,

$$\vec{\nabla} \cdot \mathbf{B} = 0, \tag{2.35}$$

is satisfied. To satisfy this constraint, fields are taken to be averaged over cell faces, and the induction equation is written as

$$\iint \frac{\partial \mathbf{B}}{\partial t} \cdot \mathrm{d}\mathbf{A} = \iint -\nabla \times \mathbf{E} \cdot \mathrm{d}\mathbf{A}. \tag{2.36}$$

Applying Stokes' Theorem and using the definition of the magnetic fields as area averages, we get that

$$\frac{\partial \mathbf{B}}{\partial t} \cdot \mathbf{A} = -\oint \mathbf{E} \cdot \mathrm{d}\boldsymbol{\ell}. \tag{2.37}$$

We can further discretize the line integral as a sum, and we arrive at the Newtonian form of CT (Evans and Hawley, 1988)

$$\mathbf{B} \cdot \mathbf{A} = -\frac{\Delta t}{2} \sum_{\text{edges}} \mathbf{E} \cdot \Delta\boldsymbol{\ell}. \tag{2.38}$$

To perform the summation, we need the electric fields around each edge of the cell. These are found by Taylor expanding the face centered electric fields, which are obtained from the fluxes of conserved magnetic variables (equation 2.11) in the reconstruction step, and using Ohm's law in ideal MHD

$$\mathbf{E} = -\mathbf{v} \times \mathbf{B}. \tag{2.39}$$

Each flux contains 2 electric fields, one in each transverse direction. At each edge there will be 4 independent fluxes that can be used to find the electric field at that point (Figure 2.1 shows two of the fluxes) Conventionally, all 4 contributions are included, which can be numerically unstable (e.g., Tóth 2000; Mignone and Del Zanna 2020). Fortunately, `FLASH` includes an option to only use the upwind fluxes (flux vectors which have a positive mass flux) to

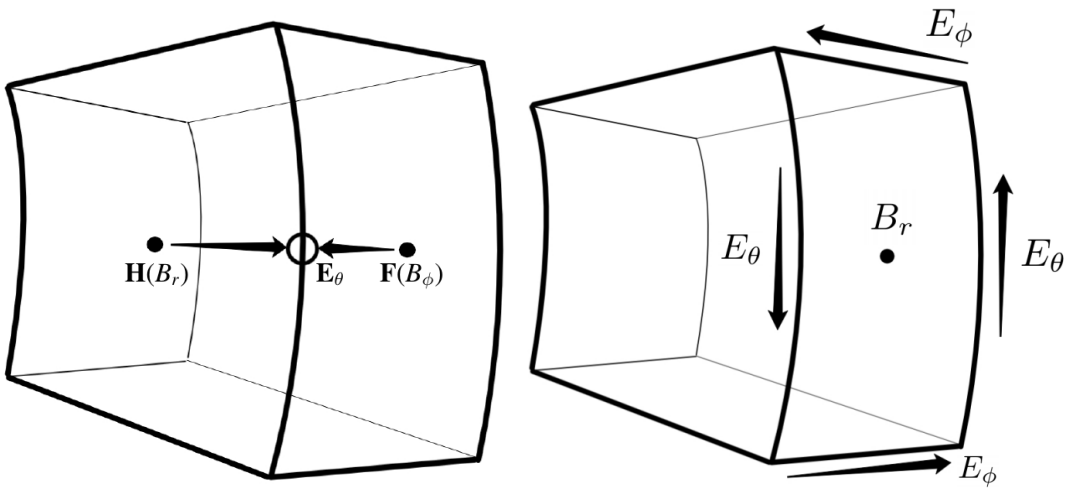

Figure 2.1: *Left:* Schematic representation of the method to obtain the electric field at cell edges for the CT method (equation 2.38). The electric fields at cell faces are obtained using Ohm's law in ideal MHD (equation 2.39) from the magnetic fluxes at the face (solid black circles). The electric fields are then Taylor-expanded to the cell edge using finite derivatives (equations [2.41]-[2.42]). The expanded values are then averaged using upwinding for numerical stability (open circle, see text). Two additional symmetric expansions to the same edge have been left out for visual clarity. *Right:* Schematic description of the reconstruction of the face-centered radial magnetic field by adding up the total contribution from electric fields along each of the cell edges (equation 2.38).

construct the electric fields (e.g., White et al. 2016). We find that this upwinded method is necessary to preserve numerical stability when using `FLASH` to evolve a magnetized torus in 3D spherical coordinates, despite not being a default option. This is also found by Kuroda et al. (2020), who note that in the regions of their core-collapse supernova setup where matter is supersonically advecting (analogous to the torus), the upwind method is necessary for stability. While no additional work is needed to implement the upwinding in spherical coordinates, the Taylor expansion for expanding the face fluxes to cell edges must be updated to account for non-uniform grid spacing. The Taylor expansion uses second-order finite differences to determine the approximate value at face edges. For example, the expansion in an arbitrary $i^{\rm th}$ direction is

$$E_{i\pm\frac{1}{2},j,k} = E_{i,j,k} \pm \Delta\ell_{i\pm\frac{1}{2}} \frac{\partial E}{\partial \ell} + (\Delta\ell_{i\pm\frac{1}{2}})^2 \frac{1}{2} \frac{\partial^2 E}{\partial \ell^2}, \tag{2.40}$$

where $\Delta\ell_{i\pm1/2}$ corresponds to the distance from the center of the cell to the $i^{\rm th}$ face. Writing the spatial derivatives as cell-centered finite differences, where $\Delta\ell_\pm$ is the distance from the center of the cell i to the cell centers above and below $(i \pm 1)$, yields

$$\frac{\partial E}{\partial \ell} = \frac{E(\ell + \Delta\ell_+) - E(\ell - \Delta\ell_-)}{\Delta\ell_+ + \Delta\ell_-} \tag{2.41}$$

$$\frac{\partial^2 E}{\partial \ell^2} = \frac{\dfrac{E(\ell + \Delta\ell_+) - E(\ell)}{\Delta\ell_+} - \dfrac{E(\ell) - E(\ell - \Delta\ell_-)}{\Delta\ell_-}}{\Delta\ell_- + \Delta\ell_+}. \tag{2.42}$$

For uniform spacing, $\Delta\ell_+ = \Delta\ell_- = \Delta\ell$, and the first and second order deriva-

tive finite differences simplify to

$$\frac{\partial E}{\partial \ell} = \frac{E(\ell + \Delta\ell) - E(\ell - \Delta\ell)}{2\Delta\ell} \tag{2.43}$$

$$\frac{\partial^2 E}{\partial \ell^2} = \frac{E(\ell + \Delta\ell) - 2E(\ell) + E(\ell - \Delta\ell)}{2(\Delta\ell)^2}. \tag{2.44}$$

Since the public version of `FLASH` only supports a uniform grid, the equations in the code (2.43-2.44) must be modified so that the more general case (2.41-2.42) is used for non-uniform grid spacing. Once the electric field construction is complete, the magnetic fields are updated every half timestep with equation (2.38) by adding up electric fields around the cell faces (Figure 2.1).

2.5 Cylindrical Mesh

Cylindrical coordinates in 2D are implemented as a Cartesian Grid in `FLASH`. The one thing which changes is the addition of source terms (See Tzeferacos et al. (2012) for the full implementation details). To extend cylindrical coordinates to include the ϕ direction, minor changes must be made to the code. However, most of these changes are covered in our implementation of spherical coordinates in a very general manner (e.g., calling for face areas determined at runtime by the selected geometry). Dimensionally correct cell lengths must also be passed to the MHD reconstruction and CT routines (e.g., passing $R\Delta\phi$ for the third coordinate. We provide no explicit tests of the functionality for 3D cylindrical coordinates, but have used it to evolve a 3D cylindrical torus as consistency check without noting any numerical artifacts.

Chapter 3

Tests of MHD in FLASH4.5

In order to demonstrate the accuracy of our extension of the unsplit MHD module to non-uniform 3D spherical coordinates, we present the results of two strong MHD tests: a magnetized blast wave and a magnetized accretion torus. Although neither of these tests has an analytic solution, we compare our results numerically to those obtained with the well-tested cartesian and cylindrical MHD implementations in FLASH4.5. In all of our spherical setups, we use a grid that is evenly spaced in $\cos\theta$ in the polar direction to increase our timestep in the polar regions. All tests use an HLLD Riemann solver and the piecewise linear reconstruction method.

3.1 Magnetized Blast Results

The magnetized blast wave is an extension of the classic hydrodynamic Sedov blast wave to MHD (e.g., Komissarov 1999). An initially overpressurized region $P \sim 500\,\mathrm{erg\,cm^{-3}}$ encompassing a few cells at the inner boundary ($r < 0.125\,\mathrm{cm}$) is allowed to expand into a uniform lower pressure $P = 1\,\mathrm{erg\,cm^{-3}}$ medium. The domain is initialized with uniform density $\rho = 1\,\mathrm{g\,cm^{-3}}$, as well

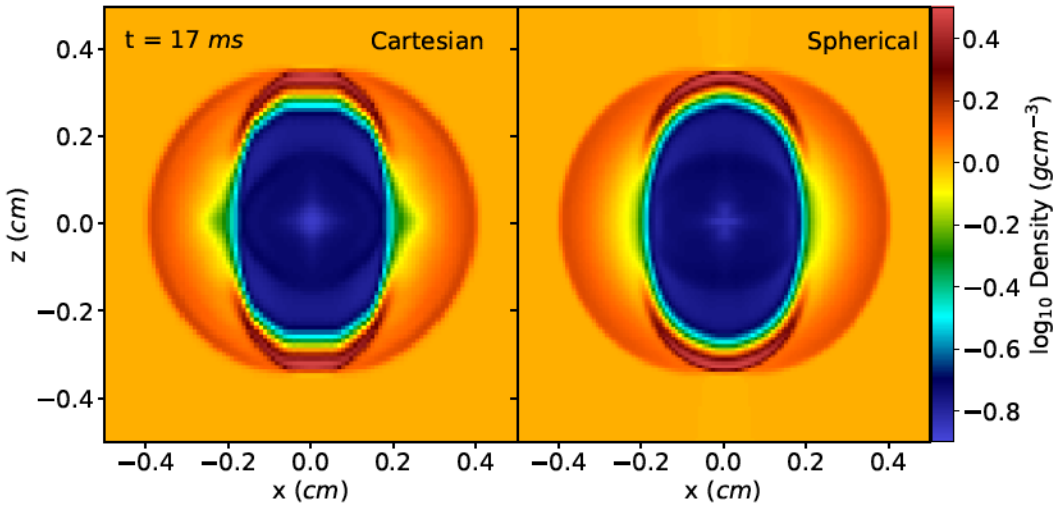

Figure 3.1: Density slice at 17 ms in xz-plane of the 3D MHD blast wave in Cartesian (left) and spherical (right) coordinates. A slice along the z-direction is shown in Figure 3.2.

as a uniform magnetic field in the cartesian $x-$direction. Due to magnetic tension, expansion of the blast wave is inhibited in the direction parallel to the x-axis, resulting in an asymmetric explosion. We use a dynamically important initial magnetic field strength, $B_0 = 10\,\mathrm{G}$, to test the code in highly magnetized regions. We perform the blast in both 3D cartesian and 3D spherical coordinates.

Both simulations produce the same overall expansion of the blast-wave, as shown in Figure 3.1. The only large quantitative difference occurs at the origin, where the reflecting inner radial boundary condition causes small differences in magnetic field evolution. In the cartesian explosion, the field is continuous across $x = 0$ and not reflecting. In `Athena++`, Skinner and Ostriker (2010) perform an off-center explosion to remove this difference, but we choose not to do so here due to the large resolution requirements. Also, an off-center explosion does not take advantage of the symmetry of the coordinate system. The cartesian test also shows visible edges, which can be attributed to the

shock being steeper in the spherical geometry.

We numerically compare a slice along the Cartesian $z-$direction in Figure 3.2. The two differences described previously are also noticeable in these plots, especially in the magnetic field at the inner boundary. However, both codes track the shock position identically, and the only noticeable differences appear at sharp gradients.

3.2 Magnetized Torus Results

We perform two torus tests. The first is carried out in 2.5D in both cylindrical and spherical coordinates, and employs a standard and normal evolution (SANE) initial magnetic field configuration. Results can be compared to multiple previous implementations (Hawley, 2000; Mignone et al., 2007; Tzeferacos et al., 2012). The second test is the extension to 3D spherical coordinates of the same SANE torus.

We set up the tori as in Fahlman (2019), using the gravitational potential of (Paczyński and Wiita, 1980) and setting the gravitating mass, $M = 1$. We normalize units such that $G = c = 1$. We choose the same parameters as model GT1 from Hawley (2000), which creates a thin, constant angular momentum torus with a maximum density of 10 and an orbital timescale of ~ 50 at the initial circularization radius $r_{\rm circ} = 4.7$, and a minimum radius of $r = 3$. The initial vector potential follows the density distribution,

$$A_\phi = \max(\rho - \frac{1}{2}\rho_{\rm max}, 0), \tag{3.1}$$

which creates poloidal field loops threaded well within the torus. Initially, the field is normalized to $\langle\beta\rangle = 100$, so the field is dynamically unimportant and

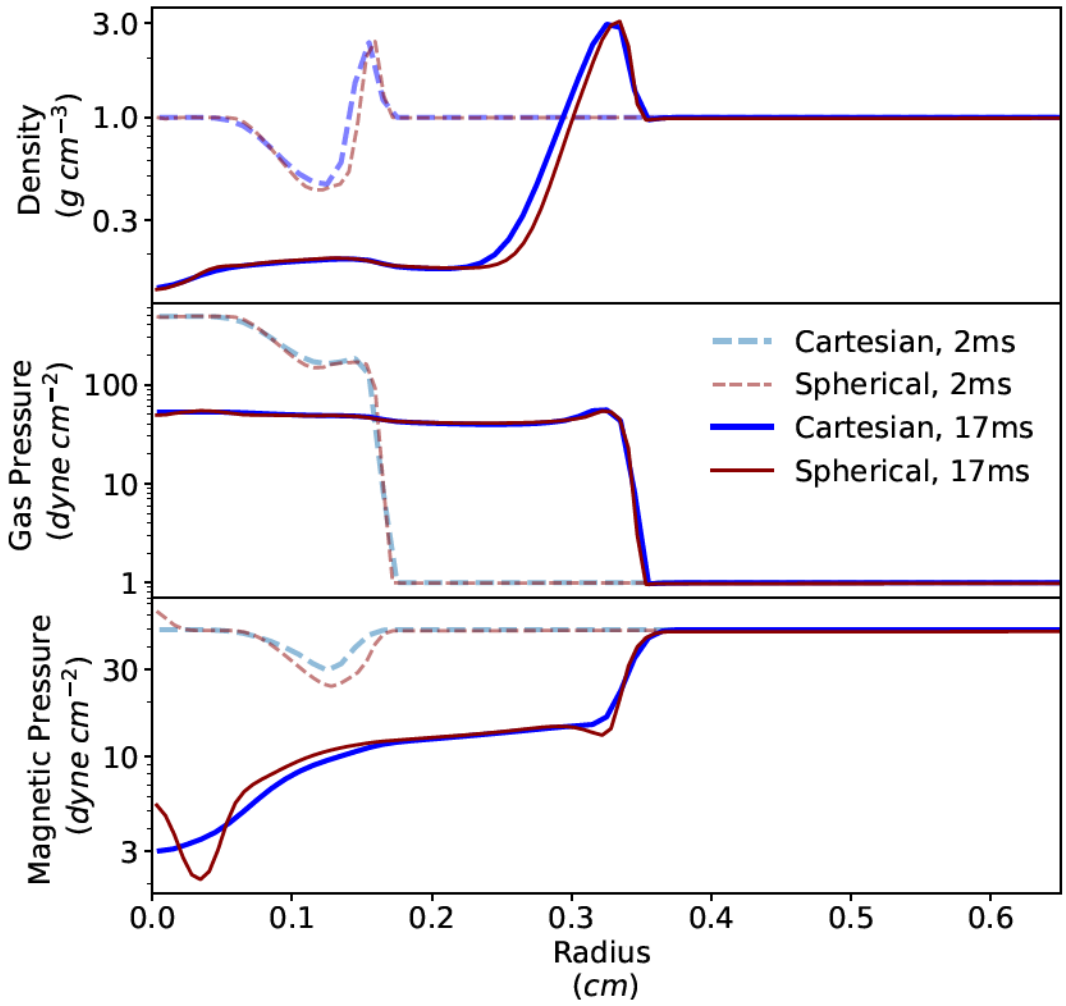

Figure 3.2: Density slices along the $z-$direction ($x = 0$, $y = 0$) in the 3D MHD blast wave test, with geometries and times as labeled (see also Figure 3.1). Notable differences appear in the magnetic pressure throughout the entire evolution due to the difference in boundary conditions between the two simulations. Other differences can be attributed to the geometry and resolution.

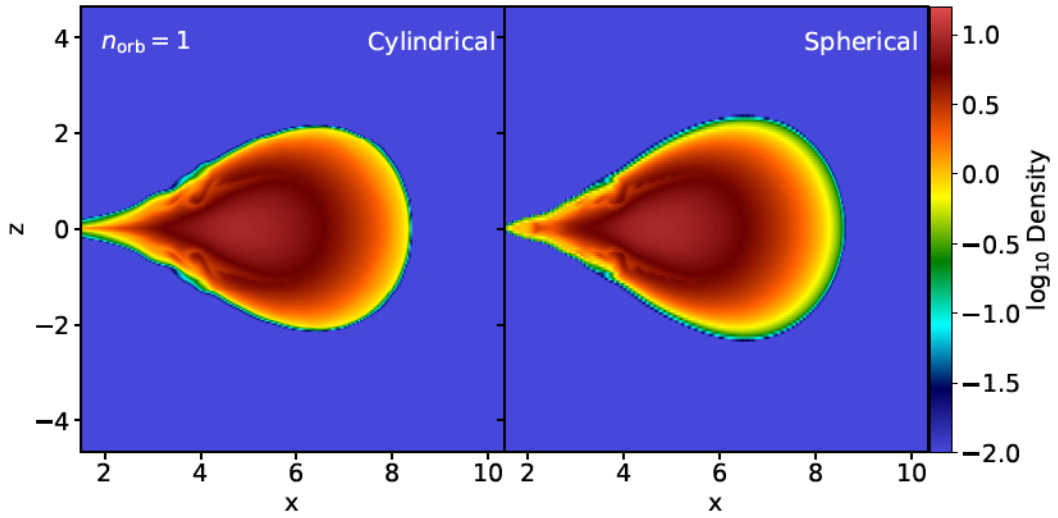

Figure 3.3: Density snapshot of the 2.5D axisymmetric torus test after one orbit at the initial density peak radius. The density field in cylindrical (left) and spherical (right) coordinates is normalized to code units, with a maximum value of 10. Noticeable differences appear in regions near the origin, where the flow is slightly more resolved in spherical coordinates.

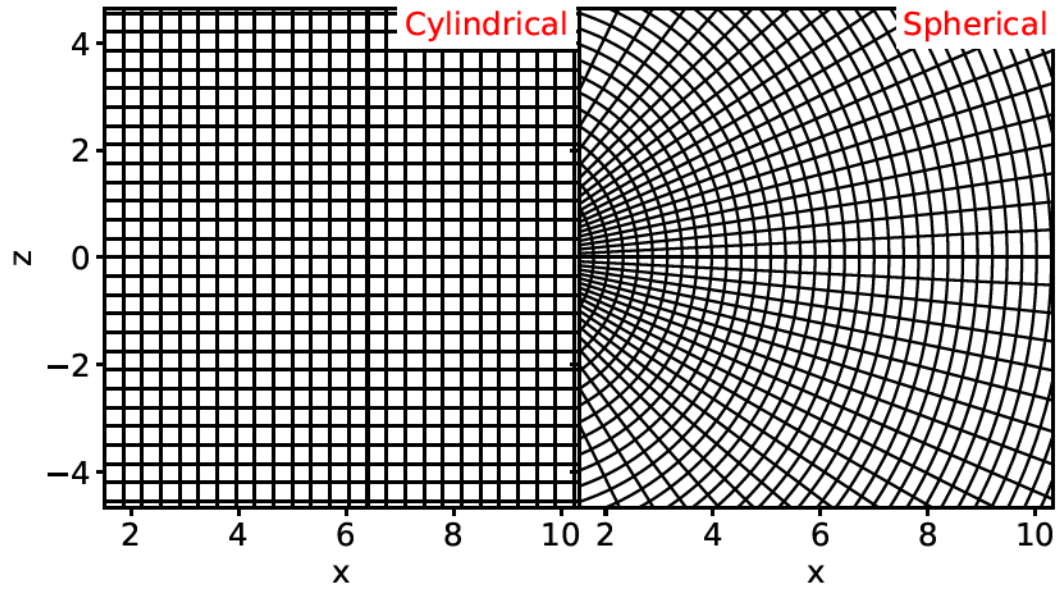

Figure 3.4: Comparison of the grid setup in cylindrical and spherical coordinates for the 2.5D torus test runs. Every 10^{th} grid line is plotted for visual clarity. The spherical grid is more resolved towards the inner radial part of the midplane, but at comparable resolutions in the rest of the torus. The outer polar regions are less resolved to reduce constraints on the simulation time step.

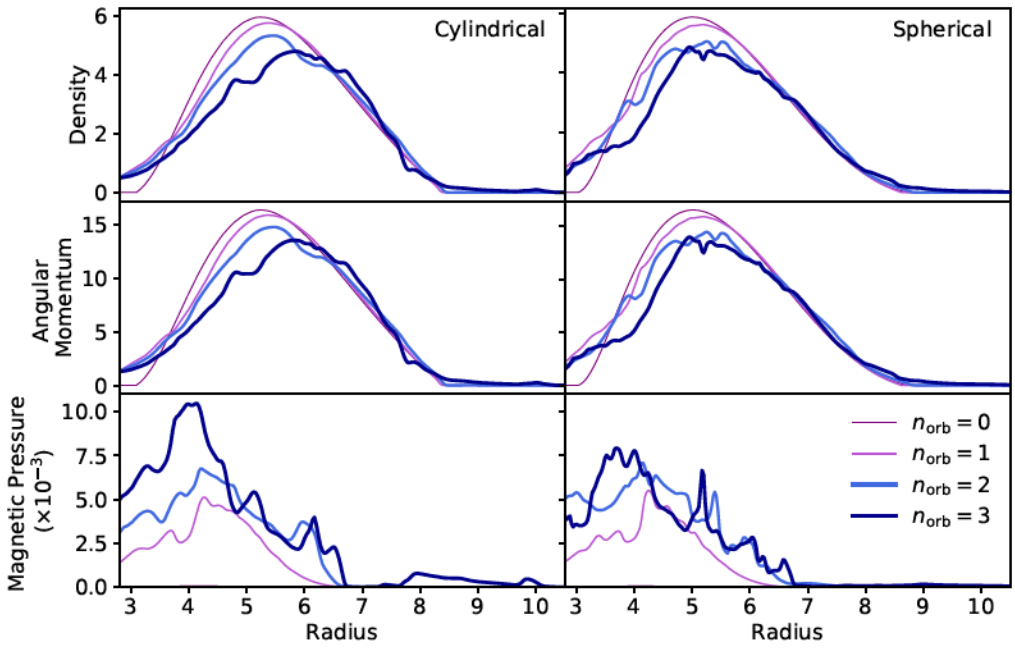

Figure 3.5: Results from the 2.5D axisymmetric torus tests, evolved for 3 orbits at the initial radius of maximum density $r_{\rm circ}$. The left column shows the height-averaged density, angular momentum, and magnetic pressure (all in code units) in the cylindrical simulation, while the right column shows the same quantities for the spherical case but angle-averaged instead. Lines of increasing thickness show the torus evolution from its initial to final state at each orbit ($n_{\rm orb}$). Numerical differences between the angle- and height-averaging appear even at the 0th orbit, but the general trends are not affected.

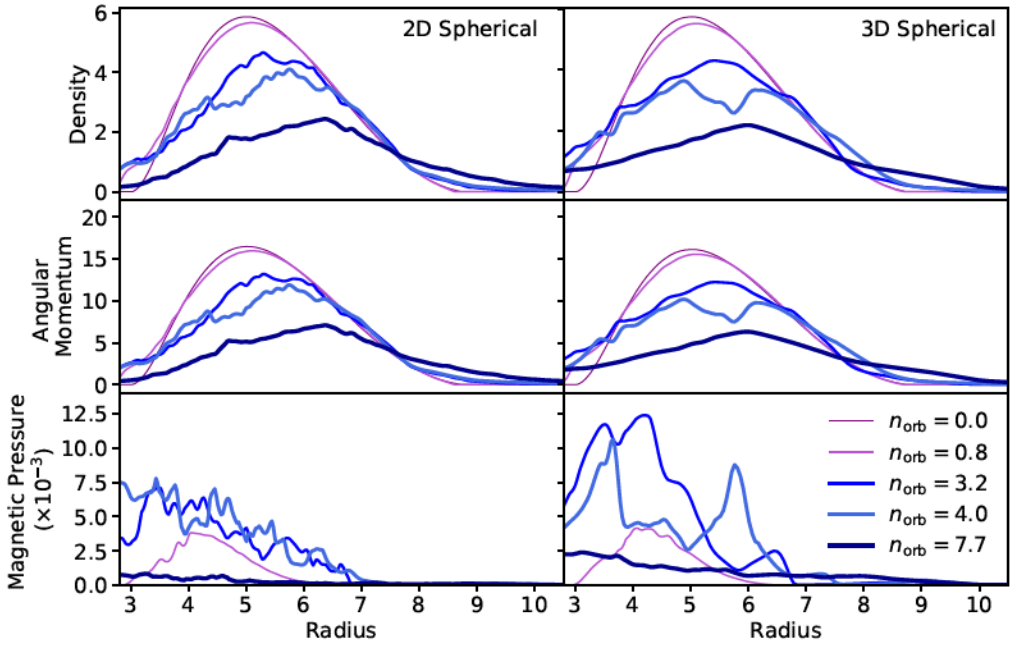

Figure 3.6: Comparison between the 2.5D axisymmetric and 3D torus test in spherical coordinates, showing the same angle-averaged quantities as in Figure 3.5 at various times. Both runs follow the expected evolution: the 3D torus sustains a more powerful MRI for a longer time due to the additional azimuthal turbulence, with the evolution being otherwise identical during the first ∼2 orbits. Differences in spatial resolution manifest as smoother profiles in the 3D runs, which has coarser cell sizes.

does not disturb the equilibrium condition. The tori are then evolved for a total of ~ 3 orbits at $r_{\rm circ}$.

We compare the evolution of hydrodynamic variables in the 2.5D runs quantitatively and qualitatively in Figures (3.3-3.5). One notable difference between the two axisymmetric runs is the resolution and the inner boundary. In cylindrical coordinates, the entire inner $z-$boundary is set to be absorbing, while in spherical coordinates the inner radial boundary is set to be absorbing, and the polar boundaries are reflecting. This affects the dynamics near the inner edges of the torus, which is noticeable in the magnetic fields. The resolution in the two runs is comparable, but not exactly the same as necessitated by

the difference in grid structures. The spherical run resolves the torus better, with $\Delta r = 0.028$ and the highest angular resolution in the midplane, $r_{\rm circ} \min(\Delta\theta) = 0.024$, resulting in nearly square cells at that location, compared to the constant cylindrical resolution of $\Delta r_{\rm cyl} = 0.035$ and $\Delta z = 0.035$. The two grids are shown in Figure 3.4 for reference.

The axisymmetric runs follow the same qualitative evolution in cylindrical and spherical coordinates: the azimuthal magnetic field grows due to winding, and the magnetic pressure causes the torus to expand and accrete. The radial angular momentum profile flattens as matter approaches the ISCO, and the magnetic field grows largest in the central regions and then accretes, frozen in with the mass flow. The first large divergences between the two simulations begin to appear in the magnetic field after ~ 1 orbit at $r_{\rm circ}$, when the accretion stream reaches the inner boundary. Feedback from the reflecting boundary changes the expansion of the torus into the ambient between the two cases. Furthermore, additional turbulent structures manifest in the spherical torus, noticeable as less smooth profiles in Figure 3.5. We attribute this in part to the differences in spatial resolution, and also note that Mignone et al. (2007) see similar effects in their `PLUTO` code tests with spherical and cylindrical coordinates and the exact same setup (see their Figure 8).

The 3D SANE torus follows the same evolution as the axisymmetric spherical case for the first few orbits, as shown in Figure 3.6. Notable differences begin to appear after $\sim$3 orbits at $r_{\rm circ}$, as the MRI begins to die down in the axisymmetric run. In 3D, the MRI creates stronger magnetic fields and is sustained for longer through the additional turbulence in the azimuthal direction (Hawley, 2000). The profiles in the 3D run appear smoother, as we run it with a lower resolution than in the 2D case due to computational limitations. To

make up for this difference in resolution, we use a logarithmic grid in radius in the 3D model, so that the region containing the torus is still resolved well. This corresponds to resolutions in the radial, polar, and azimuthal directions being $\Delta r_{\rm circ} \sim 0.040$, $r_{\rm circ} \min(\Delta\theta) = 0.10$, and $\Delta\phi = 0.03$.

Chapter 4

Neutrino Transport

In compact object mergers, neutrino interactions are essential processes to take into account. They provide additional energy to the system, which can either dominantly drive outflows in the case of a long-lived remnant or subdominantly contribute to the energy budget of outflows for prompt collapse (Dessart et al., 2009; Fernández and Metzger, 2013; Metzger and Fernández, 2014; Perego et al., 2014; Just et al., 2015; Lippuner et al., 2017; Fahlman and Fernández, 2018). Importantly, they change the composition of mass outflows, mainly through the weak interactions,

$$p + e^- \longleftrightarrow n + \nu_e, \tag{4.1}$$

$$n + e^+ \longleftrightarrow p + \bar{\nu_e}. \tag{4.2}$$

A common approach to modeling neutrinos is the so-called "leakage-scheme" of Ruffert et al. (1996), which approximates neutrino losses at minimal computational cost by using analytic approximations to Boltzmann transport. These sorts of schemes have been shown to be robust in capturing the main effects of neutrinos on the dynamics and composition of post-merger tori around compact

objects, especially BHs where they are subdominant energy sources, (Foucart et al., 2019; Fernández and Metzger, 2013; Fernández et al., 2019b; Siegel et al., 2019). However, significant differences appear when compared quantitatively to more advanced Monte-Carlo or two-moment (M1) schemes (Richers et al., 2015; Foucart et al., 2015; Perego et al., 2016; Ardevol-Pulpillo et al., 2019; Radice et al., 2022). For this reason it is necessary to make impovements to the previous leakage-scheme implemented in `FLASH` (Fernández and Metzger, 2013; Metzger and Fernández, 2014), while retaining computational efficiency.

4.1 Leakage Overview

The key components of a leakage scheme are the two source terms that describe the effective neutrino energy and number loss rate per unit volume for each neutrino species,

$$Q^{\rm eff}_{\nu_i} = Q_{\nu_i}\chi_{\nu_i,E}, \tag{4.3}$$

$$R^{\rm eff}_{\nu_i} = R_{\nu_i}\chi_{\nu_i,N}, \tag{4.4}$$

where i represents a species (ν_e or $\bar{\nu}_e$ in our scheme), the subscripts E and N refer to energy and number, respectively. Q and R are the energy and number production rates per unit volume, respectively, which are obtained from analytic expressions (Ruffert et al., 1996). The scaling factors $\chi_{\nu_i,E}$ and $\chi_{\nu_i,N}$ interpolate between the free-streaming and optically thick (diffusive) regimes for neutrinos in both energy and number,

$$\chi_{\nu_i,\{E,N\}} = \left(1 + \frac{t^{\rm diff}_{\nu_i,\{E,N\}}}{t^{\rm loss}_{\nu_i,\{E,N\}}}\right)^{-1}, \tag{4.5}$$

where $t_{\nu_i}^{\rm diff}$ and $t_{\nu_i}^{\rm loss}$ are the diffusion and loss timescales for each species, respectively. The source terms for equations (5.3)-(5.4) are then obtained as follows

$$Q_{\rm net} = Q_{\nu_e}^{\rm eff} + Q_{\bar{\nu}_e}^{\rm eff} + Q_{\rm abs} \tag{4.6}$$

$$\Gamma_{\rm net} = \frac{m_n}{\rho}\left(R_{\nu_e}^{\rm eff} + R_{\bar{\nu}_e}^{\rm eff}\right) + \Gamma_{\rm abs}, \tag{4.7}$$

where $Q_{\rm abs}$ and $\Gamma_{\rm abs}$ are the contributions from neutrino absorption (treated separately) and m_n is the neutron mass. The diffusion and loss timescales in equation (4.5) are central to the accuracy of the scheme, and thus we will discuss them in more detail.

4.1.1 Loss timescale

Once the direct energy and number production rates in (4.3-4.4) are found, the loss times are obtained as

$$t_{\nu_i,E}^{\rm loss} = \frac{Q_{\nu_i}}{E_{\nu_i}} \tag{4.8}$$

$$t_{\nu_i,N}^{\rm loss} = \frac{R_{\nu_i}}{N_{\nu_i}}, \tag{4.9}$$

where E_{ν_i} and N_{ν_i} are the neutrino energy density and number density, respectively. These quantities are obtained using analytic fits to Fermi integrals from Takahashi et al. (1978).

4.1.2 Diffusion timescale

The diffusion timescale is approximately given by

$$t^{\rm diff}_{\nu_i,\{E,N\}} \sim \frac{3\kappa_{\nu_i,\{E,N\}} d^2}{c}. \tag{4.10}$$

where $\kappa_{\nu_i,\{E,N\}}$ is the energy or number opacity for species i, and d is a characteristic diffusion distance. A more accurate expression involves calculation of the optical depth in various directions, which many leakage schemes incorporate (e.g., Rosswog and Liebendörfer 2003), but which is a global calculation that is computationally expensive. Our previous leakage implementation (Fernández and Metzger, 2013; Metzger and Fernández, 2014) approximates d as the pressure scale height assuming hydrostatic equilibrium in the cylindrical z-direction, which is the preferential direction for neutrinos to escape the torus,

$$d \approx \frac{P}{\left(\frac{\partial P}{\partial r}\right)} = \frac{P}{\rho|\cos\theta g|}. \tag{4.11}$$

This is a local calculation which yields a neutrino optical depth correct to within a factor of ~ 2.

Recently, Ardevol-Pulpillo et al. (2019) have developed a novel method for determining the diffusion timescale which is local (computationally efficient) and accurate. In this method, the diffusion timescale is determined from the diffusion equation using a flux limiter

$$\frac{\partial\{E,N\}_{\nu_i}}{\partial t} = -\vec{\nabla}\cdot\mathbf{F}_{\nu_i,\{E,N\}} \tag{4.12}$$

where $\mathbf{F}_{\nu_i,\{E,N\}}$ is the neutrino energy of number flux, respectively. In flux-limited diffusion (FLD, see e.g., Wilson et al., 1975; Levermore and Pomraning,

1981; Kolb et al., 2013), the flux is given by

$$\mathbf{F}_{\nu_i,\{E,N\}} = -\frac{c}{3\kappa_{\nu_i}}\Lambda_{\nu_i,\{E,N\}}\nabla\{E,N\}_{\nu_i}, \tag{4.13}$$

where $\Lambda_{\nu_i,\{E,N\}}$ is a flux limiter that interpolates between pure diffusion ($\Lambda_{\nu_i,\{E,N\}} = 1$) and free-streaming ($F_{\nu_i,\{E,N\}} = c\{E_{\nu_i}, N_{\nu_i}\}$). The diffusion times can be determined analogously to the loss timescales:

$$t^{\text{diff}}_{\nu_i,\{E,N\}} = \frac{\{E,N\}_{\nu_i}}{\left(\frac{\partial\{E,N\}_{\nu_i}}{\partial t}\right)}. \tag{4.14}$$

Expanding out the time derivative using the diffusion equations (4.13) and energy/number transport (4.12) yields

$$t^{\text{diff}}_{\nu_i,\{E,N\}} = \frac{\{E,N\}_{\nu_i}}{\vec{\nabla}\cdot(\frac{-c}{3\kappa_{\nu_i}}\Lambda_{\nu_i,\{E,N\}}\nabla\{E,N\}_{\nu_i})}. \tag{4.15}$$

We follow Ardevol-Pulpillo et al. (2019) in using the flux limiter of Wilson et al. (1975) for each species,

$$\Lambda_{\nu_i,\{E,N\}} = \left(1 + \frac{1}{3\kappa_{\nu_i}}\frac{|\nabla\{E,N\}_{\nu_i}|}{\{E,N\}_{\nu_i}}\right)^{-1}, \tag{4.16}$$

In contrast to Ardevol-Pulpillo et al. (2019) who integrate quantities over the neutrino distribution, we use energy-averaged (over a Fermi-Dirac distribution) opacities, energy densities, and number densities in equation (4.15), computing only the spatial gradient.

4.2 Implementation in FLASH4.5

We extend the leakage and light bulb absorption scheme of Fernández and Metzger (2013) and Metzger and Fernández (2014) by computing the diffusion time with equation (4.15) and implement it in FLASH4.5. Neutrino energy and number gradients are obtained using second order finite differences in each spatial direction. The flux limiters are calculated for each species as in (4.16). The flux limiters are then combined with the gradients, energy/number densities, and opacities to form the fluxes in 4.13. The fluxes are then linearly interpolated to the cell faces, such that we can take a numerical divergence using Gauss's theorem (2.13) and the face areas of a given cell, analogous to the unsplit update in §2.1.

4.2.1 Comparison with 2D hydrodynamic simulations

We test the effect of the new diffusion time on the long-term disk evolution by running a 2D axisymmetric hydrodynamic simulation of an accretion torus using the previous leakage scheme and the new one. A full description of the methodology is available in Fernández and Metzger (2013); Metzger and Fernández (2014), here we briefly describe the initial setup. The compact object is a BH with mass $3M_{\odot}$, and the orbiting equilibrium torus is chosen to be optically thin with a mass of $0.03M_{\odot}$. The entropy, electron fraction, and torus distortion parameter are chosen to be $8\,k_{\rm B}$/baryon, 0.1, and 1.911, respectively. This yields a well-studied initial condition compatible with dynamical merger simulations (Fernández and Metzger, 2013; Metzger and Fernández, 2014; Richers et al., 2015; Lippuner et al., 2017). Angular momentum transport is handled with the viscous stress parameterization of Shakura and Sunyaev (1973), with α set to 0.05. The tori are evolved for 1 second.

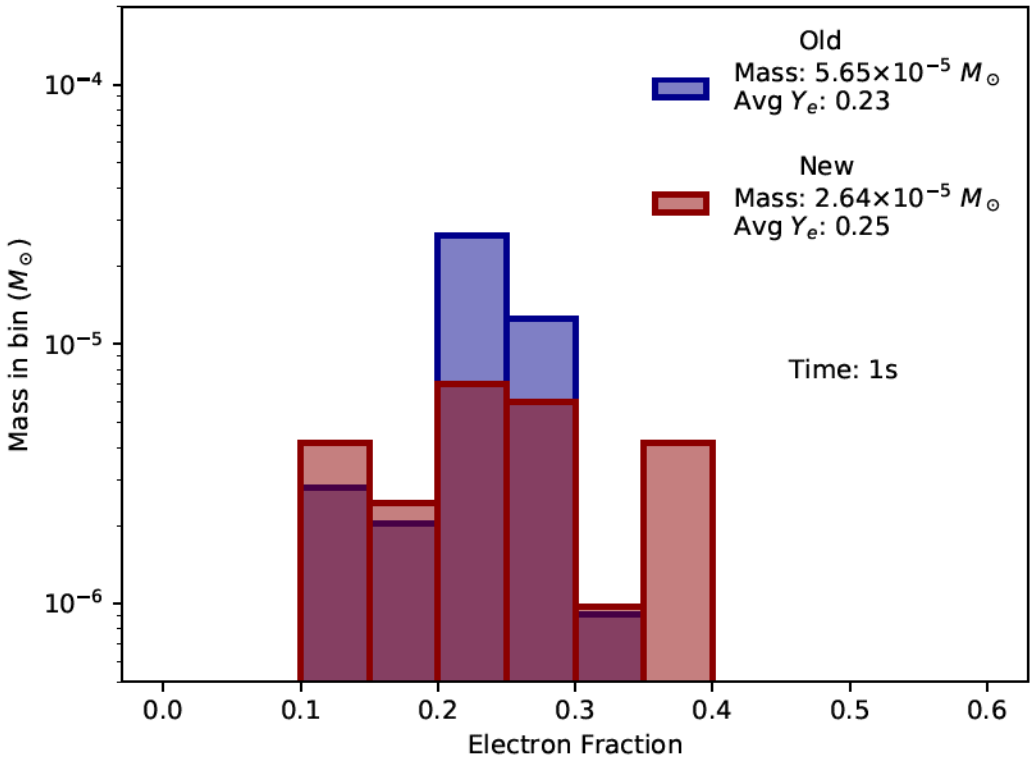

Figure 4.1: Outflow mass histogram as a function of electron fraction after 1 s of evolution from two axisymmetric hydrodynamic BH disk setups that employ the old and new implementation of diffusion time in the neutrino leakage scheme (equations 4.10-4.11 and 4.15 from Ardevol-Pulpillo et al. 2019, respectively). The average electron fraction of the outflow increases by 5%, and the outflow quantity decreases by about 50% in the new scheme, as the diffusion time correspondingly decreases by an order of magnitude. This difference in outflow properties comes from the high velocity neutrino-driven, early time outflows, which retain less energy deposited by neutrinos, since cooling is more efficient.

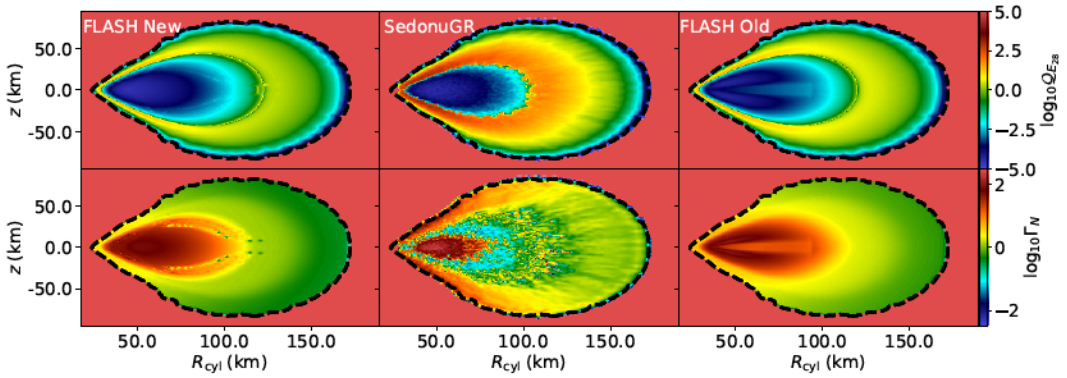

Figure 4.2: Comparison of neutrino source terms (*Top*: energy rate per unit mass in cgs, *Bottom*: number rate per baryon) obtained using a leakage scheme with the diffusion time prescription from Ardevol-Pulpillo et al. (2019) and light bulb absorption (*Left*: `FLASH` New), *Center*: `SedonuGR` Monte-Carlo transport, and the leakage scheme plus light bulb absorption previously implemented in Metzger and Fernández (2014) (*Right*: `FLASH` Old). The background fluid quantities correspond to a snapshot of the FLASH New simulation at 0.6 ms The new leakage scheme no longer artificially suppresses the source terms in the midplane of the torus, coming closer to the results of `SedonuGR`. Contours of $10^5 \mathrm{g\,cm^{-3}}$ in density are shown as thick dashed lines, corresponding to the density cutoff at which `SedonuGR` no longer performs neutrino calculations.

The average mass-flux-weighted electron fraction of the outflow increases by 5% when using the new diffusion time formulation, as shown in the histogram of torus outflows in Figure 4.1. This result corresponds to a decrease in diffusion time by a factor of ~ 10 in the high-density regions of the torus. Neutrinos are still preferentially trapped near the midplane, but the new methodology no longer overestimates this effect for the optically thin torus. The new method yields about 50% less mass outflows, predominately due to the same effect: the energy deposited into early time outflows is cooled more efficiently, unbinding less material. The major difference occurs in the neutrino-driven outflow ejected from the back of the torus, with electron fraction $Y_e \sim 0.25$. We caution that this difference will likely not extend to the late-time, radiatively inefficient evolution, as the energy and density of late time outflows appear identical, and

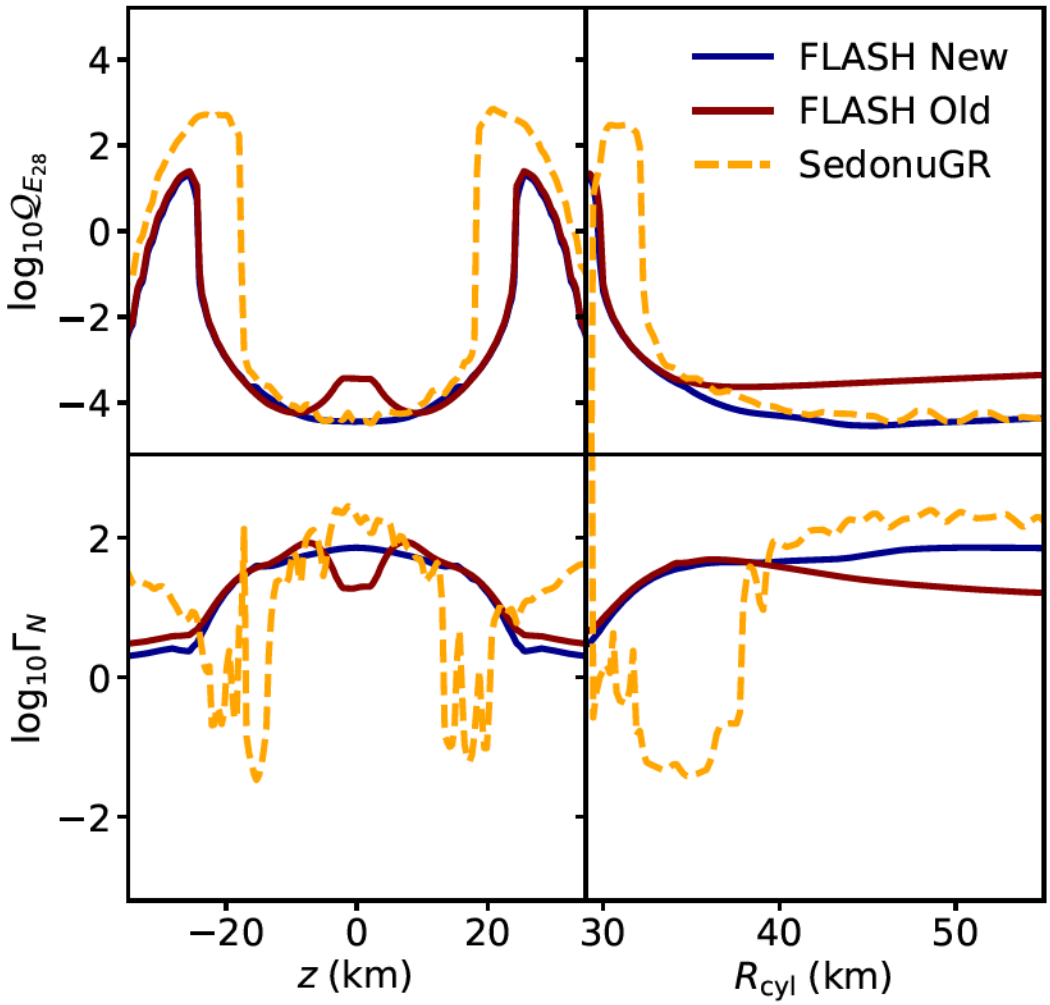

Figure 4.3: Comparison of neutrino source terms in the updated leakage scheme (`FLASH` New), `SedonuGR`, and the leakage scheme previously implemented (`FLASH` Old). Like in Figure 4.2, the top rows show rate of change of internal energy, but this time taking a slice through the density maximum in the z-direction (left), and a slice through the equatorial plane (right) of the $0.03 M_\odot$ torus at 0.6 ms. The bottom panels are identical slices but for the rate of change of lepton number. The leakage schemes follow approximately the correct curve, as previously shown (Richers et al., 2015), but once again the new scheme is closer to the MC method of `SedonuGR`, particularly when it comes to the source terms in the torus midplane.

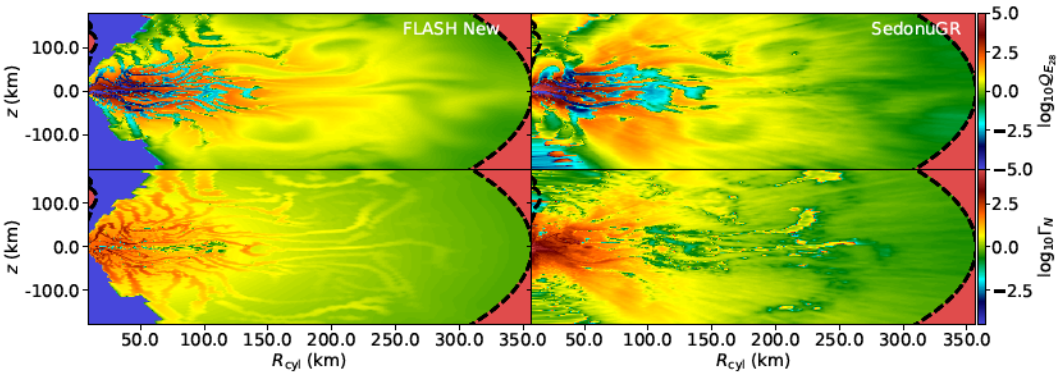

Figure 4.4: Same as Figure 4.2, but for a $0.1M_\odot$ torus evolved with 2D-MHD at ~ 30 ms using the updated leakage scheme and comparing with `SedonuGR`. There are no previous MHD results to compare with. Overall, `SedonuGR` and the new leakage scheme show similar trends in both heating/cooling and change in lepton number. `SedonuGR` does not discriminate between ambient and torus material, while our scheme does not perform neutrino calculations on ambient matter. This appears as purple areas in the poloidal regions of the `FLASH` simulations.

affects mainly the initial winds.

4.2.2 Comparison with `SedonuGR` in Hydro

We compare the emission and absorption of neutrinos to the time independent Monte-Carlo neutrino transport code `SedonuGR` (Richers et al., 2015, 2017). We are interested in the rate of change of lepton number, which governs the change in electron fraction, and the rate of change of internal energy, which governs changes in internal energy of the ejecta due to neutrinos. Following Richers et al. (2015), we load a fluid snapshot from the `FLASH4.5` simulation using the new method in `SedonuGR`. We use the Helmholtz EOS in `SedonuGR` for consistency.

At late times, the neutrino scheme for the optically thin torus shows minimal differences with the full Monte-Carlo results (Richers et al., 2015). The changes to the neutrino scheme are most evident at very early times, so we choose a time

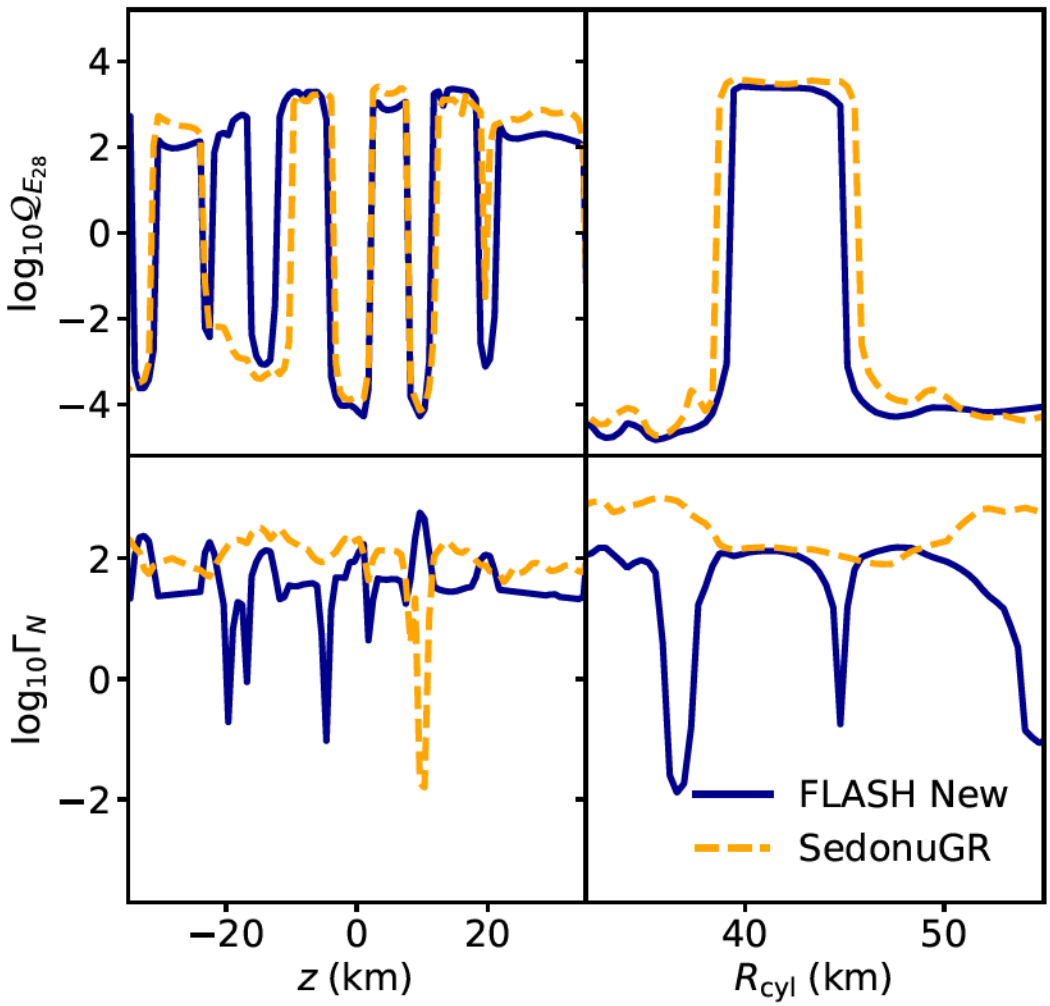

Figure 4.5: Same as Figure 4.3, but for a $0.1 M_\odot$ torus evolved with 2D-MHD and the updated leakage scheme at $\sim$ 30 ms. There are no previous MHD results to compare with, but the overall effects of neutrinos are captured well, with significant deviations only in small localized regions.

of $\sim$0.6 ms for the comparison, the result of which is shown in Figure 4.2. Most of the differences in source terms occur in the regions where absorption becomes important, which in our approach is handled by an approximate light bulb implementation (Fernández and Metzger, 2013; Metzger and Fernández, 2014), which we did not modify here. Importantly, the new neutrino leakage scheme no longer suppresses neutrino emission in the midplane of the torus, where the pressure scale height is comparatively large. This is shown quantitatively with slices in the equatorial plane and along the z-direction at the torus density maximum in Figure 4.3.

4.2.3 MHD Comparison with `SedonuGR`

Since our base torus is more massive than those used in the previous hydrodynamic test runs, and MHD evolution differs in comparison to viscous hydrodynamics, we also show a comparison of our leakage scheme in 2D-MHD with results from `SedonuGR` (Figure 4.4). Equatorial and vertical slices through the density maximum of a torus identical to our base model are shown in Figure 4.5 at 30 ms, when the neutrinos are important for setting the electron fraction of the outflows. Importantly, the source term modifying the electron fraction remains of the same order of magnitude across most of the torus.

Chapter 5

Long-term 3D MHD Simulations of Black Hole Accretion Disks formed in Neutron Star Mergers

As noted in Chapter 1, disk winds from BH accretion disks can be the most massive component in kilonova models. While many studies have utilized a viscous parameterization of MRI driven outflows, it has been shown that these do not capture all the outflows from BH-accretion disks, in particular fast magnetized winds that are launched in the first $\sim 100\,\mathrm{ms}$. At the time of writing this chapter, there were not many long term ($\sim 1\,\mathrm{s}$) 3D MHD simulations of BH-accretion tori, and they implemented varying microphysics. This included differing neutrino schemes for leakage and/or absorption, utilizing either full GR or pseudo-Newtonian potentials, and running for times ranging from $\lesssim 0.1 - 10\,\mathrm{s}$ with different initial conditions. These had not yet converged on the typical masses, velocities, and composition of ejecta from the system. (Hossein Nouri et al., 2018; Siegel and Metzger, 2018; Fernández et al., 2019b; Christie

et al., 2019; Miller et al., 2019; Hayashi et al., 2022; Just et al., 2022).

In this chapter, we use the MHD and neutrino implementations described in the previous chapters to explore the role of magnetic field geometry, disk compactness, nuclear recombination, and neutrino absorption on mass ejection in MHD simulations that have identical microphysics. We perform simulations for initial conditions relevant to GW170817, as well as to systems that could feasibly result from a NS-BH merger. The main limitation of our approach is the absence of relativistic jets, thus our focus is on the sub-relativistic outflows that are launched far enough away from the BH that relativistic effects are less important. These contain most of the ejected mass, and are therefore most relevant to the kilonova emission and r-process nucleosynthesis.

The structure of this chapter is the following. Section §5.1 presents a description of the numerical methods employed and models evolved. In §5.2 the results of our simulations are presented, analyzed, and compared to previous work. We conclude and summarize in §5.3. The previous chapters describe the implementation and testing of the MHD (§2, §3) and neutrino leakage (§4) modules employed.

5.1 Methods

5.1.1 Numerical MHD

Our simulations employ a customized version of `FLASH4.5` (Fryxell et al., 2000; Dubey et al., 2009), in which we have modified the unsplit MHD solver of Lee (2013) to work in 3D curvilinear coordinates with non-uniform spacing (see Chapter 2 for details). We use this code to numerically solve the Newtonian equations of mass, momentum, energy, and lepton number conservation

in MHD supplemented by the induction equation. Additional source terms include the pseudo-Newtonian gravitational potential of a BH and the emission and absorption of neutrinos:

$$\frac{\partial \rho}{\partial t} + \nabla \cdot [\rho \mathbf{v}] = 0 \tag{5.1}$$

$$\frac{\partial (\rho \mathbf{v})}{\partial t} + \nabla \cdot [\rho (\mathbf{v} \otimes \mathbf{v}) - (\mathbf{B} \otimes \mathbf{B})] + \nabla P = -\rho \nabla \Phi_{\mathrm{A}} \tag{5.2}$$

$$\frac{\partial (\rho E)}{\partial t} + \nabla \cdot [\mathbf{v}(\rho E + P) - \mathbf{B}(\mathbf{v} \cdot \mathbf{B})] = -\rho \mathbf{v} \cdot \nabla \Phi_{\mathrm{A}} + Q_{\mathrm{net}} \tag{5.3}$$

$$\frac{\partial Y_e}{\partial t} + \mathbf{v} \cdot \nabla Y_e = \Gamma_{\mathrm{net}} \tag{5.4}$$

$$\frac{\partial \mathbf{B}}{\partial t} + \nabla \cdot (\mathbf{v} \otimes \mathbf{B} - \mathbf{B} \otimes \mathbf{v}) = 0, \tag{5.5}$$

where ρ is the density, $\mathbf{v}$ is the velocity, $\mathbf{B}$ is the magnetic field (including a normalization factor $\sqrt{4\pi}$) , Y_e is the electron fraction, E is the total specific energy of the fluid

$$E = \frac{1}{2}(\mathbf{v} \cdot \mathbf{v} + \mathbf{B} \cdot \mathbf{B}) + e_{\mathrm{int}}, \tag{5.6}$$

with e_{int} the specific internal energy, and P is the sum of gas and magnetic pressure

$$P = P_{\mathrm{gas}} + P_{\mathrm{mag}}, \tag{5.7}$$

$$P_{\mathrm{mag}} = \frac{1}{2}\mathbf{B} \cdot \mathbf{B}. \tag{5.8}$$

The induction equation (5.5) is discretized using the Constrained Transport (CT) method (Evans and Hawley, 1988) and conserved quantities are evolved using the HLLD Riemann solver (Miyoshi and Kusano, 2005) with a piecewise linear MUSCL-Hancock reconstruction method (Colella, 1985). The gravity of the BH is modeled with the pseudo-Newtonian potential Φ_{A} of Artemova et al. (1996), ignoring the self-gravity of the disk (see also Fernández et al. 2015). The

equation of state (EOS) is that of Timmes and Swesty (2000), with abundances of protons, neutrons and α-particles in nuclear statistical equilibrium (NSE) so that $P_{\rm gas} = P_{\rm gas}(\rho, e_{\rm int}, Y_e)$, and accounting for the nuclear binding energy of α-particles as in Fernández and Metzger (2013).

We implement the framework for neutrino leakage emission and annular light bulb absorption described in Fernández and Metzger (2013) and Metzger and Fernández (2014). The scheme includes emission and absorption of electron neutrinos and antineutrinos due to charged-current weak interactions on nucleons, and with improvements in the calculation of the neutrino diffusion timescale in high-density regions following the prescription of Ardevol-Pulpillo et al. (2019). A detailed description of the implementation and verification tests (comparing to the Monte Carlo scheme of Richers et al. 2015) are presented in Chapter 4.

The leakage and absorption scheme outputs scalar source terms for the net rate of change of energy per unit volume $Q_{\rm net}$, and net rate of change per baryon of lepton number $\Gamma_{\rm net}$, which are respectively applied to E and Y_e (equations 5.3 and 5.4) in operator-split way. We neglect the contribution of neutrinos to the momentum equation.

Finite-volume codes fail when densities in the simulation become too low. We impose a radial- and time-dependent density floor, designed to prevent unreasonably low simulation timesteps in highly magnetized regions (e.g., near the inner radial boundary and extending out a few km along the the rotation axis) while also not affecting the dynamics of outflow. It has a functional form approximately following that in Fernández et al. (2019b)

$$\rho_{\rm floor} = \rho_{\rm sml} \left(\frac{r}{20{\rm km}} \right)^{-3} \left(\frac{\max[t, 0.1s]}{0.1{\rm s}} \right)^{-1.5}, \tag{5.9}$$

where $\rho_{\rm sml} = 2\times10^4$ g cm^{-3} and r is the spherical radius. The time dependence is modelled after empirically determining the rate of change of the maximum torus density in 2D runs of the baseline model. When the density undershoots the floor value, it is topped up to the floor level with material tagged as ambient, such that we can keep track of it and discard it when assessing outflows and accretion. Keeping the density above the floor is generally enough to prevent the internal energy (and gas pressure) at levels that do not crash the code. Nevertheless, we also impose explicit floors for these quantities, following the same form as in equation (5.9), but with normalizations $P_{\rm sml} = 2\times10^{14}\,{\rm erg\,cm^{-3}}$ and $e_{\rm sml} = 2\times10^{11}\,{\rm erg\,g^{-1}}$ for gas pressure and internal energy, respectively.

5.1.2 Computational Domain and Initial Conditions

Equations (5.1)-(5.5) are solved in spherical polar coordinates (r, θ, ϕ) centered at the BH and with the z-axis aligned with the disk and BH angular momentum. The computational domain extends from an inner radius, $r_{\rm in}$, located halfway between the innermost stable circular orbit (ISCO) and the BH horizon, both dependent on the BH mass and spin, to an outermost radius $r_{\rm out}$ located at $10^4 r_{\rm in}$. The polar and azimuthal angular ranges are $[5^\circ, 175^\circ]$ and $[0, 180^\circ]$, respectively, corresponding to a half-sphere with a 5° cutout around the z-axis. The radial grid is discretized with 512 logarithmically-spaced cells satisfying $\Delta r/r \sim 0.018$, the meridional grid has 128 cells equally spaced in $\cos\theta$, corresponding to $\Delta\theta \sim 0.92^\circ$ at the equator, and the azimuthal grid is uniformly discretized with 64 cells.

The boundary conditions are set to outflow at the polar cutout and at both radial limits, and to periodic at the ϕ boundaries. The cutout around the polar axis is used to mitigate the stringent time step constraints arising from the

small size of ϕ cells next to the z axis. We do not expect our polar boundary conditions to affect our analysis, as the sub-relativistic outflow is well separated from the jet by a centrifugal barrier (Hawley and Krolik, 2006). Any outflow along the polar axes without the use of full GR is unreliable anyway, as many of the proposed mechanisms for jet formation involve general relativistic energy extraction from the BH spin energy (e.g., the Lense-Thirring and Blandford-Znajek effects: Bardeen and Petterson 1975; Blandford and Znajek 1977). These processes also involve the formation of a baryon-free funnel along the rotation axis, which means outflow along the polar axes contains minimal mass. Evolution tests using reflecting, transmitting (with no azimuthal symmetry), and outflow polar boundary conditions showed little to no difference over short times after initialization ($\sim$0.5 orbits).

The initial condition for all of our models is an equilibrium torus with constant specific angular momentum, entropy, and composition, consistent with the pseudo-Newtonian potential for the BH (Fernández and Metzger, 2013; Fernández et al., 2015). The input parameters are the BH mass, torus mass, radius of density peak, entropy (i.e. thermal content or vertical extent), and Y_e. In all cases, the latter two parameters are set to $s_B = 8\ k_B$/baryon and $Y_e = 0.1$, respectively, with other parameters changing between models (§5.1.3). Initial maximum tori densities $\rho_{\rm max}$ are typically $\sim 10^{10} - 10^{11}\,{\rm g\,cm^{-3}}$.

Recent studies have shown that tori formed in NS mergers have a doubly peaked distribution of s_B and Y_e (Nedora et al., 2021; Most et al., 2021), however, the use of more realistic initial conditions for these quantities has little impact on the resulting outflows (e.g., Fujibayashi et al. 2020c), and is expected to be smaller than differences due to our approximate handling of neutrino interactions and gravity.

Models that start with a poloidal field are initialized from an azimuthal magnetic vector potential which traces the density contours, such that $A_\phi \propto \max(\rho - \rho_0, 0)$, where ρ_0 is defined as $0.009\rho_{\rm max}$, ensuring the field is embedded well within the torus (e.g., Hawley 2000). This yields an initially poloidal field topology, commonly known as "standard and normal evolution" (SANE) in the literature. The normalization is chosen such that the maximum magnetic field strength ($\sim 4 \times 10^{14}\,{\rm G}$) is dynamically unimportant, with an average gas to magnetic pressure ratio of

$$\langle\beta\rangle = \frac{\int P_{\rm gas}{\rm d}V}{\int P_{\rm mag}{\rm d}V} = 100 \tag{5.10}$$

with $\min(\beta) \sim 5$ at the inner edges and $\max(\beta) \sim 10^5$ at the initial density maximum. We also evolve a model that starts with a toroidal field, which is initialized by imposing a constant $B_\phi = 4 \times 10^{14}\,{\rm G}$ wherever $\rho > \rho_0$. The magnetic field strength and mass density set the Alfvén velocities in the meridional and azimuthal directions,

$$v^a_{\theta,\phi} = \frac{B_{\theta,\phi}}{\sqrt{\rho}}, \tag{5.11}$$

which in turn determine the respective wavelengths of the most unstable MRI modes (e.g., Balbus and Hawley 1992; Duez et al. 2006),

$$\lambda^{\rm MRI}_{\theta,\phi} \sim \frac{2\pi|v^a_{\theta,\phi}|}{\Omega_z}, \tag{5.12}$$

where Ω_z is the cylindrical angular velocity. All of our simulations resolve the relevant MRI modes with least 10 cells within the torus. Resolution tests with 2D models indicate that our mass ejection results have an uncertainty of $\sim 10\%$ due to spatial resolution (§5.2.3).

Model	$M_{\rm bh}$ ($M_\odot$)	$M_{\rm t}$ ($M_\odot$)	$R_{\rm t}$ (km)	**B** geom	α-rec	ν-abs	dim
base	2.65	0.10	50	pol	yes	yes	3
bhns	8.00	0.03	60				
base-tor	2.65	0.10	50	tor			
base-2D	2.65	0.10	50	pol	yes	yes	2.5
base-norec				pol	no		
base-noirr					yes	no	

Table 5.1: List of simulation parameters. Columns from left to right show model name, BH mass, initial torus mass, initial radius of maximum torus density, initial magnetic field geometry (pol: poloidal, tor: toroidal), inclusion of the nuclear recombination energy of α particles in the EOS, use of neutrino absorption to evolve E and Y_e, and simulation dimensionality. All BHs are assumed to have a dimensionless spin parameter 0.8.

5.1.3 Models

Table 5.1 shows all the models we evolve and the parameters used. Our *base* model employs the most likely BH mass ($M_{\rm bh} = 2.65 M_\odot$, dimensionless spin 0.8), initial torus mass ($M_{\rm t} = 0.1 M_\odot$), and initial radius of density peak ($R_{\rm t} = 50\,{\rm km}$) for GW170817 (e.g., Abbott et al. 2017; Shibata et al. 2017; Fahlman and Fernández 2018), using a poloidal field geometry. Model *bhns* uses a typical parameter combination expected from a BH-NS merger ($M_{\rm bh} = 8 M_\odot$ with spin 0.8; $M_{\rm t} = 0.03 M_\odot$; $R_{\rm t} = 60\,{\rm km}$), also with a poloidal initial field, to probe the effect of a higher disk compactness (e.g., Fernández et al. 2020).

Three additional simulations test the influence of key physical effects on the *base* model. Model *base-tor* employs an initial toroidal magnetic field geometry instead of poloidal. The other two are explored in axisymmetry (2.5 dimensions): Model *base-norec* sets the nuclear binding energy of α-particles to zero, and model *base-noirr* turns off neutrino absorption. These two simulations are compared to model *base-2D*, an axisymmetric version of the *base* model. All 3D models are evolved for at least 3 s, or until a time at which there is a clear

power-law decay with time in the ejected mass at large radius, allowing for an analytic extrapolation until completion of mass ejection (§5.1.4). To achieve this phase, the *base* model needs to be evolved to 4 s. The axisymmetric models are evolved until 1.4 s, when accretion onto the BH stops due to a build up of magnetic pressure: continuing evolution causes feedback which disrupts the torus. The MRI is expected to dissipate in axisymmetry after ~ 100 orbits at the initial torus density peak, corresponding to a few 100 ms (e.g., Cowling 1933; Shibata et al. 2007).

5.1.4 Outflow Characterization

The mass flux at a given radius is computed as

$$\dot{M}(r) = \iint_{A_r} (\rho v_r \mathrm{d}A_r), \tag{5.13}$$

where the spherical area A_r is given by

$$A_r = \iint r^2 \sin\theta \mathrm{d}\theta \mathrm{d}\phi. \tag{5.14}$$

For outflows, the extraction radius is $r = 10^4$ km, whereas for accretion onto the BH we take the radius of the ISCO. We only consider unbound outflows, which we quantify with a positive Bernoulli parameter at the extraction radius

$$\Phi_g + e_{\rm int} + e_{\rm k} + e_{\rm mag} + \frac{P_{\rm gas}}{\rho} > 0. \tag{5.15}$$

We also require that both outflowing and accreting matter have an atmospheric mass fraction $\chi_{\rm atms} < 0.2$, and subtract off any remaining atmospheric mass so

that

$$\rho = \rho_{\rm tot}(1 - \chi_{\rm atms}). \tag{5.16}$$

The total ejected mass is computed by temporally integrating the outflow mass flux, such that

$$M_{\rm out} = \int_t \iint_{A_r} (\rho v_r \mathrm{d}A_r)\mathrm{d}t. \tag{5.17}$$

Model	$M_{\rm out}$ $(10^{-2}M_\odot)$	$(M_{\rm t})$	$\langle Y_e\rangle$	$\langle v_r\rangle$ (c)	$t_{\rm max}$ (s)	$M_{\rm out}^{\rm blue}$ $(10^{-2}M_\odot)$	$\langle Y_e^{\rm blue}\rangle$	$\langle v_r^{\rm blue}\rangle$ (c)	$M_{\rm out}^{\rm red}$ $(10^{-2}M_\odot)$	$\langle Y_e^{\rm red}\rangle$	$\langle v_r^{\rm red}\rangle$ (c)	$M_{\rm out}^{\rm extr}$ $(10^{-2}M_\odot)$
base	2.750	0.275	0.195	0.105	4.1	0.660	0.302	0.087	2.090	0.161	0.110	3.55-4.44
bhns	0.155	0.052	0.197	0.065	4.0	0.014	0.260	0.057	0.140	0.190	0.064	0.18-0.23
base-tor	4.237	0.424	0.173	0.079	3.0	0.655	0.291	0.100	3.583	0.152	0.075	4.76-7.01
base-2D	6.225	0.623	0.329	0.182	1.4	5.528	0.349	0.169	0.697	0.176	0.279	-
base-norec	6.146	0.615	0.311	0.158	1.4	5.275	0.330	0.151	0.870	0.195	0.199	-
base-noirr	3.323	0.332	0.205	0.229	1.4	0.996	0.298	0.321	2.327	0.165	0.190	-

Table 5.2: Mass ejection results for all our simulations. Columns from left to right show model name, total unbound mass ejected during the first 3 s of the simulations for 3D models and first 1.4 s for 2D models (equation 5.17, in percent of a solar mass and relative to the initial torus mass $M_{\rm t}$), $\dot{M}_{\rm out}$-weighted average electron fraction (equation 5.18) and radial velocity (equation 5.19), maximum simulation time, as well as unbound ejected mass, average electron fraction, and radial velocity broken down by electron fraction (superscript *blue* – lanthanide-poor: $Y_e \geq 0.25$, *red* – lanthanide-rich: $Y_e < 0.25$). The last column shows the range of total unbound ejected mass extrapolated to infinity with a power-law fit to the mass outflow rate (equation 5.20). Note that 2D and 3D simulations run for different times, so direct comparisons of simulations with different dimensionality should not be made (See §5.2.3).

The mass weighted averages of electron fraction and radial velocity,

$$\langle Y_e \rangle = \frac{\int_t \iint_{A_r} (\rho v_r Y_e \mathrm{d}A_r)\mathrm{d}t,}{M_{\rm out}} \tag{5.18}$$

$$\langle v_r \rangle = \frac{\int_t \iint_{A_r} (\rho v_r v_r \mathrm{d}A_r)\mathrm{d}t,}{M_{\rm out}} \tag{5.19}$$

are provided as a summary of our model results in Table 5.2. We further subdivide outflows based on their electron fraction into "red" ($Y_e < 0.25$) and "blue" ($Y_e \geq 0.25$), based on kilonova models which predict a sharp cutoff between lanthanide-rich and lanthanide-poor matter (e.g., Kasen et al. 2015; Lippuner and Roberts 2015).

Once the torus reaches a quasi-steady phase following freezeout of weak interactions, ($t_{ss} \sim 1.1$s), the mass outflow rate enters a phase of power-law decay, $\dot{M}_{\rm out}(t > t_{\rm ss}) \propto t^{-\delta}$. We can therefore estimate the completed mass ejection over timescales of $\sim 10\,$s by extrapolating from a power-law fit to the mass outflow rate (e.g., Margalit and Metzger 2016; Fernández et al. 2019a),

$$M_{\rm out}^{\rm extr} = M_{\rm out}(t_{\rm ss}) + \frac{1}{\delta - 1}\dot{M}_{\rm out}(t_{\rm ss})t_{\rm ss}, \tag{5.20}$$

where the integral in equation 7.18 is computed until $t = t_{\rm ss}$. The choice of $t_{\rm ss}$ is made based on visual inspection of when the cumulative mass outflows begin to plateau. Varying this choice in response to episodic mass ejection events results in an uncertainty in the exponent of $|\Delta\delta| \lesssim 0.5$ corresponding to about 5-15% difference in total $M_{\rm out}^{\rm extr}$.

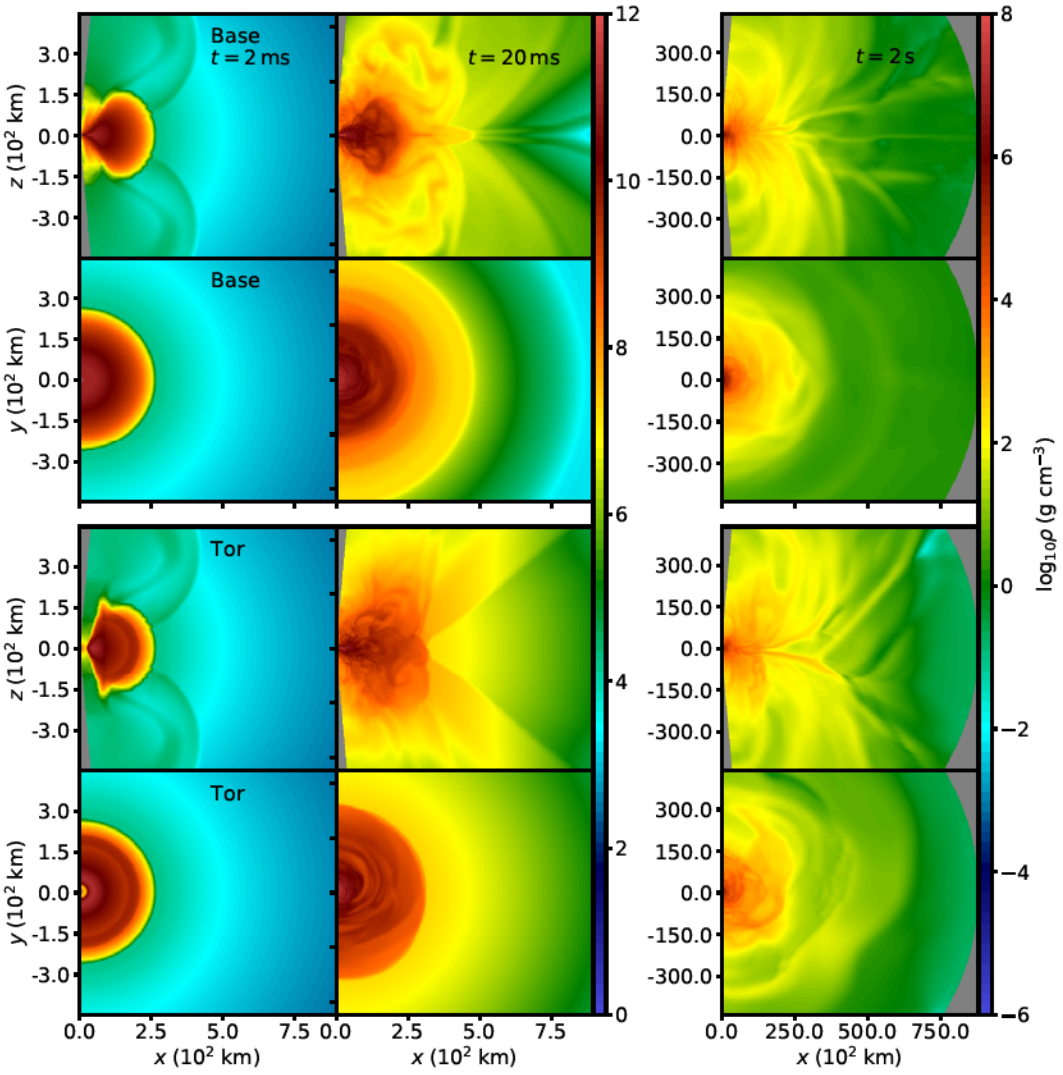

Figure 5.1: Density slices in the $x - z$ ($\phi = 0$) and $x - y$ ($\theta = 0$) plane of the *base* (top two rows) and *base-tor* (bottom two rows) models at t=2 ms (0.6 orbits at the initial torus density peak), 20 ms (6 orbits), and 2 s (600 orbits). The first two columns correspond to the early accretion and initial wind phase. Note the change in both colour table and length scale for the final column. Gray regions are outside the computational domain.

5.2 Results

5.2.1 Overview of Torus Evolution in MHD

Our *base* and *bhns* runs, with a poloidal field embedded in the torus, show very similar evolution to previous runs in (GR)MHD. Within a few orbits, accretion onto the central object begins as magnetic pressure in the torus builds up via winding and onset of the MRI, disrupting hydrostatic equilibrium. In the *base-tor* run, accretion onto the torus begins as turbulence driven within the torus by the toroidal MRI generates poloidal field. Both runs then begin mass ejection as the poloidal MRI grows (Figure 5.1).

In contrast to hydrodynamic models, mass ejection begins on a timescale of ∼ms, forming "wings" of ejected material away from the midplane and rotation axis. More isotropic, thermally-driven ejecta takes over at ∼1 s, as neutrino emission has subsided and the disk enters an advective state. As material moves outward, it cools and releases the binding energy stored in α-particles, increasing the internal energy of the fluid. Neutrino absorption, although subdominant energetically, is important in driving the evolution of Y_e. By ∼1 s, the torus has reached an equilibrium value of Y_e, and the cumulative mass outflow begins to plateau.

5.2.2 Mass Ejection in 3D Models

Table 5.2 shows the total unbound mass ejected by the end of each simulation (equation 7.18), and the extrapolation of of the mass outflow rate to infinity in time (equation 5.20), for all of our 3D models. The *base* and *base-tor* models eject $\sim 28\%$ and $\sim 42\%$ of the initial torus mass during the simulation, respectively, with the extrapolated mass ejected at late times being $\sim 40\%$ and

$\gtrsim 50\%$. The *bhns* model ejects the least mass owing to the high compactness, with $\sim 5\%$ of the initial torus mass ejected by the end of the simulation. All 3D simulations show average velocities in the range $\langle v_r \rangle \sim (0.07 - 0.11)\, c$, and average electron fractions $\langle Y_e \rangle \sim 0.17 - 0.20$.

The mass accretion and outflow rates for all 3D models are shown in Figure 5.2. Each model begins to eject mass at a steeply rising rate, primarily due to MHD effects, which eventually reaches a plateau. After rising to a peak at time $\sim 1\,\mathrm{s}$, the mass ejection rate then begins to decay as a power law with episodic ejection events. Figure 5.2 also shows that by this time, the cumulative mass ejected begins to plateau. Differences between models manifest as changes in the initial outflow time: the *base-tor* and *bhns* runs begin to eject matter $\sim 0.04\,\mathrm{s}$ and $0.02\,\mathrm{s}$ later than the *base* model, respectively. In the *base-tor* case, this delay is caused by the additional time required for the toroidal MRI to generate poloidal field, which then drives angular momentum transport. This is illustrated in Figure 5.3, which shows the evolution of the volume-integrated Maxwell stress for all 3D models. The *bhns* run has a deeper gravitational potential at the initial density maximum than the other runs (see §5.2.2), leading to more total energy input required to begin mass ejection (e.g., Fernández et al. 2020).

We also find that mass ejection peaks earlier in the *base* model than in the other two runs. The *base-tor* run reaches peak mass ejection around $0.1\,\mathrm{s}$ later than the base model at a somewhat larger outflow rate, but then decays with time following a power law slope of $\delta_{\mathrm{tor}} = 1.45$, only $\sim$3% different than the *base* model slope $\delta_{\mathrm{base}} = 1.50$. This qualitatively similar behaviour between poloidal and toroidal models is also found by Christie et al. (2019), although the initial conditions of their simulations lead to different quantitative values

of δ. Each 3D model has a different quantitative value of δ, despite having the same late-time mass ejection mechanism. This variation can be attributed to physical differences in the disks and the timing of mass ejection. Each disk reaches maximum outflow at a phase in its evolution when the remaining disk mass, wind loss rate, and accretion rate are different relative to the initial disk mass and timescale of angular momentum transport in the disk. The initial time of mass ejection is also related to the range of electron fractions in the outflow. All runs produce a broad range of Y_e in the ejecta, with a lower limit $Y_e \gtrsim 0.05$ (See §5.2.3).

Morphology

Kilonova emission is dependent on the ejecta morphology (e.g., Kasen et al. 2017; Kawaguchi et al. 2020, 2021; Korobkin et al. 2021; Heinzel et al. 2021), which can vary depending on the type of binary and mass ejection mechanism. The morphology of the disk outflow ejecta for the *base* and *base-tor* models is shown in the rightmost panel of Figure 5.1, showing a characteristic "hourglass" shape found in previous GRMHD simulations (e.g., Fernández et al. 2019b; Christie et al. 2019). This feature is robust across all our 3D models, as can be seen from the angular mass outflow histograms in Figure 5.4. Model *base-tor* ejects 50% less mass with $v \gtrsim 0.25\,c$ and within $\sim \pi/4$ of the rotation axis than model *base*, and no ejecta in this velocity range is produced within $\sim \pi/4$ of the equatorial plane. In contrast, models `base` and `bhns` have a much wider distribution of fast/early ejecta, extending down to within $\pi/6$ of the rotation axis. This implies that the morphology of the highest velocity ejecta is dependent on the initial condition of the torus, with the compactness of the disk having little effect on outflow geometry. This result is supported by the

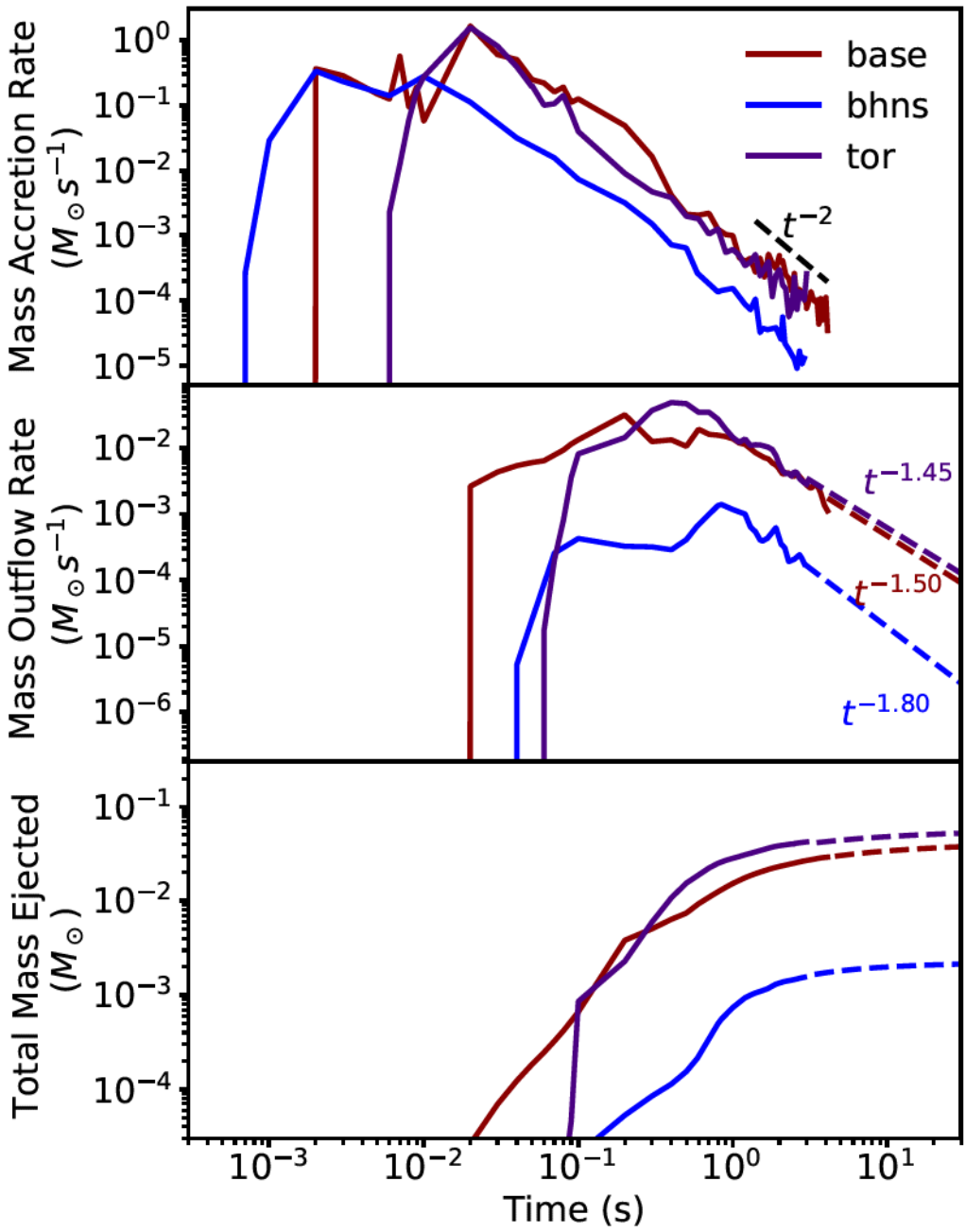

Figure 5.2: *Top:* mass accretion rate at the ISCO for all 3D models, as labeled. The dashed line shows a reference power-law dependence t^{-2}. *Middle:* unbound mass outflow rate at an extraction radius $r = 10^4$ km, for all 3D models. Outflow rates are extrapolated with a power law (dashed lines), with the fiducial power law index shown for each curve (equation 5.20). *Bottom:* evolution of the cumulative unbound mass ejected (equation 7.18). Dashed lines show the result of using the same power-law extrapolation of the outflow rate after the end of the simulation (equation 5.20).

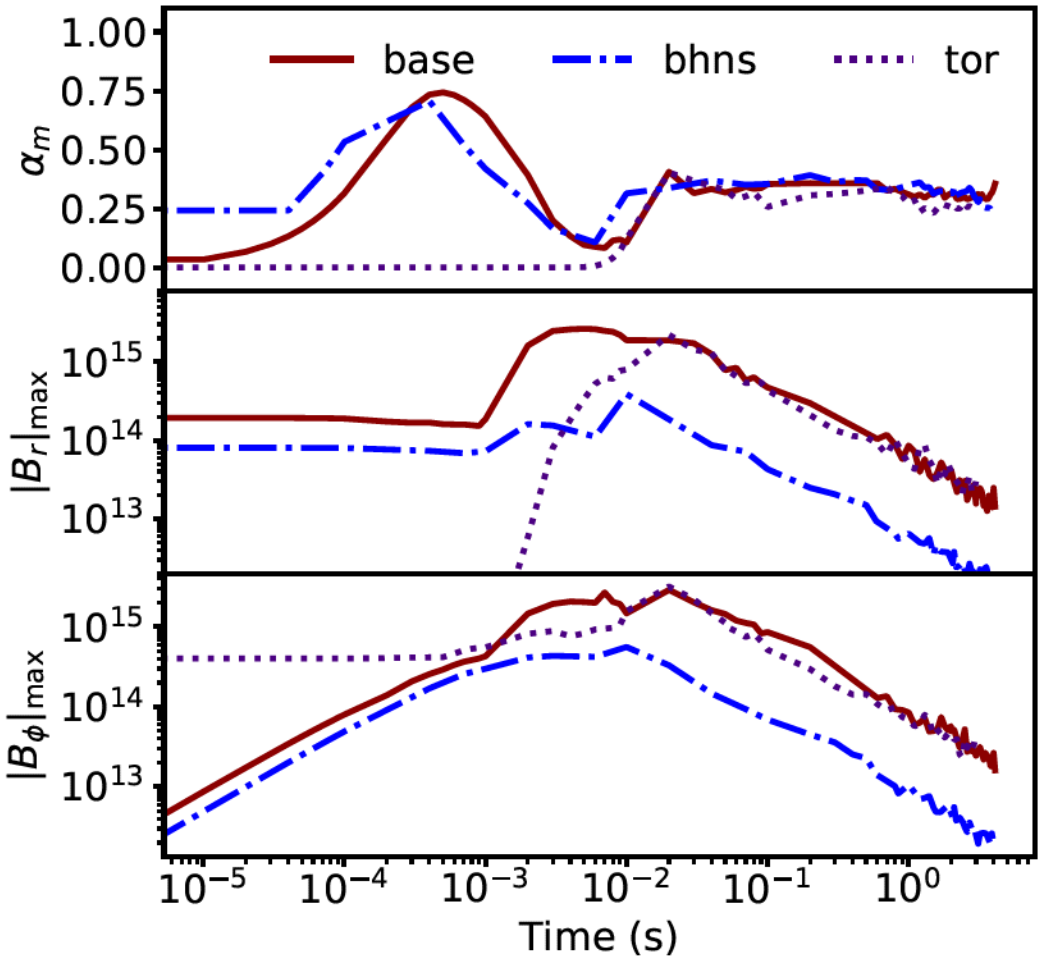

Figure 5.3: *Top*: Evolution of the volume-averaged Maxwell stress normalized by the volume-averaged magnetic pressure, $\alpha_m = \langle B_r B_\phi \rangle / \langle P_{\rm mag} \rangle$, a measure of radial angular momentum transport by magnetic forces (see Hawley 2000; Hawley and Krolik 2001 for a discussion). *Middle*: Evolution of the maximal magnitude of the radial magnetic field. *Bottom*: Evolution of the maximal magnitude of the azimuthal magnetic field.

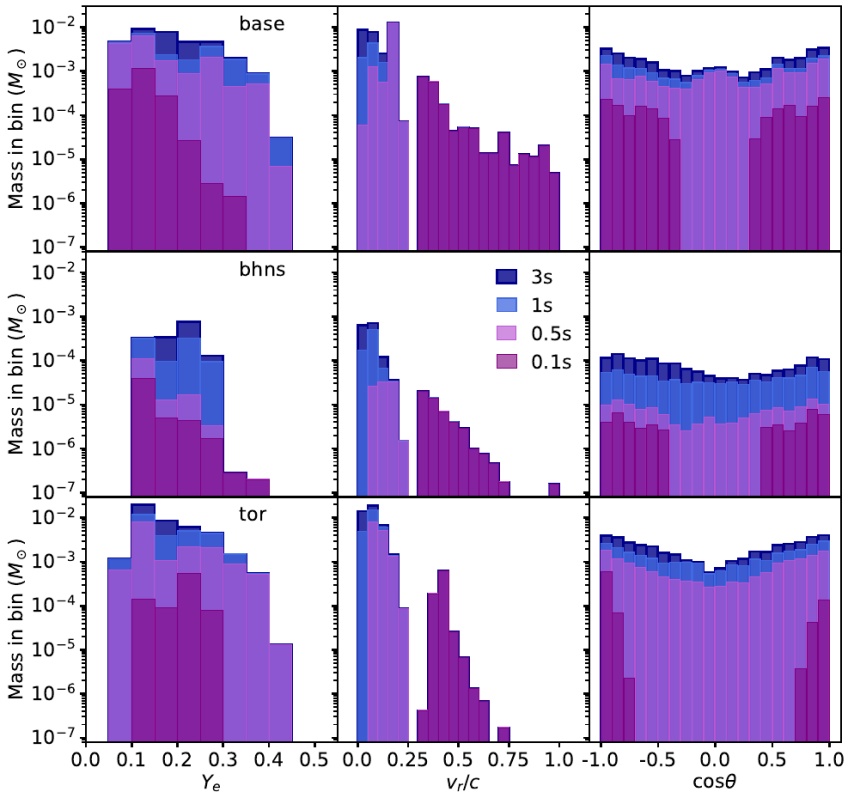

Figure 5.4: Total unbound mass ejected by our 3D models, as labeled, sorted into bins based on electron fraction Y_e,radial velocity v_r, and polar angle θ. The bin sizes are $\Delta Y_e = 0.05$, $\Delta v_r/c = 0.05$, and $\Delta \cos\theta = 0.1$, where $\cos\theta = 0$ is the midplane.

results of (Christie et al., 2019), as well as those of (Siegel and Metzger, 2018) in their discussion of the initial transient phase.

Compactness

We find that the fraction of the initial disk mass ejected decreases with increasing disk compactness (model *bhns*), following the same trend as the hydrodynamic results of Fernández et al. (2020). This shows that the additional mass ejected by MHD effects relative to pure viscous hydrodynamics also decreases with increasing disk compactness. Figure 5.4 shows that the fastest ejecta ($t < 0.1s$) becomes a smaller fraction of the total mass ejected, with the

majority of the disk outflow ensuing after 1 s. This change can be attributed to multiple differences with the *base* model: the gravitational potential is deeper by a factor ~ 2 at the density maximum, the ISCO of the BH is closer to the torus density maximum (see, e.g., Figure 5.2), and the initially lower density torus emits an order of magnitude less neutrino luminosity and is more transparent to neutrinos. Nevertheless, the different disk structure results in a shorter neutrino cooling time at the initial density peak in the *bhns* model (1 ms) relative to the *base* model (2 ms). Thus, at early times ($t < 0.1s$) when neutrino cooling is strong, disk material is more bound in the *bhns* than in the *base* case.

We note a sharp drop in mass ejected with $Y_e \sim 0.3$ for the *base* model, also found in Fernández et al. (2020), which can be attributed to the larger relative importance of neutrino absorption in more massive tori. For a neutron-rich disk where neutrino absorption dominates the evolution of Y_e, the process $\nu_e + n \rightarrow e^- + p$ occurs more frequently than its inverse, increasing the net Y_e (Siegel and Metzger, 2018; Fernández et al., 2020; Most et al., 2021).This trend is also found by Just et al. (2022) with a significantly more advanced neutrino scheme - a broader distribution in Y_e corresponds to more absorption (see their Figure 13). Similar 2D axisymmetric simulations by Shibata and Sekiguchi (2012) yield neutrino luminosities that decrease from 10^{52} erg s^{-1} to 10^{51} erg s^{-1} as the BH mass increases by from $3M_\odot$ to $6M_\odot$. We find a very similar trend as we change the compactness.

5.2.3 Mass Ejection in 2D: Sensitivity to Physics Inputs

Dimensionality

Measuring unbound ejecta by the end of each simulation, the *base-2D* model ejects a factor of ~ 2 more mass than the equivalent *base* run in 3D, despite running for 1.4 s instead of 3 s. The evolution is qualitatively similar for the first ~ 1 s, until the axisymmetric torus becomes dominated by magnetic pressure and is disrupted, at which point we end the simulation. Quantitatively, model *base-2D* produces a higher mass outflow rate at all times, in particular more ejecta with velocities $\gtrsim 0.25\,c$. We attribute this enhanced mass ejection to the lower accretion rate onto the BH in axisymmetry given the suppression of the MRI, with divergence in the evolution from the 3D case starting at ~ 20 ms. With less accretion, the larger amount of matter in the torus results in a higher outflow rate, given that the same outflow driving processes operate in 2D and in 3D.

Spatial Resolution

To quantify uncertainties due to spatial resolution, we run versions of model *base-2D* at half and twice the resolution in both the radial and polar directions. The high-resolution model is evolved until 0.5 s, probing the early, magnetically-driven phase, and the half-resolution model is evolved until 1 s, which includes the radiatively-inefficient phase of mass ejection. Mass ejection up to 1 s is $\sim 10\%$ higher in the standard resolution model relative to the low-resolution model. We thus associate an uncertainty of 10% to our mass ejection numbers due to spatial resolution. The growth of the toroidal magnetic field is identical during both the magnetic winding and MRI growth phase in all models until 3 ms, when the maximum value of toroidal magnetic field saturates at 2×10^{15} G.

We find a 0.5% difference in the saturation value of $|B_\phi|$ between the standard and high resolution runs, and a 5% lower saturation value comparing the low to standard resolution run. Thereafter, the maximum of $|B_\phi|$ undergoes stochastic fluctuations with amplitude of order unity until a dissipation phase begins at $\sim 30\,\mathrm{ms}$. The standard and high-resolution models remain consistent within fluctuations.

Nuclear Recombination

Comparing mass ejection from models *base-2d* (with recombination) and *base-norec* (without recombination), we find that nuclear recombination remains a subdominant effect until the end of our 2D simulation at 1.4 s. Before 0.5 s, energy input from nuclear recombination increases the mass-averaged velocity of ejecta, resulting in a noticeable decrease in mass ejected at $\sim 0.3\,c$ and a increase at $\sim 0.25\,c$ in model *base-norec* compared to model *base*. After $\gtrsim 0.5\,\mathrm{s}$, comparatively less mass is ejected in model *base-norec* due to the lack of recombination heating. In other words, mass which would have been ejected in the initial MHD-driven phase is instead ejected slower and at a later time, indicating that the net effect of nuclear recombination is to make matter less gravitationally bound and thus easier to eject by magnetic forces at early times. We find an almost identical distribution in electron fraction, skewed to a slightly lower average value since less mass is ejected later when the charged current weak interactions have already raised the Y_e.

Neutrino Absorption

Inclusion of neutrino absorption results in additional mass ejection by a factor of ~ 2 relative to a model without it (*base-noirr*), and a negligible effect on

the mass ejected at $t < 0.1\,\mathrm{s}$, when magnetic stresses dominate. The energy input from neutrino absorption causes additional mass to become marginally unbound, extending the distribution in velocity space to slower outflow. However, since more mass is ejected, neutrino absorption produces a *decrease* by $0.05\,c$ in the mass averaged velocity. Turning off neutrino absorption skews the electron fraction of the ejecta to lower values, with more mass (factor of 2) being ejected at all times with $Y_e < 0.1$, and 2 orders of magnitude less ejecta with $Y_e > 0.4$.

5.2.4 Comparison to previous work

The ejected masses and velocities from our 3D models are in broad agreement with comparable simulations (Siegel and Metzger, 2018; Miller et al., 2019; Fernández et al., 2019b; Christie et al., 2019; Just et al., 2022). The *base* run is qualitatively closest to the model of Siegel and Metzger (2018), which lacks neutrino absorption, and to the MHD model of Just et al. (2022), which has a less massive torus ($0.01 M_\odot$). Siegel and Metzger (2018) find that 16% of the torus is ejected during 381 ms of evolution, and Just et al. (2022) that 20% of the initial torus mass is ejected during 2.1 s. Our *base* model ejects a higher fraction of the initial disk mass due to the difference in compactness as well as a longer simulation time. Relative to the long-term GRMHD simulation of Fernández et al. (2019b), which employed an initial field geometry conducive to a magnetically-arrested disk (MAD, e.g., Tchekhovskoy et al. 2011), ran for a longer time ($\sim 10\,\mathrm{s}$), and did not include neutrino absorption, our base run ejects $\sim 20\%$ less mass by the end of the simulation at 3s. Our extrapolated ejected masses are comparable to that from this longer run, with other differences explainable by the difference in compactness and initial field geometry.

The weak poloidal (SANE) model from Christie et al. (2019) is run for the same amount of time as our base run but with an initially weaker field, and also ejects $\sim 30\%$ of the torus mass during the simulation, despite not including neutrino absorption.

The toroidal run of Christie et al. (2019) ejects 3% less mass than their weak poloidal (MAD) run, whereas we find 15% more mass ejection in our *base-tor* (toroidal) model relative to our *base* (poloidal) model. We do find a lower average velocity (by $\sim 0.02\,c$) in the *base-tor* model relative to our *base* model, same as they do. Christie et al. (2019) find that their toroidal model begins mass ejection at almost the same time as their weak poloidal run, and find a more sustained period of mass ejection from $\sim 0.01 - 0.05\,\mathrm{s}$ in the toroidal model. Comparatively, we find that mass ejection in our *base-tor* model begins later and quickly rises to peak at a value higher than that of the poloidal simulation. This difference in dynamics could be attributed to a comparatively stronger toroidal magnetic field ($\beta \sim 0.01 - 2$ in the initial torus) and the effect of neutrino absorption. We do not vary the initial field strength in our simulations, as a lower field strength would require more cells to properly resolve the MRI. We can speculate on how lowering the field strength would change our outflows by comparing to the results of Christie et al. (2019). They find that lowering the field strength reduces the initial ($t \lesssim 0.5\,\mathrm{s}$) outflows driven by magnetic stresses, but the late-time thermal outflows are nearly identical. The effects on our (SANE) field configuration would likely be similar, but less prominent, given that their MAD configuration is optimized for producing magnetic outflows.

The work of Miller et al. (2019) utilizes the same initial conditions as our *base* model but with a more advanced neutrino scheme to treat neutrino emis-

sion and absorption. We find a similar amount of mass ejected by 100 ms of evolution ($\sim 2 \times 10^{-3} M_\odot$), indicating broad agreement despite the difference in neutrino schemes.

Utilizing a mean field dynamo to address the suppression of MRI in 2D, Shibata et al. (2021b) run resistive MHD simulations of high compactness toroidal disks. They find $\sim 10 - 20\%$ of the initial disk mass is ejected over $\gtrsim 4\,\mathrm{s}$ with an average electron fraction $\langle Y_e \rangle \sim 0.25 - 0.35$, in broad agreement with our findings. Notably, they find that mass ejection begins $\gtrsim 500$ ms later than in our toroidal run, although this delay can be attributed to the high compactness of their models.

The recent GRMHD simulations of Hayashi et al. (2022) start from the inspiral of a $1.35 M_\odot$ NS and a 5.4 or 8.1 $M_\odot$ BH and evolve the remnant for up to 2 s, including neutrino leakage and absorption. They find qualitatively similar results when compared to our runs, albeit with much larger tori masses post-merger ($\sim 0.2 - 0.3 M_\odot$). The fraction of the torus mass ejected is also comparable to our *bhns* runs, as $\sim 10\%$ of their tori is ejected in the first 1 s, with a broad distribution in both electron fraction and velocity. Discounting dynamical ejecta, they find a peak electron fraction $Y_e \sim 0.25 - 0.35$ and post merger outflow velocities of $v \lesssim 0.08\,c$, in good agreement with our results. They find outflows starting at $\gtrsim 200\,\mathrm{ms}$ later than our *bhns* model, however the initial tori in their simulations are in a deeper potential well, and form with an initially toroidal field, both of which we find delay outflows in comparison to our *base* model.

By analyzing the net specific energy of tracer particles, Siegel and Metzger (2018) find that nuclear recombination of α-particles plays a key role in unbinding matter in the disk outflow (in a simulation that does not include

neutrino absorption). Our 2D model *base-norec* which has nuclear recombination turned off but includes neutrino absorption, ejects only slightly less mass than our *base-2D* run indicating that under these circumstances nuclear recombination is a sub-dominant effect. It remains to be tested whether recombination will remain sub-dominant in a fully 3D simulation that includes neutrino absorption and runs for a long time ($\gg 1\,\mathrm{s}$).

Our 2D model without neutrino absorption (*base-noirr*) ejects a factor ~ 2 less mass than the *base-2D* model. This difference is significantly larger than that found in models that employ viscous hydrodynamics, which typically find that neutrino absorption is dynamically sub-dominant for mass ejection (e.g., Fernández and Metzger 2013; Just et al. 2015). This also inconsistent with the 3D MHD run of Just et al. (2022), who find that turning off neutrino absorption results in a 2.5% *increase* in mass ejection relative to the initial torus mass, although they use a different neutrino leakage scheme and a less massive torus that is more transparent to neutrinos. Our results are limited by the use of axisymmetry for these simulations, but suggest that neutrino absorption could indeed be more significant for the dynamics of mass ejection and motivates further studies in 3D.

5.3 Summary and Discussion

We have run long-term 3D MHD simulations to explore mass ejection from BH-tori systems formed in neutron star mergers. The publicly available code `FLASH4.5` has been extended to allow its unsplit MHD solver to work on non-uniform spherical coordinates in 3D (Chapter 2, 3). All of our models include a physical EOS, neutrino emission and absorption via a leakage scheme with disk-lightbulb irradiation (Chapter 4), and treat the gravity of the BH with a

pseudo-Newtonian potential. Our 3D models employ different initial magnetic field geometries and disk compactnesses. We have also carried out axisymmetric models that suppress the nuclear recombination and neutrino absorption source terms.

The disk outflows from our 3D models exhibit a broad distribution in electron fraction and ejection polar angle (Figure 5.4), with a typical hourglass morphology (Figure 5.1). The tori eject matter with a bimodal distribution in velocity (Figure 5.4) associated with two different mass ejection phases: MHD stresses power early time ($t < 0.1\,\mathrm{s}$) high velocity ($v \gtrsim 0.25\,c$) ejecta, and late-time ($t \sim \mathrm{s}$) "thermal" ejection provides the majority of mass outflows centered around $v \sim 0.1\,c$.

We find that imposing an initially toroidal field configuration ejects ∼15% more of the initial torus mass than the standard SANE poloidal field of similar maximal field strength (Figure 5.2, Table 5.2). However, the toroidal model ejects an order of magnitude less ejecta in the first 100 ms of evolution (Figure 5.4), comprising all of the ejecta travelling at velocities $v \gtrsim 0.25\,c$. The high-velocity ejecta is suppressed by the additional time it takes for dynamo action to convert toroidal into large-scale poloidal fields, which then drives radial angular momentum transport.

Increasing the disk compactness to values expected for typical BH-NS mergers results in significantly less mass ejection relative to our *base* (NS-NS) model, beginning at a later time and decaying at a faster rate. Comparing to the viscous hydrodynamic models of Fernández et al. (2020), we find the same overall trend of decreased mass ejection with increasing disk compactness. Model *bhns* has the same initial torus and BH configuration as their model *b08d03*: by 4 s, our 3D MHD simulation has ejected 5.5% of the initial torus mass, while the

viscous hydrodynamic equivalent has ejected only 1.9% of the initial disk mass by the same time. The hydrodynamic model goes on to eject 5.0% of the initial disk mass after 12 s of evolution, with mass ejection peaking at 2.3 s but remaining non-negligible until later times. The extrapolated outflow for our 3D MHD model *bhns* predicts $6 - 8\%$ of the initial torus mass, which is consistent with the previously-found enhancement in mass ejection by MHD relative to viscous hydrodynamics at smaller compactnesses when evolving both to ~ 10 s (Fernández et al., 2019b). Our results inform analytic fits to fractions of the initial disk mass ejected like that of Raaijmakers et al. (2021), which has the enhancement in mass ejection due to magnetic effects relative to viscous hydrodynamics as a free parameter. More 3D MHD simulations at different compactness and with various initial magnetic field geometries are needed to improve the predictive power of these fits.

Our axisymmetric models that vary the physics show that nuclear recombination is a sub-dominant effect, while neutrino absorption can make a significant difference in mass ejection. Inclusion of neutrino absorption produces a shift of the velocity distribution at late times, down by $\sim 0.05\,c$, with negligible effects at early times ($t < 0.1$). In the absence of neutrino absorption, the distribution of electron fraction shifts to include additional material with $Y_e < 0.1$ and exclude $Y_e > 0.4$. Nuclear recombination deposits additional energy into the already unbound outflows at $t \sim 0.1$ s, resulting in ejecta with moderately higher velocities, but its absence only decreases the total ejecta mass by 1%. Inclusion of r-process heating by the formation of heavier nuclei can further speed up the ejecta at late times (Klion et al., 2022). Proper characterization of the effect of neutrino absorption and nuclear recombination on the mass ejection dynamics and composition must be done with full 3D simulations, which

unfortunately still remain expensive computationally.

Our *base* and *base-tor* models have initial conditions consistent with the post-merger system of the observed NS-NS merger GW170817. We find that although these 3D models can eject lanthanide-free material ($Y_e > 0.25$) with velocities inferred from kilonova modelling, $v \gtrsim 0.25\,c$, there is insufficient mass in the outflows to match observations (e.g., Kasen et al. 2017; Villar et al. 2017a) with the disk outflow alone. The inclusion of a finite-lived remnant in our *base* model is a promising way to produce more lanthanide-free ejecta at the required velocities (e.g., Fahlman and Fernández 2018).

The main limitations of our work are the approximations made for modelling neutrino radiation transport on the necessary timescales. Prior research into the effectiveness of neutrino schemes have shown that the differences between two-moment (M1) and Monte Carlo (MC) schemes can result in a $\sim 20\%$ uncertainty in neutrino luminosity, translating to a difference of 10% in outflow electron fraction (Foucart et al., 2020). Comparison between M1 and the leakage scheme of Ardevol-Pulpillo et al. (2019) (which our scheme is based on, see Chapter 4) shows a further 10% uncertainty in neutrino luminosities, and a comparison of leakage+M0 to M1 schemes shows that leakage schemes tend to decrease the average Y_e, but with a minimal effect on nucleosynthetic yields (Radice et al., 2022). The exclusion of relativistic effects implies that we cannot accurately model jet formation, but the effects of these approximations on mass ejection and composition are likely minimal, since the relevant processes operate far from the BH. The leading order special relativistic corrections to the MHD equations are $\sim v/c$ for $v < c$, hence we estimate uncertainties associated with our fastest ejecta to be at least of the same order (e.g., 50% for matter with $v_r/c = 0.5$, etc.). The bulk of mass ejection has $v_r/c < 0.1$, and

thus uncertainties due to Newtonian physics should be on the order of 10%, comparable to those due to spatial resolution.

Chapter 6

HMNS Evolution

As discussed, a promising way to induce large quantities of high velocity, high electron fraction outflows is the inclusion of a finite lived remnant in our simulations. In most NS mergers, this remnant is a HMNS, expected to live for a timescale of $\sim 10-100$ ms post-merger, and driving additional outflows through magnetized and neutrino-driven winds before collapsing to a BH. To include a HMNS in our simulations, we require an initial thermodynamic profile, self-gravity, an EOS which can deal with densities near nuclear saturation, and an additional source of neutrinos from the HMNS in our leakage/absorption scheme. Here, we describe our implementation of the EOS and neutrino source terms.

6.1 Equation of State

We generate our EOS for use in `FLASH4.5` using the `SROEOS` generator (Schneider et al., 2017), which generates hot equations of state assuming an NSE prescription for subnuclear density material ($\lesssim 10^{11}$g cm^{-3}) , and was further modified by Schneider et al. (2019) to include the APR EOS. This involves

separating the matter into representative constituent species and minimizing the Helmholtz free energy of the combined gas. Material near or above nuclear densities ($\gtrsim 10^{11}$g cm^{-3}) uses a single nucleus approximation (SNA) for nuclei, where the properties of all present nuclei are represented by a single particle. To determine the energy of the gas, interactions between the nuclei are handled with either a Skyrme (Lattimer and Swesty, 1991) or APR (Akmal et al., 1998) prescription. The high and low density regimes are then stitched together with a derivative-preserving merge prescription, creating a seamless EOS across a large parameter space.

`FLASH4.5` requires all material to have a positive internal energy, but the nuclear binding energies of the material in NSE causes the total internal energy to be negative. Therefore, we leave the portion of the code handling nuclear densities unchanged, but modify the NSE part of the code to output the binding energy of material at a point in thermodynamic space (ρ, T, Y_e). This binding energy is then added on to the energy during the `FLASH4.5` MHD evolution so that differences in binding energy are still taken into account, but the internal energy of the fluid is never negative. We generate tables which span a space of $10^{-6} - 10^{15}$g cm^{-3} with 655 points in density, $10^4 - 10^{13}K$ with 256 points in temperature, and $0.005-0.660$ with 66 points in electron fraction. Additionally, the SNA portion of the code fails for numerical reasons at temperatures $T \lesssim 10^6$ K. To work around this, the merged code is separated in density space around nuclear density ($\sim 10^{11}$g cm^{-3}), and the table temperature minimum is set to be 10^6 K above the separation density, and 10^4 K below.

To use the tabulated EOS in `FLASH4.5`, we modify the implementation used by Couch and Ott (2013), included with the release of `FLASH4.5`, which is used for similar equations of state in CCSNe simulations (O'Connor and Ott, 2010).

In addition to modernization of the routines, the iterative Newton-Raphson solver is modified to be more robust against failure by adding a temperature change limiter, as well as adding the capability to handle the binding energies of nuclei. At each point in the evolution, the EOS iteratively solves for the temperature given a consistent Y_e, ρ, and $E_{\rm int}$ from the MHD solver. It then outputs the mass fraction of each species, and changes the internal energy accounting for the binding energies. The binding energy of elements are conglomerated into 3 species for use in simulations, α-particles, "light" elements, and "heavy" elements. Light elements consist of any elements with $Z < 6$ excluding α-particles, whereas "heavy" elements represent everything else ($Z > 6$). The average value of the heavy element mass and binding energy is then taken to be the sole representative "heavy" element which is evolved in `FLASH4.5`. As well, the code outputs a spatially varying adiabatic Γ_1 and γ_2 for use in the unsplit evolution, which determine the sound speed and relates pressure to the energy, respectively.

6.2 Neutrino Implementation

In this section we detail the implementation of additions to our neutrino scheme to include the effects of HMNS irradiation in the domain, in particular the effects of neutrino heating on the torus. Full details of the rest of the scheme are outlined in Chapter 4, Metzger and Fernández (2014) and Lippuner et al. (2017). The end goal of the implementation is a scheme accurate to within an order of magnitude with limited computation costs. It is well known that neutrino leakage schemes tend to under predict the lepton number change and energies in merger simulations (e.g., Foucart et al. 2020; Radice et al. 2022; Curtis et al. 2023a), and as such we do not attempt to create a totally quanti-

tatively accurate scheme.

We extend the previous implementation of the neutrino heating from a HMNS for heating fluid elements outside the neutrinosphere, which requires the location of the neutrinosphere, as well as the temperature and luminosity of the neutrino emission.

The explicit heating and cooling terms are given in the appendices of Fernández and Metzger (2013) and Metzger and Fernández (2014). What requires modification is the total neutrino luminosity input from the HMNS, which is then normalized by the blackbody radiation of the neutrinos at the neutrinosphere, and a radial component to account for the flux hitting the cell,

$$\bar{L}_{\nu_i} = \frac{L_{\nu_i}}{4\pi R_{ns,\nu_i}^2 \sigma_{SB} T_{ns,\nu_i}^4}. \tag{6.1}$$

In previous simulations, the neutrino luminosity L_{ν_i}, neutrinosphere temperature, T_{ns,ν_i}, and neutrinosphere radius $R_{ns,\nu}$ were user defined parameters, and we now make them self-consistent. We find the total luminosity of the HMNS by summing up the individual emissivities of each cell within the HMNS. The neutrinosphere radius is not assumed to be spherically symmetric, and is allowed to change with θ and ϕ. It is determined as the first location radially outwards at which the optical depth is less than or equal to 2/3,

$$R_{ns,\nu_i}(\theta,\phi) = R(\tau_{\nu_i} \leq 2/3). \tag{6.2}$$

The radial optical depth for each species is calculated along each direction using the numerical summation $\tau_{\nu_i} = \sum \kappa_{\nu_i}(r)\mathrm{d}r$, where we utilize the analytic expressions for κ from Ruffert et al. (1996), which include the effects of energy averaged scattering and absorption processes onto neutrons and protons. The

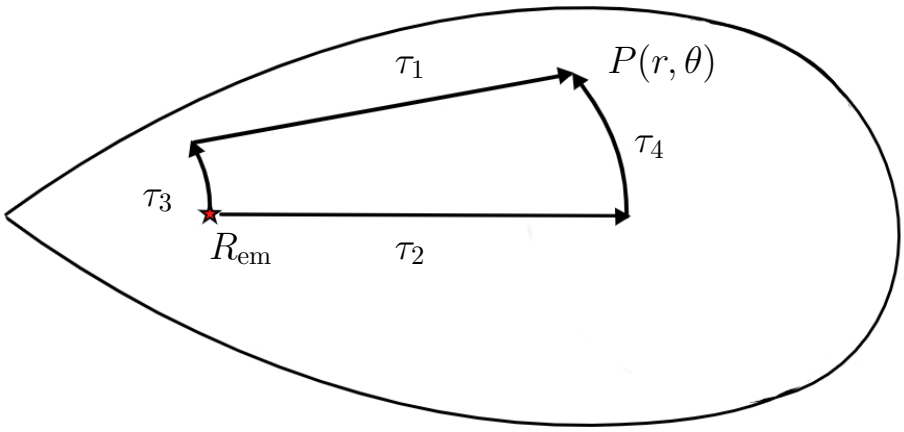

Figure 6.1: Integrated line of sight optical depths used in determining the reduction in self-irradiation heating from torus emission. The torus is taken to be a lightbulb which emits from two points slightly above and below the the midplane at a radius $R_{\rm em}$, to each point in the domain, $P(r,\theta)$

neutrino temperature is then determined from the average neutrino energy in the neutrinosphere

$$\langle \epsilon_{ns,\nu_i} \rangle = \sum Q^{\rm eff}_{\nu_i}(R_{ns}) / \sum R^{\rm eff}_{\nu_i}(R_{ns}), \tag{6.3}$$

$$\langle T_{ns,\nu_i} \rangle = \langle \epsilon_{ns,\nu_i} \rangle \frac{\mathcal{F}_4(0)}{\mathcal{F}_5(0)}, \tag{6.4}$$

where $Q^{\rm eff}_{\nu_i}$ and $R^{\rm eff}_{\nu_i}$ are the effective energy and lepton number change for each neutrino species, the explicit forms for which are defined in Fernández et al. (2019b), eq (3) and (4). The factors of the Fermi integrals, $\mathcal{F}_n(0)$ come from expanding the explicit forms of $Q^{\rm eff}_{\nu_i}$ and $R^{\rm eff}_{\nu_i}$.

The neutrino radiation is then further attenuated by a factor of $e^{-2\tau_{\nu_i}}$, where τ_{ν_i} is the radially integrated optical depth along the line of sight from the cell to the HMNS.

Within the neutrinosphere, the irradiation is identical, except that it relies on the spherically symmetric enclosed luminosity and temperature at each radial cell. These enclosed quantities are then used in equations (6.1-6.4) to calculate the normalized luminosity and the temperature used in the heating and lepton number change rates. In practice, however, the luminosity within the HMNS is dampened to negligible rates by the exponential of the massive opacities ($\tau_{\nu_i} \sim 10^4$), which drops steeply across one single cell at the HMNS neutrinosphere with our current resolution.

Additionally, we improve the lightbulb scheme for emission from the torus by integrating τ_{ν_i} for absorption from neutrinos emitted by the torus. While this is a subdominant effect compared to both cooling from the torus and irradiation from the HMNS, the previous scheme detailed in Chapter 4 has problems with high density tori after they experience shocks from the HMNS

oscillation. These shocks can artificially increase τ_{ν_i} in the outer regions of the torus, as the previous scheme used the value of τ_{ν_i} at the density maximum for the luminosity reduction in the entire torus.

We develop a simple new scheme which relies on integration of τ_{ν_i} in the radial and polar directions. First, we determine the 4 optical depths shown in Figure 6.1. The first is along the radial line of site from the emission maximum to each point (τ_1), the radial optical depth along the equator to the radius at which the point lies (τ_2), the angular optical depth from the torus equator to the emission maximum (τ_3) and to the point (τ_4). The optical depth is then taken to be the maximum of the two possible path lengths

$$\tau = \max(\sqrt{\tau_1^2 + \tau_3^2}), \sqrt{\tau_2^2 + \tau_4^2}). \tag{6.5}$$

to avoid issues with points around the HMNS where one of the path can have unphysically small optical depths. This is similar to other neutrino leakage schemes (e.g., Ruffert et al. 1996; Neilsen et al. 2014; Siegel and Metzger 2018; Werneck et al. 2023).

We compare snapshots of the net energy and lepton number change source terms from our scheme to the time stationary Monte-Carlo (MC) neutrino transport code `SedonuGR` (Richers et al., 2015, 2017) in Figure 6.2 and Figure 6.3. `SedonuGR` utilizes an MC algorithm accounting for emission, absorption, and scattering of neutrinos for a given fluid background and EOS to return the local energy and lepton number change rates for a fluid parcel. MC schemes are among the most accurate in the literature (e.g., Richers et al. 2015; Ryan et al. 2015; Richers et al. 2017; Miller et al. 2019; Foucart et al. 2020), so the source terms returned by `SedonuGR` are a good benchmark that we can compare our more approximate leakage/lightbulb scheme to. Snapshots from 2D slices

of our spherical domain at $t = 0, 1$ and 30 ms are taken as comparison points. The effects of neutrinos start to become negligible due to decreased emission and increased transparency as the torus dissipates, and for this reason, we focus our comparison at earlier timesteps, with earlier agreement being much more impactful.

The neutrino scheme recreates the overall energy and lepton number change rates to within a factor of a few, following a similar spatial distribution. As the scheme progresses, cooling of material is overestimated by an order of magnitude, especially in the midplane of the torus and close to the HMNS. We show this both with 2D colormaps, as well as a numerical comparison of the schemes by taking a radial slice through the domain at the equator, and a vertical slice at the density maximum of the torus. While it is difficult to extrapolate the effects of the discrepancies on our outflows, we can speculate that increased cooling near the midplane of the HMNS may result in less neutron rich material being ejected by magnetically driven outflows, which is also found by Curtis et al. (2023a) in their leakage scheme comparison. However, the majority of matter affected is also likely to be accreted upon HMNS collapse, as its small angular momentum causes it to circularize at a radius smaller than the ISCO upon collapse to BH.

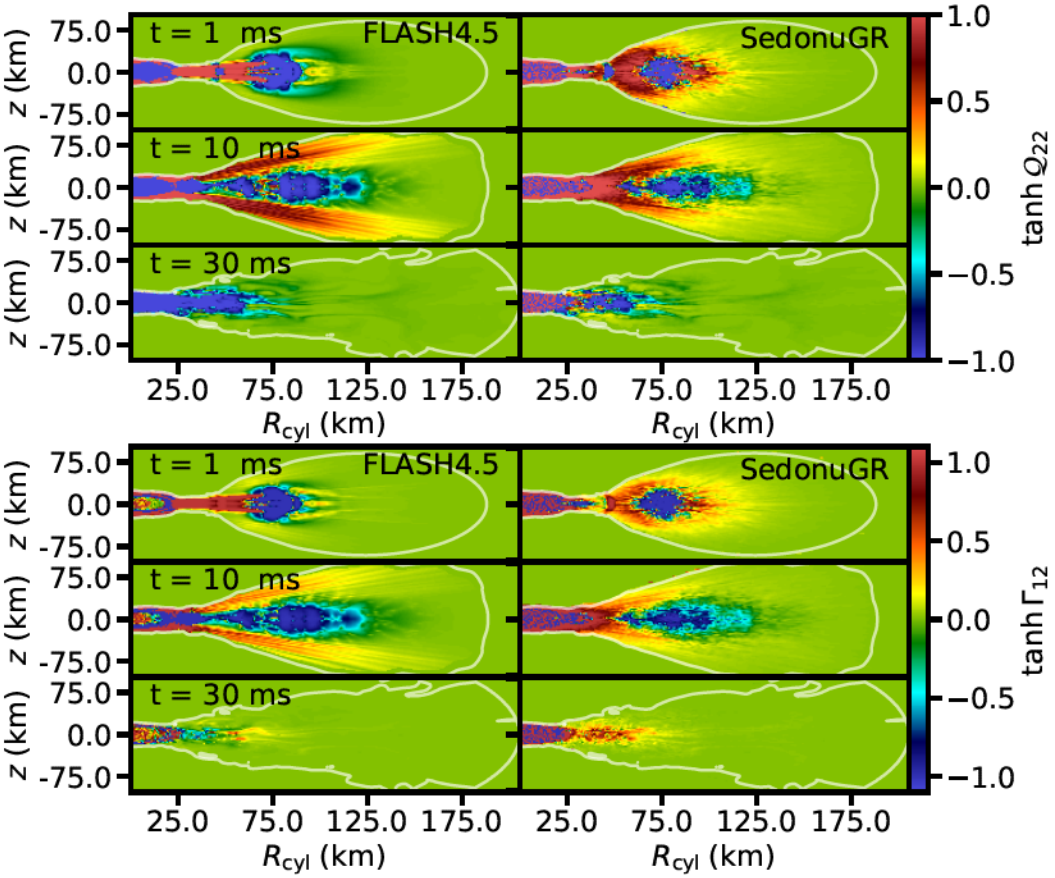

Figure 6.2: Comparison of neutrino source terms for a $0.1M_\odot$ torus and $2.65M_\odot$ HMNS at $t = 1, 10, 30$ ms in `FLASH4.5` (*Left*) to `SedonuGR` (*Right*). The top 6 panels compare rate of energy change per unit mass, and the bottom 6 panels show rate of lepton number change per baryon. The background fluid snapshot are taken as 2D slices at $\phi = 0$ from the `FLASH4.5` domain at the specified time, with the $10^9 \mathrm{g\,cm^{-3}}$ white contours delimiting the approximate edge of the torus, where the neutrino source terms are set to 0. The lightbulb/leakage scheme tends to underestimate the heating and lepton change at all times, leading to less energetic, lower Y_e neutrino driven outflows than in an MC scheme.

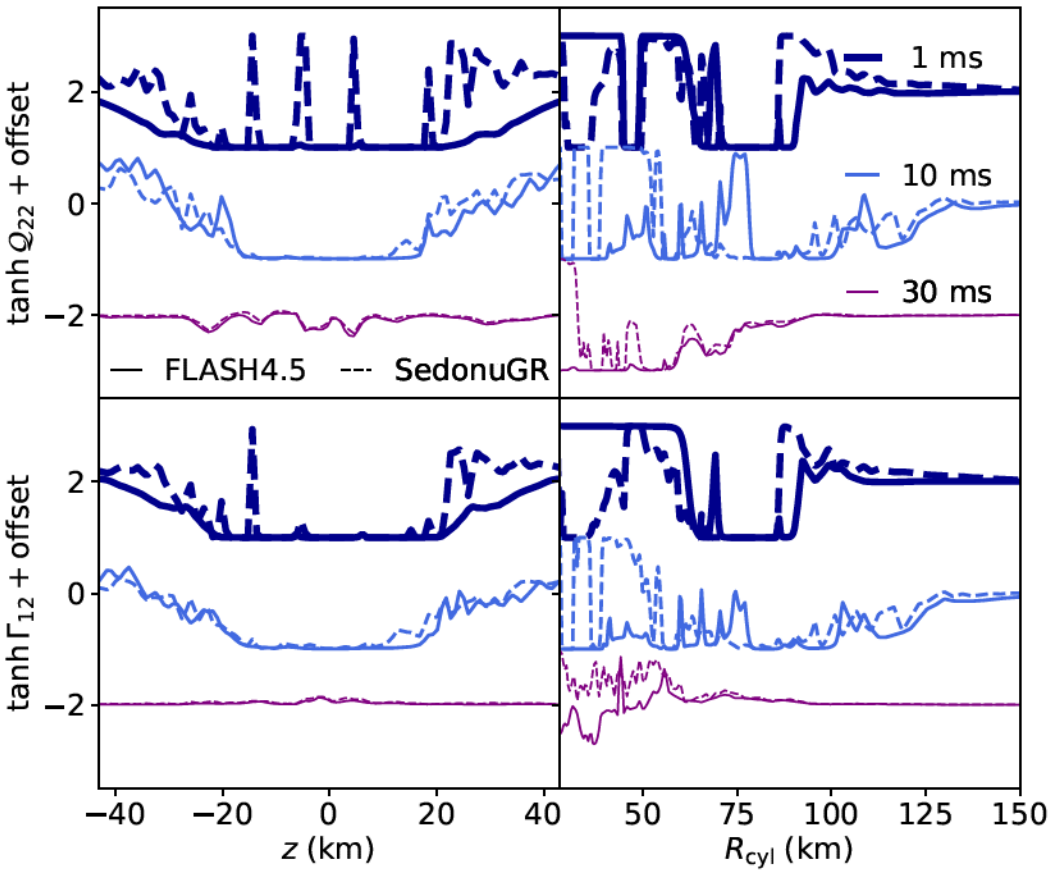

Figure 6.3: Comparison of neutrino source terms for a $0.1M_\odot$ torus and $2.65M_\odot$ HMNS at $t = 1, 10, 30$ ms in *Top*: Rate of energy change per unit mass, and *Bottom*: Rate of lepton number change per baryon. The absolute values of the source terms for $t = 1, 30$ ms have been offset by a constant (± 2) for each time for visual clarity. The background fluid snapshots are from the `FLASH4.5` domain at the specified time. *Left:* Vertical slices at $\phi = 0$ and $r = r_{\rm circ}$ (through the torus density maximum). *Right:* Radial slices at $\phi = 0$ and $\theta = 90$ (through the equator). The neutrino source terms from `FLASH4.5` are shown as solid lines, while the source terms from `SedonuGR` are dashed lines. Changing color and line thickness denote different time snapshots.

Chapter 7

Secular Outflows from 3D MHD Hypermassive Neutron Star Accretion Disk Systems

Simulations of BH torus systems suggest that winds from the disk can eject sufficient mass to power the red kilonova, but are lacking enough mass in high electron fraction ($Y_e \gtrsim 0.25$), high velocity ($v \gtrsim 0.25c$) outflows to create the blue kilonova. Several studies point to the formation of a short lived hypermassive NS (HMNS) as a resolution to the lack of this ejecta (e.g., Metzger et al. 2018; Fahlman and Fernández 2022; Combi and Siegel 2023; Curtis et al. 2023a).

At the time of writing this chapter, there are few long term simulations of 3D MHD HMNS systems, (e.g., Kiuchi et al. 2012; Siegel et al. 2014; Ciolfi and Kalinani 2020; Mösta et al. 2020; de Haas et al. 2022; Combi and Siegel 2023; Curtis et al. 2023a) with only one simulation lasting ~ 1 s (Kiuchi et al., 2022). The varying input neutrino physics, HMNS lifetimes, and magnetic

fields strengths and orientations result in little consensus on the composition, mass, velocities and ejection mechanisms for their outflows.

Here we present long-term 3D MHD numerical simulations of HMNS and torus systems, starting from varying idealized initial conditions. We utilize a (pseudo)Newtonian potential (Artemova et al., 1996), the nuclear APR EOS (Schneider et al., 2019), and a leakage/absorption scheme to handle energy deposition and lepton number change from neutrinos, as described in Section 7.1. In Section 7.2 we examine our outflows in the context of powering a kilonova while ignoring effects from relativistic jets, which we are unable to model without full GR. In Section 7.3 we compare to other works and in Section 7.4 we conclude. Chapter 6 describes updates to our previously used neutrino scheme to handle a HMNS fully contained in the computational domain.

7.1 Methods

7.1.1 Numerical MHD

We use a modified version of the `FLASH4.5` code to run our MHD simulations in non-uniform 3D spherical coordinates, as described in Chapters 2. Here we give a brief overview. The code solves the Newtonian conservation equations for mass, momentum, energy, and lepton number, as well as the induction

equation

$$\frac{\partial \rho}{\partial t} + \nabla \cdot [\rho \mathbf{v}] = 0 \tag{7.1}$$

$$\frac{\partial (\rho \mathbf{v})}{\partial t} + \nabla \cdot [\rho (\mathbf{v} \otimes \mathbf{v}) - (\mathbf{B} \otimes \mathbf{B})] + \nabla P = -\rho \nabla \Phi \tag{7.2}$$

$$\frac{\partial (\rho E)}{\partial t} + \nabla \cdot [\mathbf{v}(\rho E + P) - \mathbf{B}(\mathbf{v} \cdot \mathbf{B})] = -\rho \mathbf{v} \cdot \nabla \Phi + Q_{\rm net} \tag{7.3}$$

$$\frac{\partial (\rho Y_e)}{\partial t} + \nabla \cdot [\rho Y_e \mathbf{v}] = \Gamma_{\rm net}, \tag{7.4}$$

$$\frac{\partial \mathbf{B}}{\partial t} + \nabla \cdot [\mathbf{v} \otimes \mathbf{B} - \mathbf{B} \otimes \mathbf{v}] = 0. \tag{7.5}$$

where ρ is the density, $\mathbf{v}$ is the velocity, $\mathbf{B}$ is the magnetic field (including a normalization factor $\sqrt{4\pi}$) , Y_e is the electron fraction, and E is the total specific energy of the fluid

$$E = \frac{1}{2} (\mathbf{v} \cdot \mathbf{v} + \mathbf{B} \cdot \mathbf{B}) + e_{\rm int}. \tag{7.6}$$

We denote $e_{\rm int}$ the specific internal energy, and P is the sum of gas and magnetic pressure

$$P = P_{\rm gas} + \frac{1}{2} \mathbf{B} \cdot \mathbf{B}. \tag{7.7}$$

We use the constrained transport method (Evans and Hawley, 1988) to preserve the solenoidal condition ($\nabla \cdot \mathbf{B} = 0$) while evolving the induction equation. We include source terms from the self-gravitating potential of the fluid, Φ, neutrino heating and cooling, $Q_{\rm net}$, and lepton number change, $\Gamma_{\rm net}$. Our self-gravity scheme utilizes the Newtonian multipole solver of Müller and Steinmetz (1995), as implemented in Fernández et al. (2019a). After the HMNS collapses into a BH, we add a point source term with the mass of the remnant to the zeroth

moment of the multipole expansion using the Artemova potential (Artemova et al., 1996). We close the equations with the hot APR EOS of Schneider et al. (2019). The additional source terms from our neutrino scheme are calculated using a 3 species, two source, lightbulb-leakage scheme (Metzger and Fernández, 2014; Lippuner et al., 2017; Fernández et al., 2022). We use local emission rates from Bruenn (1985) for neutrino production from charged-current interactions, and the rates from Ruffert et al. (1997) for plasmon decay, nucleon-nucleon brehmsstrahlung, and pair processes. We take into account absorption due to charged-current weak interactions from electron-type neutrinos and antineutrinos emitted by the central HMNS and by a ring within the torus. The implementations of our neutrino source terms are detailed in Chapter 6.

7.1.2 Initial Torus

We initialize our simulations with a constant specific angular momentum, entropy, and composition torus in hydrostatic equilibrium with a point mass remnant in a Newtonian potential. Generating the torus requires choosing input parameters, which we set according to inferred values from GW170817 (See e.g., Abbott et al. 2017; Shibata et al. 2017; Fahlman and Fernández 2018). For all our simulations, we set a remnant mass of $2.65 M_\odot$, torus mass of $0.1 M_\odot$, radius of density maximum at 50 km, entropy of $s = 8\, k_b$/baryon and $Y_e = 0.1$. This results in a torus with an initial maximum density $\rho_{\max} = 8 \times 10^{10}\, \mathrm{g\, cm^{-3}}$. Matter initialized in the torus is flagged as torus material using a passive mass scalar which is advected with the flow. We neglect the self-gravity of the torus in the initialization process, as the system mass is dominated by the remnant. We additionally neglect spatial variations in the composition and entropy, which have been found to make small ($\sim 10\%$) differences in the outflows around BH

accretion disks (Fernández et al., 2017; Nedora et al., 2021; Fujibayashi et al., 2020b,c; Most et al., 2021).

The torus is then threaded with a magnetic field. We choose magnetic field configurations that cover possible geometries found in magnetized merger simulations, which generally yield a combination of (turbulent) toroidal and poloidal fields. Due to the high resolution requirements to capture the mechanisms for amplifying the field at merger and within the remnant plus torus (e.g., the Kelvin-Helmholtz instability and MRI), we start with field strengths that assume that growth and saturation has been reached, allowing us to resolve the smallest growing wavelength of the MRI with our grid (See Figure 7.1 and Section 7.1.5). These field strengths are similar to those found in merger simulations which use sub-grid models to resolve these effects (e.g., Aguilera-Miret et al. 2023). For models which specify a poloidal field geometry, this is initialized using an azimuthal vector potential that follows the density,

$$A_\phi \propto \max(\rho - \rho_0, 0) \tag{7.8}$$

where $\rho_0 = 0.009\rho_{\max}$ is the cutoff density used to ensure the field is embedded in the torus. This results in a poloidal ("SANE") field topology (Hawley, 2000). The field is normalized to be dynamically unimportant, with an average plasma β of

$$\langle\beta\rangle = \frac{\int P_{\rm gas} \mathrm{d}V}{\int P_{\rm mag} \mathrm{d}V} = 100, \tag{7.9}$$

resulting in a maximum field strength of $|B_r| \sim |B_\theta| \sim 4 \times 10^{14}\,\mathrm{G}$. Models with a toroidal field geometry are initialized as

$$B_\phi = B_0 \max(\rho - \rho_0, 0), \tag{7.10}$$

where $B_0 = 5 \times 10^9\,\mathrm{G}/(\mathrm{g\,cm^{-3}})$. This results in nearly constant azimuthal magnetic field embedded within the torus, which tapers off as a function of the density profile. The field has a maximal value of $8 \times 10^{14}\,\mathrm{G}$, and an average strength of $\sim 2 \times 10^{14}\,\mathrm{G}$.

7.1.3 Initial HMNS

Our torus orbits a stable equilibrium model of an azimuthally-symmetric, differentially-rotating NS. We find 2D HMNS thermodynamic profiles using the code `NewtNeut`, a reduced version of the code `drns` (Stergioulas and Friedman, 1995). `NewtNeut` generates differentially-rotating high-density stars in the Newtonian limit, taking a central density, rotation law, and EOS as input, and utilizing the self-consistent field method of Hachisu (1986, HSCF) to generate thermodynamic profiles for a differentially rotating non-relativistic star. The equilibrium equation that the HSCF method solves is

$$\int \rho^{-1} \mathrm{d}P = C - \Phi_g + \int \Omega^2(r_{\mathrm{cyl}}) r_{\mathrm{cyl}} \mathrm{d}r_{\mathrm{cyl}}, \tag{7.11}$$

where Φ_g is the (Newtonian) gravitational potential, and Ω is a choice of rotation profile dependent on r_{cyl}, the cylindrical radial coordinate. We use the well studied j-const rotation law (Hachisu, 1986; Baumgarte et al., 2000)

$$\Omega = \frac{\Omega_0}{(1 + \hat{A}^2 \hat{r}^2 \sin^2\theta)}, \tag{7.12}$$

where Ω_0 is the central rotation rate, $\hat{A} = A/r_e$ is a scaling constant which sets the amount of differential rotation, and $\hat{r} = r/r_e$ is the radial coordinate normalized to the equatorial radius of the star. We use a uniform spherical grid with a resolution of $(N_r \times N_\theta) = (200 \times 200)$ to generate one quadrant of the

NS, and then assume azimuthal and equatorial symmetry to generate the rest of the star. The HSCF method requires finding the quantity $\int \rho^{-1} \mathrm{d}P$, which can be obtained from the enthalpy,

$$h = \int \rho^{-1} \mathrm{d}P + \int T \mathrm{d}S, \tag{7.13}$$

as long as our star satisfies the barotropic condition $T\mathrm{d}S = 0$. We choose to generate stars of constant entropy, so that neutrino emission is not suppressed by a zero temperature initial condition. Our choice of constant angular momentum differential rotation law and constant entropy are not entirely correct for the remnant of a NS-NS merger, as more realistic neutron stars follow a rotation law that peaks away from the central density, (e.g., Hanauske et al. 2017; Iosif and Stergioulas 2022) and have varying spatial entropy (e.g., Most et al. 2021; Nedora et al. 2021).

The generated HMNS has a mass $2.65 M_\odot$, entropy $s = 2\,k_\mathrm{B}$/baryon, with $\hat{A} = 0.5$, and the central rotation rate chosen such that the ratio of polar to equatorial radius is $r_p/r_e = 0.75$. This makes a star with a maximal equatorial radius and central rotation rate of 23.5 km and $3780\,\mathrm{rad\,s^{-1}}$, respectively, corresponding to a period of $\sim$ 1.6 ms. The thermodynamically consistent axisymmetric density, electron fraction, temperature, internal energy, and rotational velocity profile output from `NewtNeut` are read into `FLASH`, and the relevant quantities are linearly interpolated to the cell centers to create our initial HMNS. Like the torus, HMNS matter is also flagged using a passively advected mass scalar. In all our runs, we embed the HMNS with a dynamically unimportant axisymmetric toroidal field that vanishes as we approach the origin, as motivated by merger simulations (Shibata et al., 2021b). The HMNS

field is given by

$$B_\phi = B_{NS}\left(\frac{r}{r_e}\right)^2 \max(\rho - \rho_0, 0) \tag{7.14}$$

where $\rho_0 = 5 \times 10^{13}\,\mathrm{g\,cm^{-3}}$ is 1/10 the central density of the HMNS, and the constant $B_{NS} = 8 \times 10^4\,\mathrm{G}/(\mathrm{g\,cm^{-3}})$ is set such that the total magnetic energy within in the NS is $2 \times 10^{47}\,\mathrm{erg}$. We note that the magnetic field geometry is no longer toroidal by $t \sim 5\,\mathrm{ms}$, as it is modified by the dynamics inside the HMNS.

7.1.4 Tracer Particles

Tracer particles are used to track nucleosynthesis in post-processing. We initialize 10,000 tracer particles by placing them into pseudorandom positions within the domain, following the density distribution, where the density falls between $10^6 \leq \rho \leq 10^{13}\,\mathrm{g\,cm^{-3}}$ and the atmospheric fraction is 0. This ensures that the particles are embedded within the torus and the edges of the HMNS, but also that few are trapped in the HMNS when it collapses. Particles are then advected with the fluid flow, and the history of any particles that make it past a fixed extraction radius r_{out} are used in nucleosynthesis calculations. The latter are carried out with the publicly available nuclear reaction network `SkyNet` (Lippuner and Roberts, 2017), with the same settings as Fernández et al. (2020).

7.1.5 Computational Domain

We solve the MHD equations in spherical polar coordinates (r, θ, ϕ) on a domain initially ranging from an inner boundary at $r_{\mathrm{min}} = 0\,\mathrm{km}$ to an outer radius

$r_{\rm max} = 10^5\,{\rm km}$, located far away from the central remnant. Both the polar (θ) and azimuthal (ϕ) domains subtend an angle from 0 to π, creating a hemisphere.

Upon collapse of the HMNS, we excise an integer number of cells covering a radial region interior to a new radius $r_{\rm min}$, located approximately halfway between the event horizon and ISCO of the newly formed BH. To preserve the total number of radial cells in the grid, the domain is expanded outwards in radius by the same number of cells removed around the origin, with the new cells filled with ambient medium. Since no ejecta has reached the outer radial boundary at the collapse times, this results in no effective change to the simulation outside $r_{\rm min}$. For all models, this results in a post-collapse value of $r_{\rm min} = 15.4\,{\rm km}$ and an outer boundary at $r_{\rm max} = 5.23 \times 10^5\,{\rm km}$.

We use a logarithmic grid in the radial direction, a grid evenly spaced in $\cos\theta$ in the polar direction, and uniform spacing in azimuth. To avoid issues with time stepping close to the singularity, we make the innermost radial cell large, with a size of 3 km, encompassing the inner $\sim$13% of the HMNS radius. We set our polar and azimuthal resolution such that the initial wavelength of the most unstable mode of the MRI within the torus is resolved with ~ 10 cells, and set a radial resolution to get approximately square cells in the midplane of the torus. This results in a mesh size of $(N_r \times N_\theta \times N_\phi) = (580 \times 120 \times 64)$, focused towards the midplane of the disk, with $\Delta r/r \sim 0.018$, $\min(\Delta\theta) \sim 0.017$, and $\Delta\phi \sim 0.1$. We show the MRI quality factor (Sano et al., 2004) for both our initial setups in Figure 7.1.

The boundary conditions of our domain are periodic in the azimuthal direction, and reflecting along the polar axes. The outer radial boundary is set to outflow, while the inner radial boundary is initially reflecting while the HMNS survives. After collapse, we set the inner radial boundary to outflow so matter

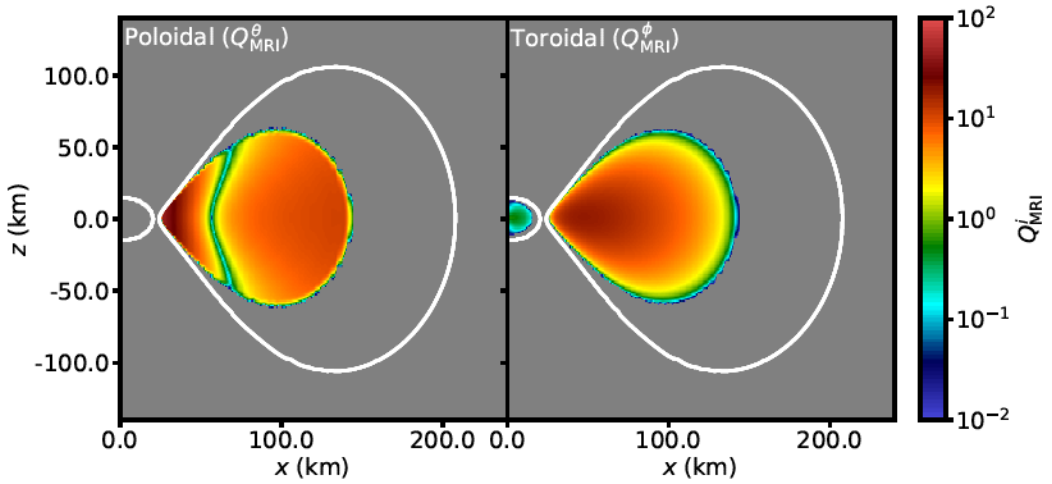

Figure 7.1: Slices of the MRI Quality parameter ($Q^i_{\rm MRI} = \lambda^i_{\rm MRI}/\Delta\ell_i$), where $\lambda^i_{\rm MRI}$ is the wavelength of the most unstable mode of the MRI and $\Delta\ell_i$ is the cell width in the specified i-th direction. Slices are in the $x-z$ ($\phi = 0$) plane of the *Bpol-t30* and *Btor-t30* models at initialization. The solid white lines mark the $3 \times 10^8\,{\rm g\,cm^{-3}}$ density contour, corresponding to near the edge of the torus and HMNS. Gray colour denotes regions without any magnetization in the relevant direction. The field is well embedded within the torus, and is generally resolved by at least 10 cells. The toroidal field in the HMNS is not well resolved due to the high densities, and as such we do not expect to resolve magnetized outflows driven by MRI turbulence in the remnant.

can accrete onto the BH.

7.1.6 Floor

To avoid issues with convergence, finite volume codes implement density floors. We impose a spatial and temporal varying floor to prevent computationally unfeasible low timesteps in magnetized regions near the inner boundary and rotation axis, while not affecting dynamics of the outflows. We implement the functional form used in Fahlman and Fernández (2022)

$$\rho_{\rm floor,A} = \rho_{\rm sml}\left(\frac{r}{20\,{\rm km}}\right)^{-3}\left(\frac{1}{\sin\theta}\right)^{0.75}\left(\frac{\max[t, 0.1\,{\rm s}]}{0.1\,{\rm s}}\right)^{-1.5}, \tag{7.15}$$

where $\rho_{\rm sml} = 2 \times 10^4\,{\rm g\,cm^{-3}}$. When the code reaches a density below the floor value in that cell, we add atmospheric material to raise it back up. Identical floors are implemented for pressure and internal energy, with the respective scaling constants $P_{\rm sml} = 2 \times 10^{14}\,{\rm erg\,cm^{-3}}$ and $e_{\rm sml} = 2 \times 10^{11}\,{\rm erg\,g^{-1}}$. In the magnetized polar funnel close to the black hole, we find that this restriction is often too low, but raising the floor results in unphysical effects in important areas of the flow. To address this, we impose an alternative floor on the density only that is dependent on the magnetization, as in Fernández et al. (2019b)

$$\rho_{\rm floor,B} = \begin{cases} \frac{P_{\rm mag}^2}{\zeta c^2}, & r < 200\,{\rm km} \\ 0, & r \geq 200\,{\rm km} \end{cases} \tag{7.16}$$

where we find $\zeta = 2$ a reasonable value to increase the timestep in the magnetized funnel, without affecting the dynamics in the disk. We then impose the floor

$$\rho_{\rm floor} = \max[\rho_{\rm floor,A}, \rho_{\rm floor,B}] \tag{7.17}$$

7.1.7 Models

Our models are summarized in Table 7.1. We choose parameters for the torus and HMNS which are the most likely properties of the remnant + disk system for GW170817 (e.g., Abbott et al. 2017; Shibata et al. 2017; Fahlman and Fernández 2018), while varying the lifetime of the remnant and the initial field topology.

Table 7.1: Simulation Parameters. From left to right, they list the name of the model, the mass of the remnant, the lifetime of the HMNS, the initial mass of the torus, the peak magnetic field strength in the torus, and the magnetic field geometry.

Model	$M_{\rm remnant}$ ($M_\odot$)	$\tau_{\rm HMNS}$ (ms)	$M_{\rm t}$ ($M_\odot$)	$\|\|\mathbf{B}\|\|$ (G)	**B** geom
Bpol-t30	2.65	30	0.10	4×10^{14}	pol
Bpol-t100		100			
Btor-t30		30			tor
Btor-t100		100			

7.1.8 Outflows

We calculate the total outflow by temporally integrating the mass flux passing through an extraction radius $r_{\rm out}$,

$$M_{\rm out} = \int_t \iint_{A_r} (\rho v_r {\rm d}A_r){\rm d}t, \tag{7.18}$$

where $A_r = \iint r^2 \sin\theta {\rm d}\theta {\rm d}\phi$ is the area of the cell face. After testing various extraction radii, we choose $r_{\rm out} = 1000\,{\rm km}$ as a radius where unbound matter has minimal interaction with the atmosphere, which can impact the energy of the ejecta, as well as being far away from the edges of the viscously spreading disk at late times, but close enough for most ejecta to cross during the simulation time. Matter is considered unbound if it has a positive Bernoulli parameter at the extraction radius

$$\Phi_g + e_{\rm int} + e_{\rm k} + e_{\rm mag} + \frac{P_{\rm gas}}{\rho} > 0, \tag{7.19}$$

and we discount any "atmospheric" matter that is present due to the requirement of the non-zero floor (§7.1.6).

We tabulate the ejecta in terms of total, "blue" ($Y_e \geq 0.25$), and "red" ($Y_e < 0.25$) outflows, based on the characteristic division between lanthanide-poor and lanthanide-rich material found in parametric nuclear network calculations (e.g., Lippuner and Roberts 2015; Kasen et al. 2015). The mass weighted averages of electron fraction and radial velocity,

$$\langle Y_e \rangle = \frac{\int_t \iint_{A_r} (\rho v_r Y_e \mathrm{d}A_r)\mathrm{d}t,}{M_{\rm out}} \tag{7.20}$$

$$\langle v_r \rangle = \frac{\int_t \iint_{A_r} (\rho v_r v_r \mathrm{d}A_r)\mathrm{d}t,}{M_{\rm out}} \tag{7.21}$$

are shown alongside the mass outflows in Table 7.2.

Throughout this paper, we identify material that is ejected through different mechanisms using the energy and entropy of the ejecta. Regions with large neutrino heating source terms are imparted with large internal energies and entropies, which we identify as neutrino driven winds. Conversely, fast, low-entropy material from regions with small neutrino heating source terms and high magnetization are identified as purely MHD driven. Passive tracer particles are also used to track the source terms applied to them as they are ejected and corroborate the identification of different mass ejection mechanisms.

7.2 Results

7.2.1 Overview of HMNS Outflows

We show the mass outflow rates and cumulative mass outflows for all models in Figure 7.2. Mass ejection is dominated by the torus ($\gtrsim 99\%$), although the

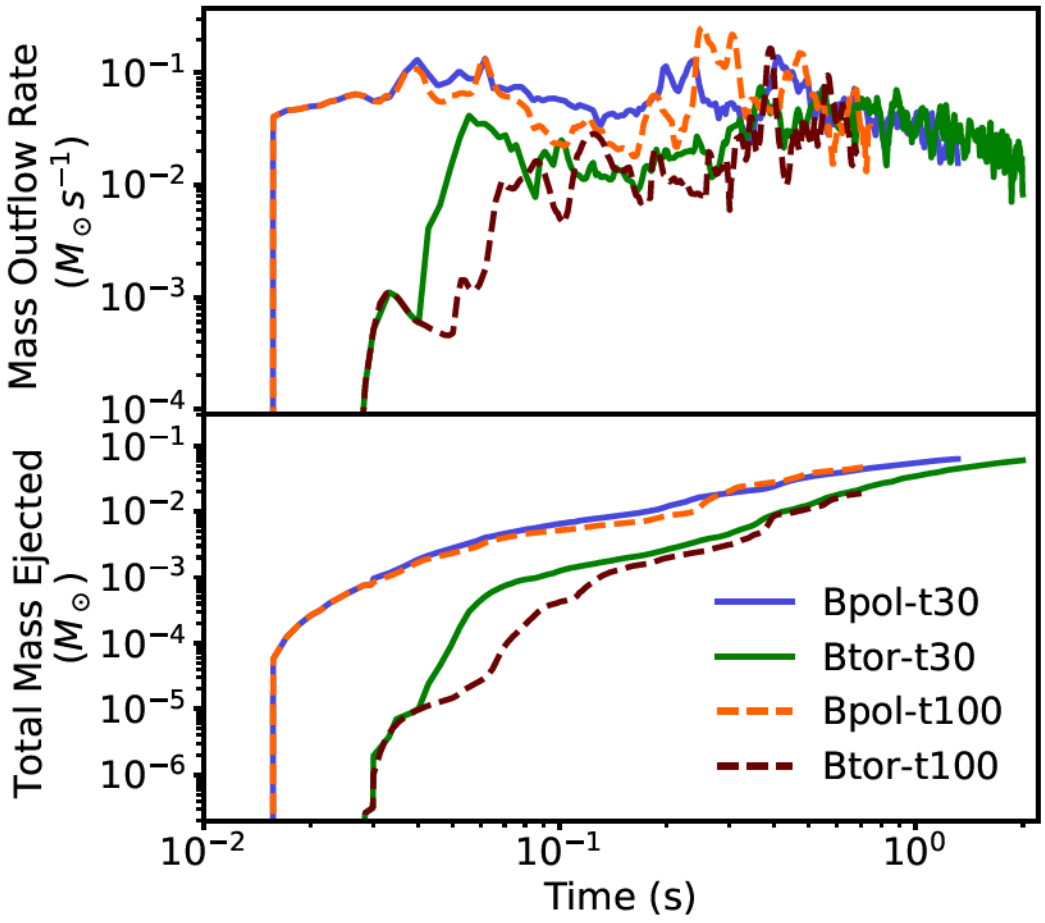

Figure 7.2: *Top:* Unbound mass outflow rates in our simulations at a radius of $r = 1000\,\mathrm{km}$. *Bottom:* Cumulative ejected mass in the simulations.

HMNS provides additional channels. During the first $\sim 30\,\mathrm{ms}$ of evolution, the HMNS ejects mass through mechanical oscillations, which induces noticeable pressure waves in the torus. Viscous spreading from the action of the MRI and the HMNS oscillations drives the center of mass of the torus out from $\langle r_{\mathrm{CM}} \rangle \sim 10\mathrm{km}$ by a factor of 2-4, depending on the initial field geometry and lifetime of the HMNS, and the lower density edges of the torus develop turbulent structures.

The initial sharp increase in mass outflow rate shown in Figure 7.2 is dominated by ejection through MHD stresses in the torus that are dependent on the initial magnetic field geometry, as seen in BH-tori simulations (Christie et al., 2019; Siegel et al., 2019; Fahlman and Fernández, 2022; Curtis et al., 2023b). The large scale poloidal field generates characteristic "wings" in the first $\sim 30\,\mathrm{ms}$, whereas the toroidal field takes an additional ($\sim 50\,\mathrm{ms}$) for dynamo action to convert the geometry into large scale poloidal structures, which then drives outflows. Material ejected through MHD stresses tends to have a wide range of electron fractions and velocities, spanning $Y_e \sim 0.1 - 0.5$, and $v \sim 0.05 - 0.6c$. The majority of MHD-driven and neutrino-driven winds are imprinted in the levels showing $t \lesssim 500\,\mathrm{ms}$ in the cumulative mass histograms of Figure 7.3, with the transition to purely thermally driven outflows (§7.2.2) happening around the $500\,\mathrm{ms}$ mark.

Also in the first $30 - 100\,\mathrm{ms}$, depending on the HMNS lifetime, high-entropy ($s \sim 100\,k_{\mathrm{B}}/\mathrm{baryon}$), magnetically- and neutrino-driven outflows are driven from the edges of the torus, which achieves electron fractions $Y_e \gtrsim 0.3$ and velocities $v \gtrsim 0.5c$. As illustrated by the angular histograms of Figure 7.3, this material is preferentially ejected in a cone of opening angle 50°, centered on the angular momentum axis (the polar regions). It is dominated by matter from

the torus, with ~ 30 times more ejecta from the torus than from the HMNS.

Figure 7.4 and the leftmost panels of Figure 7.5 show the matter density around the HMNS just before collapse. A magnetized funnel is formed while the HMNS survives, but there remains a significant amount of matter in the funnel with densities $\rho \sim 10^6 - 10^8\,\mathrm{g\,cm^{-3}}$ from HMNS oscillations and accreting matter, leading to the absence of steady-state, high velocity, collimated magnetic "tower" outflows from the HMNS (the so called "baryon loading problem"). After collapse of the HMNS, the polar regions become evacuated of matter and sit on our imposed density floor, so we cannot draw conclusions on whether or not matter would be launched post-collapse.

Shown in Figure 7.6 is the spatial distribution of ejecta Y_e for models *Bpol-t30* and *Btor-t30*. The aforementioned magnetized neutrino-driven winds are visible as high Y_e matter in the polar regions, common to all models. The average Y_e of the torus differs between models over the interval $t \sim 10 - 400$s from differences in accretion physics during this phase. Due to the susceptibility of the poloidal field to the MRI, the *Bpol* models begin accretion onto the HMNS earlier and at a higher rate than the *Btor* models, and feedback from accretion creates eddies of a size similar to the scale height of the torus. This expansion lowers the average density, thus lowering the attenuation of HMNS irradiation by matter, and mixes irradiated material from the accretion flow back into the dense regions of the torus. This results in an increase in the average electron fraction to $Y_e \sim 0.35$ in the densest midplane of the torus, as compared to $Y_e \sim 0.2$ in the *Btor* runs.

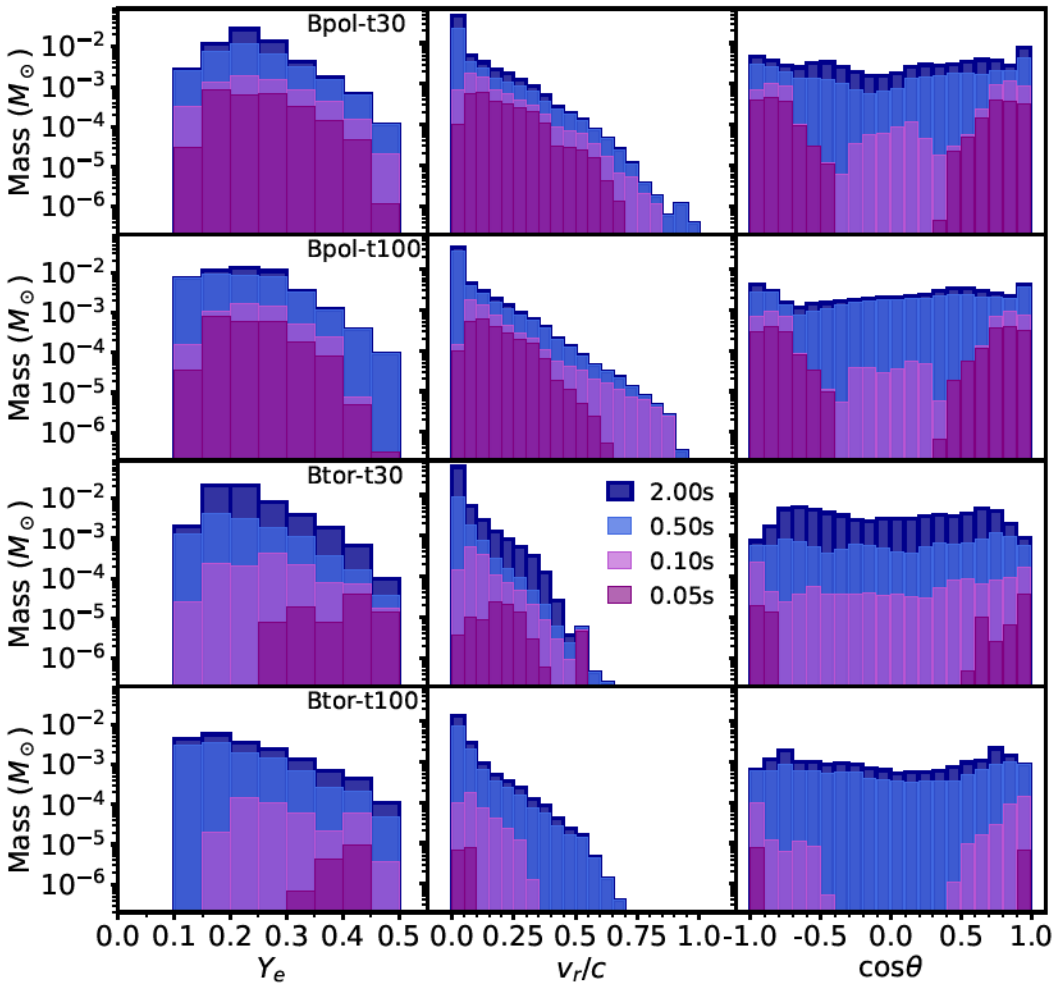

Figure 7.3: Total unbound mass ejected by our simulations at the extraction radius, binned into electron fraction Y_e,radial velocity v_r, and polar angle θ. The bin sizes are $\Delta Y_e = 0.05$, $\Delta v_r/c = 0.05$, and $\Delta \cos\theta = 0.1$, where $\cos\theta = 0$ is the midplane. Accounting for the time taken for the ejecta to reach the extraction radius, ($r_{\rm out}/v_{\rm r} \lesssim 70\,{\rm ms}$), the 0.1 s, 0.5 s and 2.0 s bins are populated by ejecta launched post-collapse in the *Bpol-t30* and *Btor-t30* models. Similarly, the 0.5 s and 2.0 s bins are comprised of mainly post-collapse ejecta in the *Bpol-t100* and *Btor-t100* models.

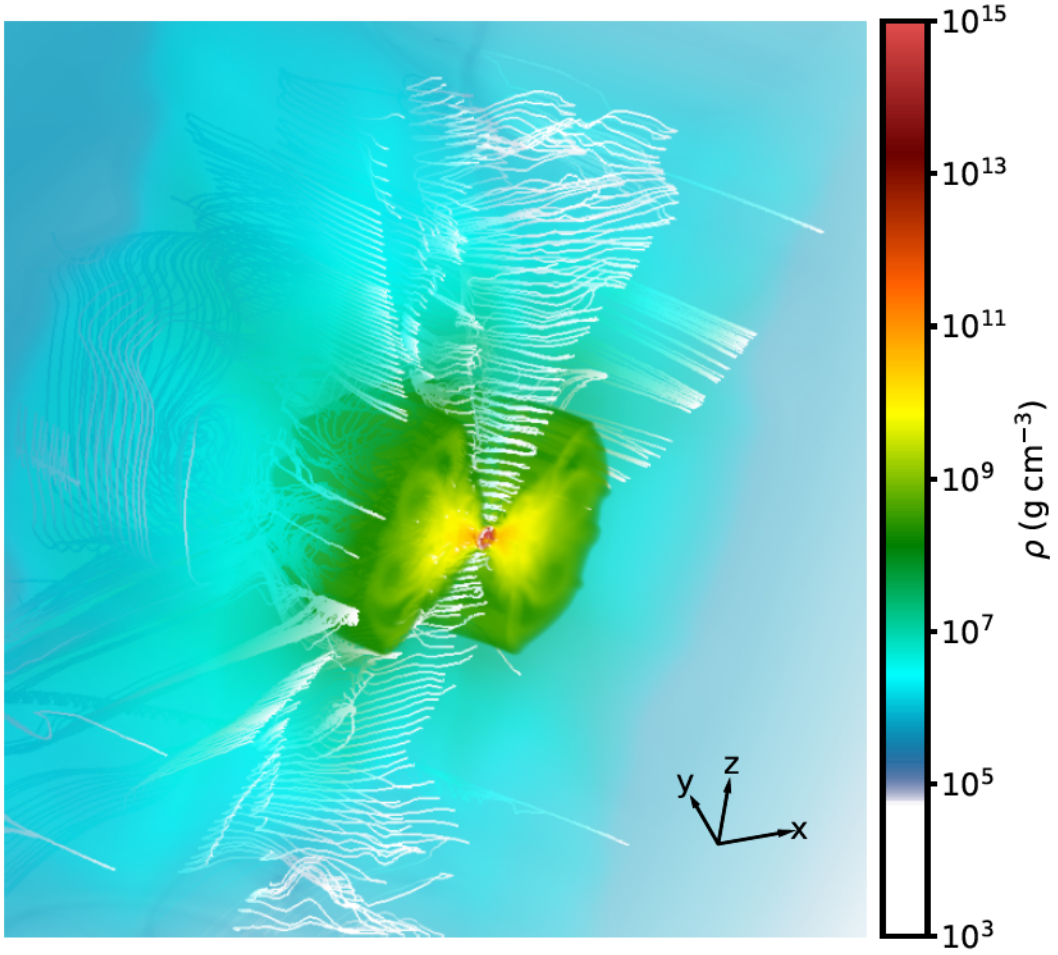

Figure 7.4: Volume rendering of the *Bpol-t30* run at $t = 30\,\mathrm{ms}$, right before the HMNS collapse to a BH is initiated. Colors show the density with increasing transparency as the density decreases. The visible outer edge of the torus in green ($\sim 10^8 \mathrm{g\,cm^{-3}}$) is located $\sim 350\,\mathrm{km}$ from the remnant in the midplane. Magnetic field streamlines are shown in white. Note the formation of a lower density, highly magnetized funnel along the spin axis of the HMNS.

7.2.2 Overview of Post-Collapse Outflows

After we trigger the collapse of the HMNS, the system then resembles a BH-torus system. In all cases, there is an increase in outflow caused by a magnetized shock wave launched by the collapse of the HMNS, and a subsequent settling into steady accretion onto the newly formed BH. This effect shows up most prominently in the *Btor-t30* model, where it is not masked by other outflows, and is noticeable as a spike in mass ejection at $t \gtrsim 30\,\mathrm{ms}$ in Figure 7.2. In the *Bpol-t30* case, we find that expansion of the torus due to the action of the MRI causes $\sim 10\%$ of the torus mass to not have enough angular momentum to maintain its orbit, plunging into the BH on a timescale of $\lesssim 1$ ms after collapse. For the *Btor-t30* run, we find that only 1% of material is caught in the collapse, in comparison. This is a result of disk spreading and accretion induced by the MRI taking longer to initiate, as well as comparatively weaker initial magnetically driven outflows, resulting in a much more compact torus configuration - the torus centroid is located only 1.1 times further out than its initial position, as opposed to the 2.2 times increase in the *Bpol-t30* case. For the longer-lived HMNS cases, *Bpol-t100* and *Btor-t100*, the longer time for accretion and viscous spreading to occur causes even more mass to be lost upon collapse, $\sim 25\%$ and $\sim 15\%$, respectively, of the torus is accreted instantaneously.

In all cases, material that is ejected by $t \gtrsim 600\,\mathrm{ms}$ is very similar to that of previous BH-torus studies in (GR)MHD, and tends to be in stochastic, slow ($v \lesssim 0.1c$) MRI turbulence driven outflows, with an electron fraction of $Y_e \sim 0.2 - 0.3$ set by the equilibrium value in the torus (see e.g., Siegel and Metzger 2018). The thermally driven outflows are noticeable as a peak in the velocity and electron fraction histograms in Figure 7.3 at $v \sim 0.05c$ and $Y_e \sim 0.2$.

The total mass ejected asymptotes to similar values at times $t \sim 1$s in both *Bpol-t30* and *Btor-t30*, although a significantly larger fraction (factor 2, in comparison) of that mass is contained in redder, slower outflows in *Btor-t30*. While the average electron fraction remains the same in the blue outflows between the two runs, they too tend to be about half as fast in the toroidal model.

Both *Bpol-t100* and *Btor-t100* are very similar to their 30 ms counterparts. Although they are run for a shorter amount of simulation time ($t \sim 0.5$ s), cumulative mass ejection and mass ejection rates match those from their counterparts well at that time, and we do not expect large differences in the thermally driven outflows past this point in time. This is explained by mass ejection being dominated by MHD stresses in the torus at early times ($t \lesssim 100$ ms) and thermal outflows at late times ($t \gtrsim 400$ ms), the latter being mostly unaffected by the lifetime of the HMNS. The neutrino-driven winds between 30 and 70 ms tend to be diminished by the accretion flow onto the HMNS, which cools more effectively than the neutrino irradiation heats it, making ejecta in this time from lower density, lower temperature edges of the flow where neutrino heating dominates. While total outflows remain the same, the proportion of blue outflows when compared at the latest common time ($t = 0.5\,s$) is 5% higher for the longer lived HMNS models, and they tend to be concentrated in magnetically and neutrino driven winds with velocities $v \sim 0.3 - 0.5c$.

7.2.3 Tracer Particles and Nucleosynthesis

The r-process abundance patterns at $t = 30$ yr for all of our simulations are shown in Figure 7.7. All models broadly follow the solar r-process abundance pattern. Both increasing the HMNS lifetime and initializing with a toroidal field

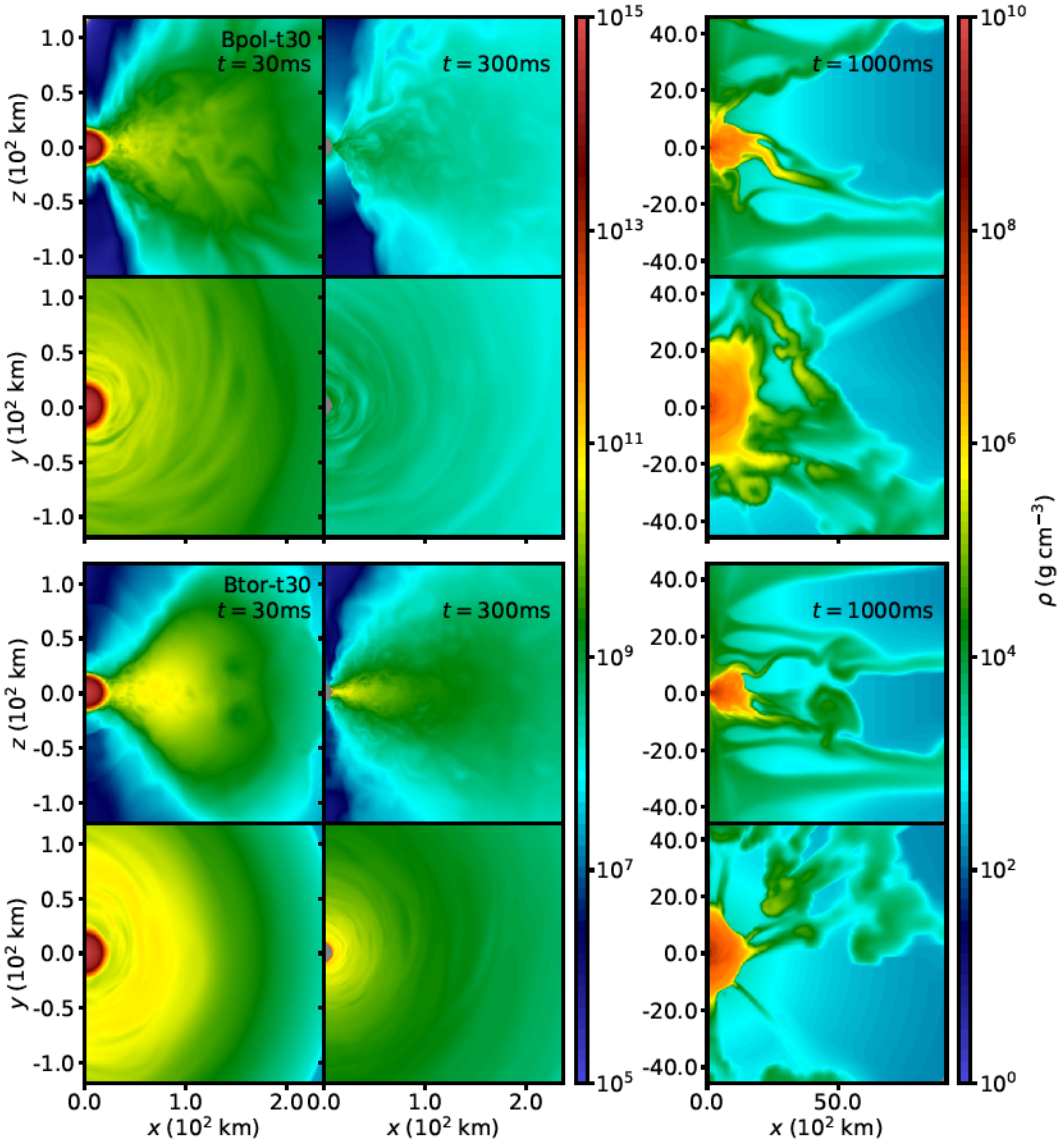

Figure 7.5: Slices of density in the $x - z$ ($\phi = 0$, polar) and $x - y$ ($\theta = 0$, equatorial) plane for the models *Bpol-t30* (top two rows) and *Btor-t30* (bottom two rows) at $t = 30$ ms (just before collapse), 300 ms and 1 s. The 2 leftmost columns show the difference in torus structure and density just before and a few hundred ms after collapse, corresponding to when most of the outflows occur. Gray regions show the excised black hole, and are outside the computational domain. Note the changes in both colour and length scale for the final column, showing the late time periodic mass ejection events from the torus.

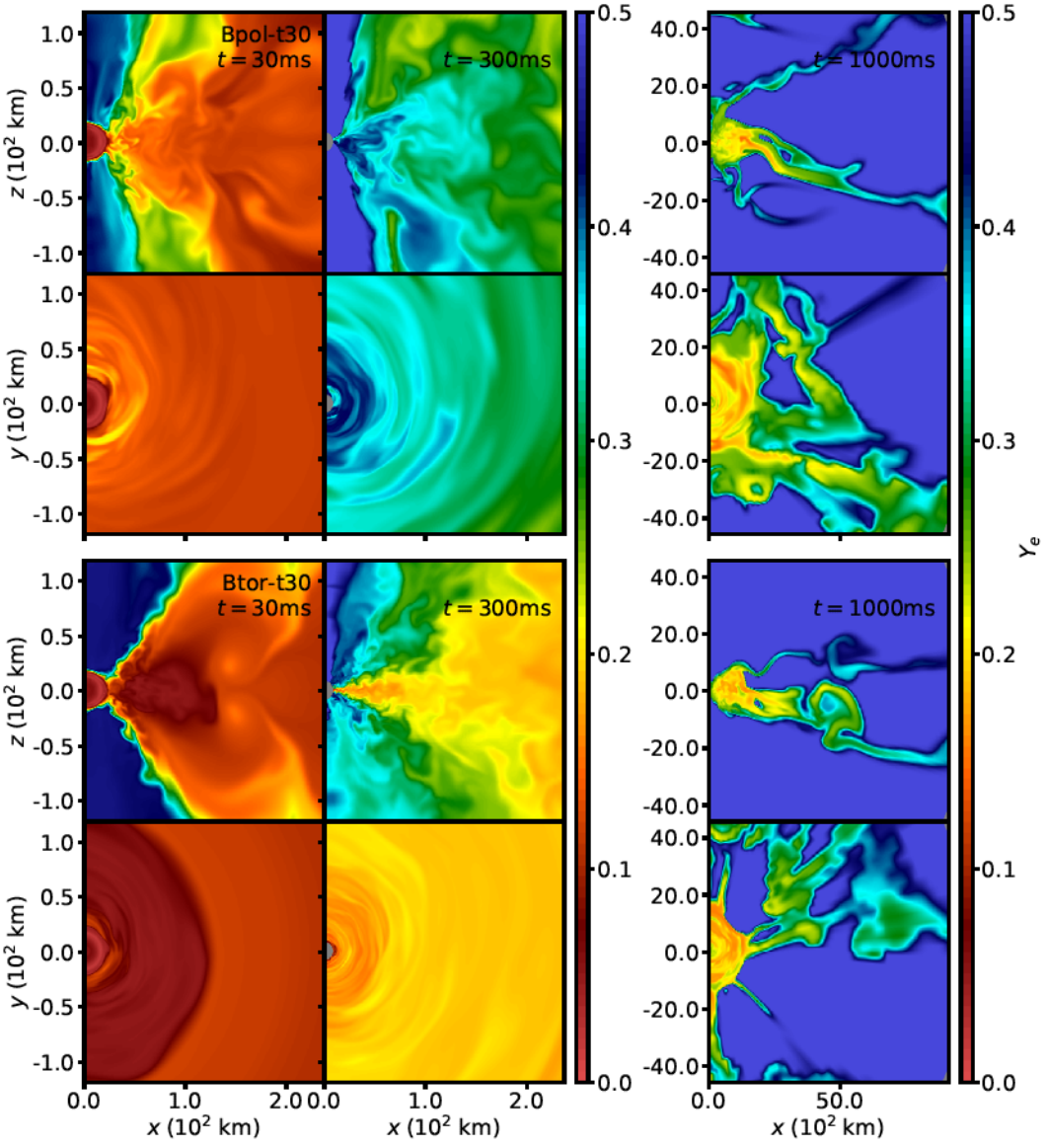

Figure 7.6: Same as Figure 7.5, but for electron fraction.

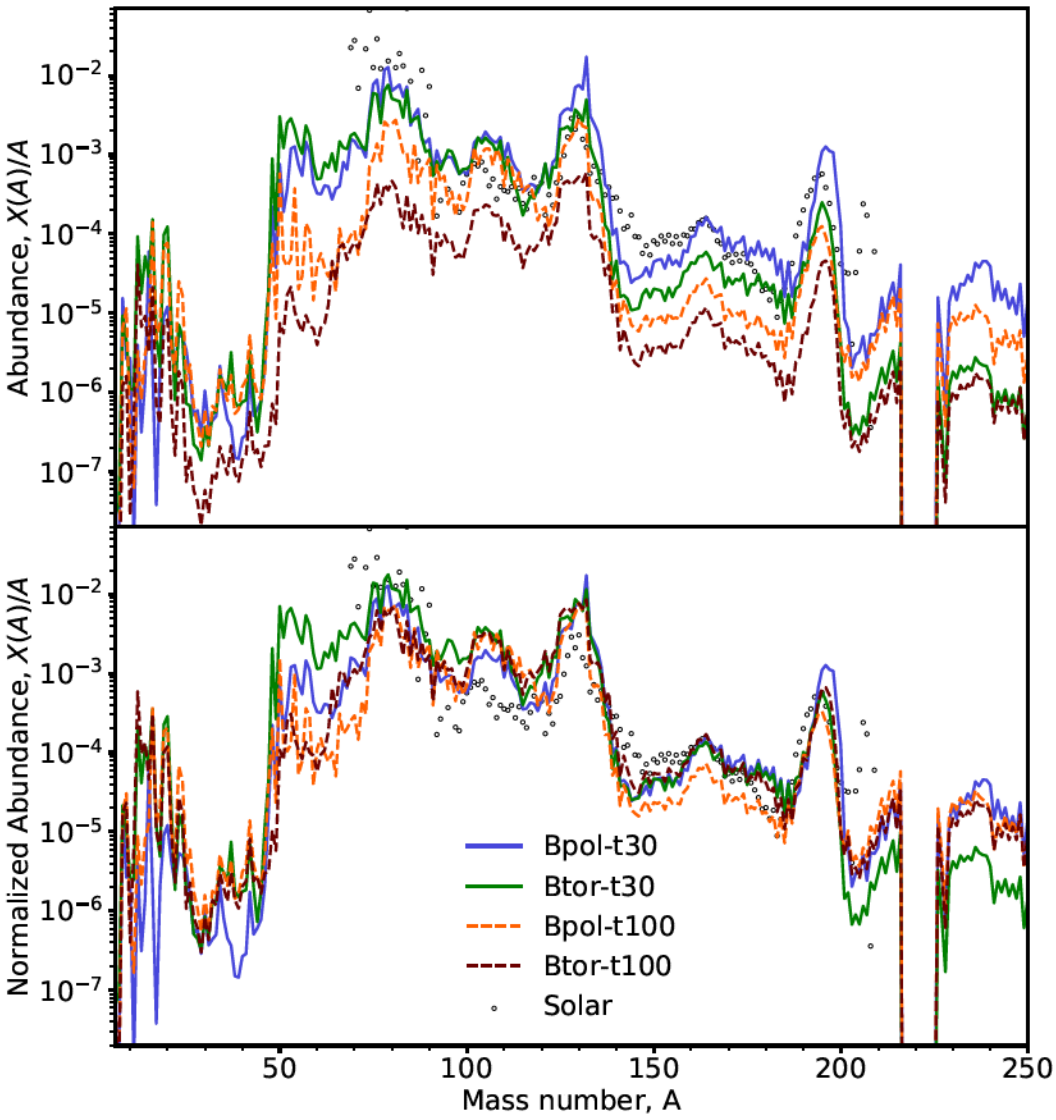

Figure 7.7: *Top:* Abundances at 30 years computed with the nucleosynthesis code `SkyNet` using the trajectories of all unbound tracer particles past 1000 km in the simulation. Shown in open circles are the solar r-process abundances from Goriely (1999), scaled such that the abundance at the second peak (A=130) matches that of our *Bpol-t30* model. *Bottom:* Same as top, except that *all* models are scaled such that they match the abundances of *Bpol-t30* at A=130, to illustrate differences in abundance pattern assuming that the ejected mass is the same.

geometry result in less mass ejection on timescales shorter than those required for weak interactions to raise the electron fraction above the critical value of $Y_e \gtrsim 0.25$. As a result of this, we see a drop in abundances with $A > 130$ in these models compared to the *Bpol-t30* model, qualitatively consistent with other studies.

The lifetime of the HMNS has the largest impact on the abundance distribution, with a decrease of almost 100 times from model *Bpol-t30* to *Bpol-t100* in these elements. However, the significant decrease in initially purely magnetic driven outflows (e.g., between *Bpol-t30* and *Btor-t30*) also causes a drop by almost half an order of magnitude. This is consistent with the expectations from the distribution of our particles in $s_{\rm kB} - Y_e - v$ space.

Overall, we find that all 4 models produce the 3 process peaks. By normalizing *all* the abundance patterns to the second peak of *Bpol-t30*, we find that the relative ratios of light to heavy r-process elements are very similar between models. The *Bpol-t100* model tends to underproduce the rare-earth peak, which could be due to the increased high entropy ($s \gtrsim 100 k_{\rm B}$/baryon) neutrino-driven winds during $30\,{\rm ms} \leq t \leq 100\,{\rm ms}$ that makes lighter seed nuclei for the r-process to build on (Lippuner and Roberts, 2015). We speculate that if more thermally driven outflows with lower entropy and $Y_e \sim 0.3$ were captured by running the simulation longer, this discrepancy may vanish as the fraction of ejecta from neutrino driven winds decreases. We also see a relative underproduction of actinides and overproduction of lighter ($A \lesssim 100$) r-process elements in *Btor-t30*. This is consistent with the additional high Y_e material ejected during HMNS collapse, which makes a substantial contribution to the total ejected mass.

Table 7.2: Mass ejection from all models. Columns show, from left to right, the model name, maximum simulation time, total unbound mass ejected at $r_{\rm out} = 1000\,{\rm km}$ using the Bernoulli criterion, mass ejected that is composed of HMNS material, $\dot{M}_{\rm out}$-weighted average electron fraction and radial velocity, as well as unbound ejected mass, average electron fraction, and radial velocity broken down by electron fraction (superscript blue lanthanide-poor: $Y_e \geq 0.25$, red lanthanide-rich: $Y_e < 0.25$).

Model	$t_{\rm max}$ (s)	$M_{\rm out}$ ($10^{-2}M_\odot$)	$M_{\rm out}^{\rm hmns}$ ($10^{-2}M_\odot$)	$\langle Y_e \rangle$	$\langle v_r \rangle$ (c)	$M_{\rm out}^{\rm blue}$ ($10^{-2}M_\odot$)	$\langle Y_e^{\rm blue} \rangle$	$\langle v_r^{\rm blue} \rangle$ (c)	$M_{\rm out}^{\rm red}$ ($10^{-2}M_\odot$)	$\langle Y_e^{\rm red} \rangle$	$\langle v_r^{\rm red} \rangle$ (c)
Bpol-t30	1.31	6.309	0.012	0.235	0.057	2.073	0.295	0.125	4.236	0.206	0.024
Btor-t30	2.00	5.992	0.026	0.226	0.035	1.494	0.305	0.091	4.498	0.200	0.017
Bpol-t100	0.75	4.790	0.012	0.223	0.059	1.619	0.294	0.120	3.171	0.186	0.029
Btor-t100	0.70	1.886	0.021	0.213	0.050	0.510	0.317	0.109	1.376	0.175	0.028

7.3 Comparison to previous work

7.3.1 3D Simulations

Kiuchi et al. (2022) carry out simulations in full GRMHD of a magnetized NS-NS merger, including neutrino leakage and absorption, and using the SFHO EOS. They run the simulation until $\sim 1.1\,{\rm s}$ post merger, with the HMNS surviving for 17 ms, and report mostly red post-merger outflows with broad range of electron fractions peaking at $Y_e \sim 0.24$ and traveling at $v \lesssim 0.15c$. The material with $Y_e \gtrsim 0.25$ is ejected via turbulent angular momentum transport from MRI operating in the disk after HMNS collapse, which travels too slow to power the blue kilonova from GW170817, consistent with other MHD simulations of BH-torus ejecta (Hayashi et al., 2022; Fahlman and Fernández, 2022; Curtis et al., 2023b). They note a lack of magnetic "tower" structure which drives outflows in the polar regions. Our *Btor-t30* model most closely matches the post-merger state found in their work, and our outflows show broad agreement in the electron fraction and entropies of the ejecta, as well as a lack of "tower" outflows. We do not however find a sharp cutoff in post-merger mass ejection with velocities $v > 0.15c$, but rather a gradual fall off. This could

be due to the increased lifetime of our HMNS, as well as the lack of special relativistic effects limiting the velocity of our outflows.

The simulations of Combi and Siegel (2023) are also of a GRMHD neutron star binary with neutrino leakage and absorption, using the APR EOS. Their HMNS survives $\sim 60\,\mathrm{ms}$ (the duration of the simulation), and ejects $\sim 10^{-2}\,M_\odot$ of ejecta, travelling with $v \gtrsim 0.1c$ mainly through disk winds. Through irradiation from the HMNS, the vast majority of this ejecta has $\langle Y_e \rangle \sim 0.3$. In our poloidal setups we also find sustained mass ejection rates of $\sim 0.1\,M_\odot\,s^{-1}$. They find about 5% of their outflows are generated from HMNS magnetized "tower" outflows, consistent with our simulations where we find only $\sim 10^{-4}\,M_\odot$ ($\sim 1\%$) come from magnetized outflows from the HMNS. They also find similar amounts of matter, $\sim 10^{-3}\,M_\odot$, moving with $v > 0.25c$ and $Y_e > 0.25$, which is consistent with our simulations.

Interestingly, they find that this result is consistent with the early blue kilonova of GW170817 through a simple kilonova model (Combi and Siegel, 2023). This is consistent with the recent kilonova models of Bulla (2023) and Ristic et al. (2023), which show that massive ($\sim 10^{-2}\,M_\odot$), blue ($Y_e > 0.25$), disk winds with $v \sim 0.05c$ are sufficient to power the early blue kilonova at times $\lesssim$5 days. This suggests that our very similar outflows would also be able to power the blue kilonova, although this cannot be confirmed without self-consistent modelling.

de Haas et al. (2022) examine the effects of magnetic field strength and geometry within the HMNS on the outflows mapped from a post-merger system, using 3D GRMHD neutrino-leakage/absorption simulations with the LS220 EOS. They find that a magnetar strength poloidal magnetic field in the HMNS ($B \sim 10^{15}\,\mathrm{G}$) is capable of ejecting $\sim 10^{-3}\,M_\odot$ of ejecta travelling with a wide

range of velocities, $0.05c < v < 0.6c$, and $Y_e \gtrsim 0.25$. They find decreasing the field strength by an order of magnitude decreases the ejecta to $\sim 10^{-4}\,M_\odot$, while also lowering the maximum velocity of the ejecta to $\sim 0.2c$. As well, they show changes in the imposed field geometry have similar effects. We find similar distributions of ejecta in velocity and electron fraction in our simulations, with mass ejection rates similar in our poloidal runs, despite in our simulations imposing a weaker (10^{14} G) initially toroidal field within the HMNS, but this changes quickly ($\lesssim 20$ ms) through the dynamics inside the HMNS. The field acquires a large poloidal component that peaks at values of 3×10^{16} G, and in the case of the 100 ms HMNS saturates at 8×10^{16} G. Additionally, they find changing magnetic field geometry to be primed for more stress driven outflow results in less $A > 130$ element nucleosynthesis, consistent with our findings.

Curtis et al. (2023a) and Mösta et al. (2020) perform 3D GRMHD simulations using a two moment (M1) and neutrino leakage scheme, respectively, the LS220 EOS, and the same HMNS remnant that survives for 12 ms after mapping in from a hydrodynamic merger simulation at 17 ms post-merger with an added $B \sim 10^{15}$ G poloidal field. Both studies find $\sim 3 \times 10^{-3}\,M_\odot$ worth of material ejected and velocities peaking at $0.15c$, with a significant tail up to $0.5c$. They highlight the difference in using an M1 vs leakage scheme for handling neutrinos, as the more advanced M1 scheme shifts the peak electron fraction of the ejecta up from distribution around $Y_e \sim 0.25$ to one peaking at $Y_e \sim 0.35 - 0.45$. Our results are similar in both velocity and electron fraction to the outflows from their system, especially to the leakage results of Mösta et al. (2020), with a mass ejection rate very similar to that of our *Bpol-t30* and *Bpol-t100* models.

7.3.2 2D Simulations

Studies that use axissymmetric simulations find that neutrino driven winds from the HMNS can reach velocities of $v \sim 0.15c$, although the exact velocity, ejecta mass, and composition depends on the lifetime of the HMNS, prescription used for neutrino radiation, as well as the handling of angular momentum transport. Higher velocities are possible, but they come with increased irradiation of the ejecta, making a simultaneous match to the blue and red KN difficult (e.g.,Fahlman and Fernández 2018; Lippuner et al. 2017; Nedora et al. 2021; Fujibayashi et al. 2023).

However, the recent hydrodynamic simulations of Just et al. (2023), mapped in from a merger simulation, include a more advanced energy-dependent neutrino leakage scheme and utilize the SFHo EOS, as well as varying remnant survival times in pseudo Newtonian potential. They find neutrino driven winds with a mass of $\sim 10^{-2}\,M_\odot$ and velocity $\langle v_{\rm ej} \rangle \sim 0.2c$ for their remnants which survive for a comparable amount of time, $\sim 100\,$ms. The mass ejection rates are broadly similar to our simulations $\sim 10^{-2} - 10^{-1}\,M_\odot\,{\rm s}^{-1}$, and due to the ejection mechanism, these tend to be high electron fraction $Y_e > 0.25$. They produce few elements with $A > 130$, most consistent with our *Btor-t100* run, which in our case produces the most dominant neutrino driven wind.

As well, Shibata et al. (2021a) perform unique 2D resistive GRMHD simulations, with a mean field prescription to prevent the damping of the magnetic dynamo in axisymmetry. Their simulations start from prescribing a toroidal magnetic field onto the outcome of a GRHD merger simulation using the DD2 EOS, similar to our idealized initial conditions. The setup of their low resistivity simulations are most comparable to our ideal MHD treatment, although their remnant has a different rotational profile, and survives for the duration of

the simulation. They find ejecta masses of $\sim 0.1\,M_\odot$ that plateau at $\sim 500\,\mathrm{ms}$, with average velocities of $0.5c$. The velocity and electron fraction of the ejecta is comparable to our `Btor-t30` run, although we find more low electron fraction ejecta and less mass ejected, by an order of magnitude.

7.3.3 Discussion

In general, our results are in agreement with those of the literature. They tend to span a broader range of electron fraction than is found by other studies in the literature, in particular with a larger component of material ejected with $Y_e < 0.2$. We speculate this is due to the simplicity of our leakage scheme in comparison to the more advanced energy dependent leakage, M1, or MCMC schemes (See Chapter 6) in combination with the idealized initial conditions for the torus, which tends to eject material in fast, magnetic stress driven outflows that can escape neutrino interactions.

Our HMNS itself has a lower mass ejection rate than others found in the literature. This is also likely partially due to the neutrino scheme, which yields less efficient heating of matter surrounding the HMNS, with implications for the neutrino driven winds. Additionally, the importance of the magnetic field configuration and resolution within and around the HMNS likely plays a large role. Our toroidal field embedded in the HMNS ejects mass similar to that of Kiuchi et al. (2022), but ejects an order of magnitude less mass than poloidal field configurations (e.g., Combi and Siegel 2023; de Haas et al. 2022; Curtis et al. 2023a). We do not resolve the most unstable wavelength of the MRI inside our HMNS, meaning that MRI driven ejection is not captured. Finally, we note that changing the rotation profile of the HMNS to match those of merger simulations could result in additional mechanical-oscillation powered

outflows as angular momentum is transported in the HMNS.

7.4 Conclusions

We have performed $\sim 1\,\mathrm{s}$ long 3D MHD simulations of a an idealized post-merger system consisting of a $2.65 M_\odot$ HMNS and $0.1\,M_\odot$ torus. We utilize Newtonian self-gravity, the hot APR EOS, a leakage/absorption scheme to handle neutrino interactions, and a pseudo-Newtonian potential after BH formation. Motivated by the sensitivity of the HMNS collapse time to physical processes, and necessitated by our use of Newtonian gravity, we use two parameterized HMNS collapse times of 30 ms and 100 ms to determine the effects of a HMNS as a central remnant. To evaluate the effects of the initial magnetic field geometry we utilize either a toroidal or poloidal magnetic field threaded through the torus.

The outflows are similar to those produced by idealized BH-disk setups, with a broad distribution of electron fraction and velocities. The HMNS itself tends to drive additional fast ($v \gtrsim 0.2c$) high electron fraction outflow ($Y_e > 0.3$) from the torus while it survives, due to oscillations in the remnant and energy from neutrino irradiation. Upon collapse, accretion onto the BH drives additional outflows, and slower ($v < 0.1c$), redder ($Y_e \sim 0.2$) MRI driven outflows begin to dominate the total mass ejection.

We find that in all cases, a shock wave is launched upon collapse of the HMNS as the torus and newly formed BH settle into an accreting state. The creation of a rarefaction wave has been seen in previous 2D hydrodynamic simulations (Fahlman and Fernández, 2018), but in the magnetized 3D case we find it drives significant outflows, especially noticeable in the short-lived HMNS. The launching of a magnetized shock by supramassive NS collapse has

been explored in baryon-free environments in the context of powering fast radio bursts (the "blitzar" mechanism, Most et al. 2018), but it is unknown whether this shock would drive mass outflows in a baryon polluted system. Whether this effect is due to our instantaneous collapse in Newtonian gravity, idealized initial conditions, or is a real effect, remains to be seen.

Neutrino driven winds from a longer lived ($t > 30\,\mathrm{ms}$) HMNS tend to be suppressed by the accretion of matter onto the HMNS, which cools efficiently. Due to accretion from the torus and oscillations of the HMNS, we find a lack of high velocity "tower" ejecta from the polar regions, which tend to be too dense to eject large amounts of matter moving at relativistic velocities.

Nucleosynthesis in the outflows tends to predict a robust r-process up to the second peak ($A \sim 130$), with order of magnitude variations past $A \sim 130$ caused by changing HMNS lifetime or magnetic field geometries.

Across all models, we find $M \sim 10^{-3} M_\odot$ of ejecta with $Y_e > 0.25$ and $v > 0.25c$. Whether or not this can completely account for the blue kilonova of GW170817 is model-dependent, as simple 2-component models require an order of magnitude more blue, fast ejecta. However, multidimensional models with more realistic opacities, thermalization, heating rates and viewing angle dependence find that a massive ($10^{-2}\,M_\odot$), slower ($v \sim 0.1c$) wind is all that is required. If the latter is the case, then our outflows are in principle capable of powering the blue kilonova.

The main limitations of our simulations are the use of an approximate neutrino scheme and Newtonian gravity. In testing of our neutrino scheme (see Chapter 6), we find results similar to that of other leakage comparisons, with an under prediction of neutrino heating resulting in slower, lower Y_e outflows as compared to more robust Monte Carlo or M1 schemes (e.g., Ardevol-Pulpillo

et al. 2019; Radice et al. 2022; Curtis et al. 2023a). For a similar mass HMNS in GR, we estimate that the HMNS could be up to 1.5 times as compact as our Newtonian HMNS upon merger. This reduces the amount of neutrino emission in the Newtonian HMNS compared to a general relativistic one, and results in the same under predictions of neutrino absorption in the torus, an effect which has been documented in the context of core collapse supernova simulations (e.g. Liebendörfer et al. 2001; Marek et al. 2006; Müller et al. 2012; O'Connor and Couch 2018; Mezzacappa 2023). As well, although we find a lower density magnetized funnel in our simulations, it is unlikely that we are able to correctly model jet formation in our simulations. Inclusion of special relativistic effects to the MHD equations results in corrections that are of order $\sim v/c$, so we estimate uncertainties in the fast tail of our ejecta of $\sim 50\%$, but the majority of outflows sit at v ¡ 0.1c, which results in a 10% inherent uncertainty.

Chapter 8

Magnetorotational Supernovae

8.1 Modified Newtonian Self-Gravity

Given that gravity is the dominant source of energy in CCSNe, it is important that a proper treatment of gravity, including general relativistic effects, is included. Multiple groups have shown that the use of GR results in more compact proto-NSs (Burrows and Vartanyan, 2021), which in turn leads to higher neutrino luminosities and energies. This then results in more successful explosions as the neutrino absorption in the gain region increases and becomes more efficient due to these effects. However, full treatment of GR is expensive, especially in addition to 3D MHD, prompting some groups to use a pseudo-Newtonian potential (Obergaulinger and Aloy 2020; O'Connor and Couch 2018, see also Just et al. 2023 for pseudo-GR potentials in NS merger outflows).

We follow this approach and implement the self-gravity solver of Rampp and Janka (2002) and Marek et al. (2006). The theory behind this method is in using the 1D Tolman-Oppenheimer-Volkoff (TOV) equations to determine contributions to the effective gravitational potential from pressure and other energy sources within the star, mimicking the effects of gravity felt in GR. The

solver is built on the truncated multipole algorithm of Müller and Steinmetz (1995) as extended to a non-uniform grid by Fernández et al. (2017). The multipole algorithm is a computationally efficient way to solve the integral form of the Poisson equation for the gravitational potential,

$$\Phi_{sg} = -G \int \mathrm{d}^3 r \frac{\rho(r')}{|r - r'|}, \tag{8.1}$$

by casting the denominator into an expansion of spherical harmonics. In azimuthal symmetry, The self-gravitational potential, Φ_{sg} takes the form

$$\Phi_{sg}(r, \theta) = -2\pi G \sum_{\ell=0}^{\ell_{\max}} P_\ell(\cos\theta) \left[\frac{1}{r^{\ell+1}} C_\ell(r, \theta) + r^\ell D_\ell(r, \theta) \right], \tag{8.2}$$

where P_ℓ is the Legendre polynomial of index ℓ, and the moments C_ℓ and D_ℓ are given by

$$C_\ell(r, \theta) = \int_0^\pi \sin\theta \mathrm{d}\theta P_\ell(\cos\theta) \int_0^r \mathrm{d}r' r'^{2+\ell} \rho(r', \theta) \tag{8.3}$$

$$D_\ell(r, \theta) = \int_0^\pi \sin\theta \mathrm{d}\theta P_\ell(\cos\theta) \int_r^\infty \mathrm{d}r' r'^{1-\ell} \rho(r', \theta). \tag{8.4}$$

In the limit of $\ell_{\max} \to \infty$, this is an exact solution of Poisson's equation. For computation, these integrations are discretized to be evaluated as sums at the cell edges, up to a maximum of $\ell_{\max}$ which sets the desired accuracy. To avoid the integral diverging at $r = 0$, we set a lower limit on the values of r that can be used in the integration. In our case, we find that setting a softening length of $r_{\min} = \frac{1}{10}\Delta r_{\min}$ has a negligible effect on the dynamics of the simulation, but prevents infinities from occurring in the calculation of the gravitational potential.

To implement our pseudo-GR potential, we subtract off the spherically sym-

metric $\ell = 0$ moment from Φ_{sg} and add on a term $\Phi_{\rm TOV}$,

$$\Phi_{\rm GR} = \Phi_{\rm SG} - \Phi_{\rm SG}(\ell = 0) + \Phi_{\rm TOV} \tag{8.5}$$

$$\Phi_{\rm TOV}(r) = -G \int_r^\infty \frac{1}{r'^2}\left(m_{\rm TOV} + \frac{4\pi r'^3(P + P_\nu)}{c^2}\right)\left(\frac{1}{\Gamma^2}\frac{\rho c^2 + e + P}{\rho c^2}\right)\mathrm{d}r' \tag{8.6}$$

where the TOV mass and metric function are defined as

$$m_{\rm TOV}(r) = \frac{1}{\Gamma}\int_0^r \mathrm{d}r' 4\pi r'^2\left(\rho c^2 + e + \frac{E_\nu}{c^2} + \frac{vF_\nu}{c^4\Gamma}\right) \tag{8.7}$$

$$\Gamma(r) = \sqrt{1 + \left(\frac{v}{c}\right)^2 - \frac{2Gm_{\rm TOV}}{rc^2}}. \tag{8.8}$$

The terms F_ν, P_ν, E_ν are the neutrino flux, pressure and energy, as determined by the neutrino scheme. For our leakage scheme, we calculate the enclosed neutrino energies and luminosity (Chapter 4), and from there we assume isotropy to find $F_\nu = L_\nu/4\pi r^2$ and $P_\nu = E_\nu/3$. Equations 8.7 and 8.8 are recursively defined, but we find that they converge quickly (within a few timesteps), if we initially set $\Gamma(r) = 1$ everywhere then calculate $m_{\rm TOV}$, and iterate.

8.2 Verification Tests

8.2.1 Static Comparison

To test our new gravitational potential, we first determine the effective gravitational potential from a spherically symmetric $1.44M_\odot$, 11.4 km radius non-spinning cold neutron star in hydrostatic equilibrium (HSE). We use the `drns` code (Stergioulas and Friedman, 1995) to solve the TOV equations in 2D, and output the necessary thermodynamic quantities to construct the exact same stellar profile in `FLASH4.5`. We also output the metric potentials, γ, ρ, α, and

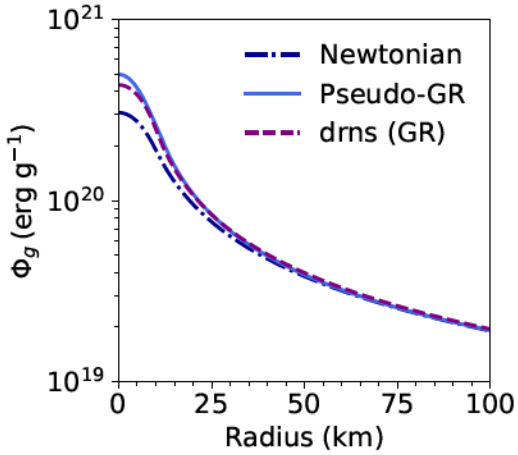

Figure 8.1: Comparison of gravitational potentials generated by a $1.44 M_{\odot}$, 11.4 km radius non-spinning cold NS in HSE. The same profiles are initialized in `FLASH`, using both the Newtonian and pseudo-GR potential (eq 8.5).

ω as defined by the Schwarzchild line element (see Cook et al. (1994) for full definitions), and define a relativistic generalization of the Newtonian gravitational potential

$$ds^2 = -e^{\gamma+\rho}dt^2 + e^{2\alpha}(dr^2 + r^2 d\theta^2) + e^{\gamma-\rho} r^2 \sin^2\theta (d\phi - \omega dt^2) \tag{8.9}$$

$$\phi_{GR} = 1/2(\gamma + \rho)c^2 \tag{8.10}$$

which converges to the Newtonian limit $\sim GM/r$ far away from the star. We find that the implementation of the pseudo-GR potential results in stronger gravitational effects outside of the star as compared to the purely Newtonian case, and is in good agreement with the metric potentials from the fully relativistic `drns` for $r \gtrsim R_{NS}$.

8.2.2 Collapse Comparison

Concern about utilizing Newtonian potentials comes from the change in neutrino emission due to the less compact stellar core. To measure the strength

of these effects, we run a comparison core collapse supernova with our potential up until a few 100 ms post bounce, and compare to the fully relativistic hydrodynamics code GR1D (O'Connor and Ott, 2010).

For our initial progenitor, we use the well studied 35 solar mass magnetized rotating star (35OC) of Heger et al. (2005), evolved using the 1D stellar evolution code Kepler (Weaver et al., 1978; Woosley et al., 2002). This is the star which will be used in future production runs, and an ideal way to test how our collapse compares to full GR simulations. However, since GR1D is a 1D hydrodynamic code, we set the initial rotation and magnetization of the star to 0 in both GR1D and FLASH4.5. We then run both codes with identical equations of state, using an axisymmetric initial condition, but evolving FLASH4.5 in 2D. We use an almost identical neutrino leakage/absorption scheme to the one detailed in GR1D (O'Connor and Ott, 2010), which has been used widely in the literature. This scheme differs from the scheme described in Chapter 6 in that the separate absorption scheme outside of the neutrinosphere which treats the HMNS as a lightbulb source term is removed. Instead, all neutrino luminosity is treated as enclosed luminosities within spherical shells determined by the radial coordinate on the grid. The heating rate is then obtained using an empirical formula that approximates absorption effects of more detailed neutrino schemes. In the case of magnetorotational supernovae, the explosion is dominated by magnetic energy, and while neutrinos play an important role and cannot be neglected, an approximate treatment is acceptable. Electron capture onto nuclei is handled using the precription of (Liebendörfer, 2005), as implemented into FLASH4.5 by (Couch, 2013).

The initial collapse until bounce is dominated by gravitational forces, making the timing of core bounce, as defined when the central density and en-

tropy ($r < 30\,\mathrm{km}$) reach threshold values of $2 \times 10^{14}\mathrm{g\ cm^{-3}}$ and $3\,k_\mathrm{b}$ baryon^{-1} (O'Connor and Ott, 2010), a good test of the gravitational acceleration.

Core bounce occurs 18 ms sooner in the pseudo-GR potential of `FLASH4.5` than in `GR1D`, consistent with other tests of the pseudo-GR potential (O'Connor and Couch, 2018). In comparison, the purely Newtonian potential run of `FLASH4.5` experiences core bounce 30 ms later than the full GR run. We find better agreement in electron fraction and density from the pseudo-GR run to the GR run, whereas the entropy in GR tends to be lower. The condition for bounce in full GR is triggered by a spike in the entropy at $\sim 15\,\mathrm{km}$ instead of a smoothly varying central value above $3\,k_\mathrm{b}$ baryon^{-1} as found in both the Newtonian and pseudo-GR runs. We note a similar spike in entropy in the pseudo-GR potential, but this occurs outside of the defined "central" value of 30 km, and as such does not trigger the bounce condition.

We compare the neutrino emission between the two codes $\sim 20\,\mathrm{ms}$ after bounce, when neutrino emission is peaking at values of $\sim 2 \times 10^{53}\,\mathrm{erg\,s^{-1}}$ across all species. We take the comparison when the shock in the star is approximately the same radius (60 km) so that the neutrino emission properties are spatially aligned. We find agreement to within a factor of ~ 2 for both lepton number and energy change within the fluid at this time, although the spatial peak in neutrino emission occurs $\sim 5\,\mathrm{km}$ further out in the pseudo-GR case, a result of a higher compactness PNS in full GR.

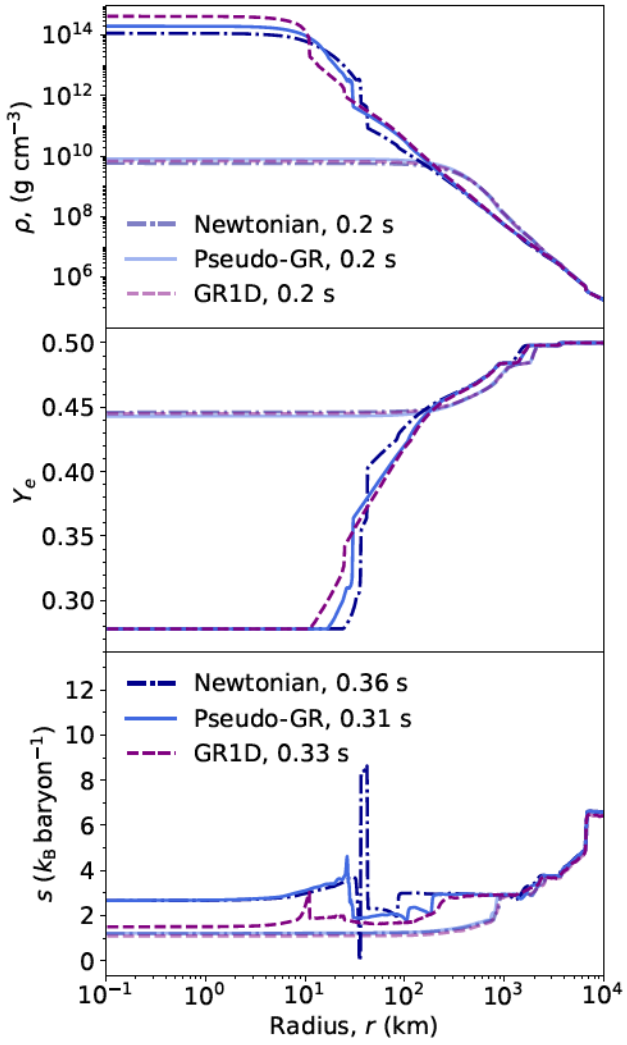

Figure 8.2: Thermodynamic quantities during the hydrodynamic core collapse of a 35 $M_\odot$ star, run using full GR in `GR1D`, and both a pseudo-GR and purely Newtonian potential in `FLASH4.5`. Semi-transparent lines denote a common time of $t = 0.2$ s, where the differences between the codes are small, where as opaque lines show the quantities at $t = t_{\rm bounce}$, which varies between the codes.

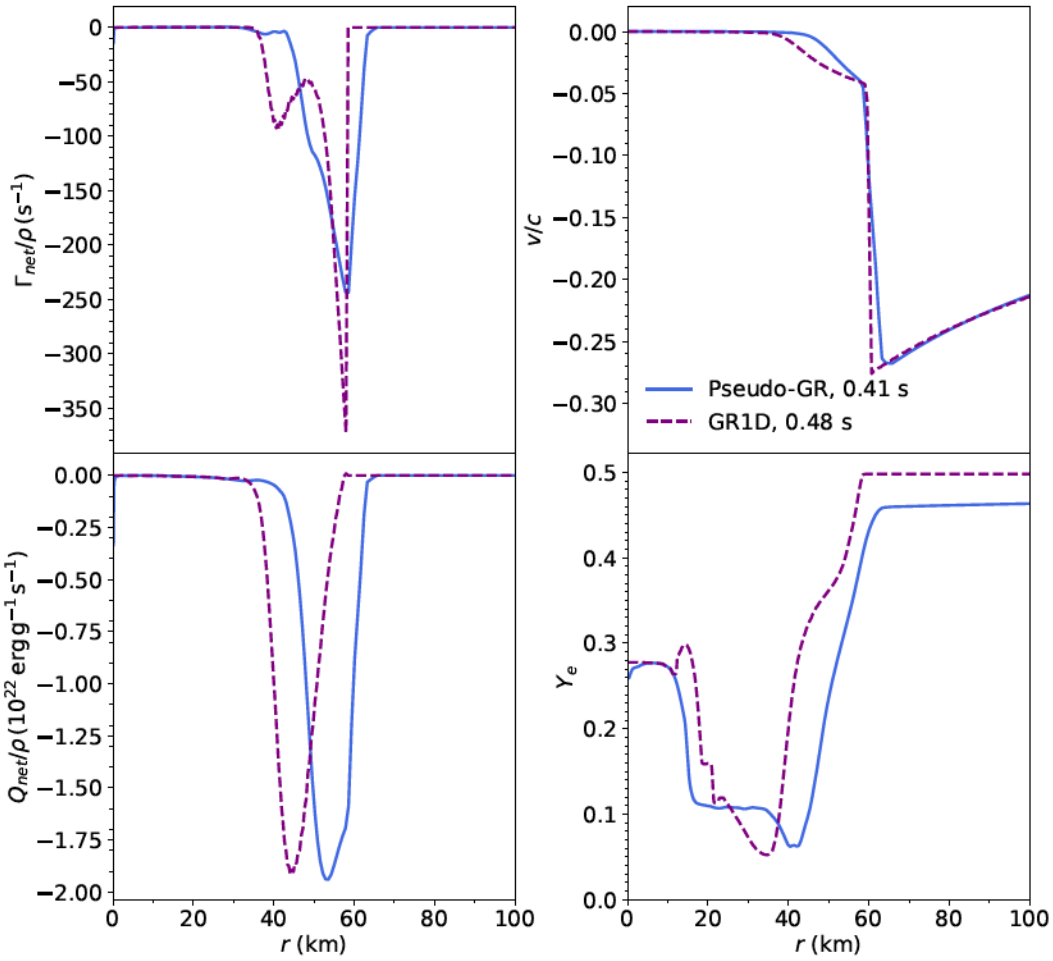

Figure 8.3: Quantities relevant to neutrino emission during the hydrodynamic core collapse of a 35 $M_\odot$ star, run using full GR in `GR1D`, and both a pseudo-GR and purely Newtonian potential in `FLASH4.5`. The codes are offset temporally such that the infalling material is spatially aligned by requiring matching shock positions. This allows us to compare relevant neutrino quantities.

Chapter 9

Conclusion

In this thesis, we examine different possible astrophysical sites for r-process element nucleosynthesis and the transients associated with them. In particular, the remnants of NS mergers and their associated ejecta are thought to contain matter with the necessary electron fractions, entropies, and expansion timescales for the r-process to occur (e.g., Kasen et al. 2015; Lippuner and Roberts 2015), while also comprising a sizable fraction of ejecta mass from the system (Wu et al., 2016; Radice et al., 2018; Margalit and Metzger, 2019; Krüger and Foucart, 2020; Fujibayashi et al., 2020c; Nedora et al., 2021). This makes understanding the post-merger mass ejection crucial for our understanding of kilonovae and the production of r-process elements in the universe. The ejecta from post-merger disks is dominated by magnetic effects, which drive early ($t \sim 0.1s$), fast outflows from magnetic streses, as well as late time ($t \sim s$) thermal outflows induced by the MRI. To resolve the wavelength of most unstable mode of the MRI within the torus, as well as track outflows to large radii, we require an MHD code with high spatial resolution and large distance scales ($\sim 10^3 - 10^8$ m). As well, the code must account for both neutrino emission and absorption in order to correctly characterize the electron fraction

and velocities of the ejecta, both of which have important implications for the kilonova and abundances of r-process elements created.

To this end, we extended the `FLASH4.5` code to run MHD in 3D non-uniform spherical coordinates. Necessary modifications involve the addition of geometric source terms as well as curvilinear volumes, face areas, and line elements. We perform tests of the MHD implementation to verify the code is working correctly, and validate our usage in evolving post-merger tori using a well studied initial condition. We then turn our attention to the implementation of neutrino physics. Due to the computational expense of our simulations, we opt to use a 3 species neutrino leakage/absorption scheme, which takes into account emission and absorption of electron-type neutrinos and antineutrinos from charged-current weak interactions (Bruenn, 1985), as well as emission of all relevant neutrino types from plasmon decay, nucleon-nucleon brehmsstrahlung, and pair processes (Ruffert et al., 1997). The scheme previously interpolated between analytic rates for free-streaming and optically thick regimes by utilizing the pressure scale height in the torus, which works well for BH-tori systems with low mass tori ($M \lesssim 0.03 M_\odot$) (Fernández and Metzger, 2013). We modify the scheme so that it no longer depends on the pressure scale height within the torus, and instead uses gradients in neutrino energy and number to determine the neutrino fluxes, as done in Ardevol-Pulpillo et al. (2019). We show that our new scheme no longer underpredicts the effects of neutrino emission within massive tori ($M \sim 0.1 M_\odot$) by comparing our new implementation to the time stationary MC neutrino transport code `SedonuGR`.

Armed with our new computationally inexpensive MHD code with simple neutrino transport, we perform long term ($\sim$3 s) simulations of accretion tori around BHs that could feasibly be the outcome of a NS-NS or NS-BH merger.

We ran three different 3D models, two with a 2.65 $M_\odot$ BH and 0.1 $M_\odot$ torus, but either a toroidal or poloidal field, and one more compact system with a 8 $M_\odot$ BH and 0.03 $M_\odot$ torus threaded with a poloidal field. The outflows from all these systems showed two different channels of ejecta, an early ($t \lesssim 100\,\mathrm{ms}$) MHD stress driven outflow that is dependent on the initial magnetic field geometry, and a late time ($t \gtrsim 400\,ms$) thermal outflow that is driven by MRI induced turbulence in the torus. The MHD stress driven outflow has velocities $v \gtrsim 0.25c$ and electron fractions $Y_e \lesssim 0.3$, while late time outflows have a velocity peaking at $v \sim 0.1c$ and a broad range of electron fractions, $0.05 < Y_e < 0.5$. While these outflows reach much higher velocities than those found in hydrodynamic simulations, there is still insufficient mass in high velocity, high electron fraction blue outflows to match the mass and velocity inferred from two component kilonova modelling of GW170817.

The BH-tori setups implicitly neglect ejecta from a remnant HMNS, but the HMNS phase has the potential to drive additional blue outflows through neutrino irradiation, mechanical oscillations, and MHD stress driven ejecta. GW170817 is believed to be below the maximum mass threshold for prompt collapse, meaning the inclusion of the HMNS phase may be a resolution to the lack of high velocity blue outflows found in BH simulations. To this end, we further modify `FLASH4.5` to include a HMNS within our domain. This involves the addition of a hot nuclear equation of state, Newtonian self-gravity, and an update to include self-consistent emission and absorption from a HMNS included entirely within the domain. We calculate the neutrino luminosity enclosed by radial shells within the domain, up until the neutrinosphere of the HMNS. Using this luminosity and the integrated radial optical depths for each poloidal and azimuthal cell, we then include the effects of neutrino absorption

from the HMNS. Time stationary comparisons with `SedonuGR` show agreement with neutrino heating and lepton number change to within an order of magnitude or better, especially within the torus.

We then run long term 3D MHD ($\sim 1\,\mathrm{s}$) simulations of HMNS-accretion disk systems to examine the effects of a HMNS on mass ejection. We again choose two representative magnetic field geometries, an ordered poloidal and purely toroidal field. Motivated by the sensitivity of the HMNS collapse time to various microphysics and constrained by our use of Newtonian gravity, we choose two different collapse times of 30 and 100 ms which we expect to have a significant effect on the outflows based on previous simulations. Our models show that purely MHD stress-driven winds and magnetized neutrino-driven winds can eject $M_{ej} \sim 10^{-2} M_\odot$ of material with velocities peaking at $v \sim 0.1c$ and a tail out to $v \lesssim 0.7c$. These have a broad range of electron fraction over the interval $0.1 \lesssim Y_e \lesssim 0.5$, reflecting whether or not the ejecta has a significant neutrino-driven component or is quickly launched by magnetic stresses. The transition to a thermally driven component happens at $t \gtrsim 400\,\mathrm{ms}$, with MRI driven turbulence continuing to eject material with lower velocities ($v \sim 0.05c$) and a broad range of electron fractions peaking at $Y_e \sim 0.2$. We still find an order of magnitude less mass ejected with $v > 0.25c$ and $Y_e > 0.25$ than is inferred from two component kilonova models, but detailed kilonova models show that the velocities of the required disk wind component may be overestimated. Therefore, detailed multi-dimensional kilonova modelling is required to conclusively say whether or not the ejecta from our simulations could power the blue kilonova.

Motivated by studies which show that a rare r-process site may be active earlier in the galaxy than NS mergers, we also explore the necessary modifications

to the code to run simulations of MRSNe. As gravity is the dominant source of energy in all CCSNe, this involves the addition of a pseudo-GR potential to the Newtonian self-gravity module, as well as changes to the neutrino leakage scheme to account for emission and absorption within the star. We show tests of our implementations, and leave the running of MRSN simulations to future work.

Bibliography

B. P. Abbott, R. Abbott, T. D. Abbott, F. Acernese, K. Ackley, C. Adams, T. Adams, P. Addesso, R. X. Adhikari, V. B. Adya, and et al. Gravitational Waves and Gamma-Rays from a Binary Neutron Star Merger: GW170817 and GRB 170817A. *ApJ*, 848:L13, October 2017. doi: 10.3847/2041-8213/aa920c.

Ricard Aguilera-Miret, Carlos Palenzuela, Federico Carrasco, and Daniele Viganò. The role of turbulence and winding in the development of large-scale, strong magnetic fields in long-lived remnants of binary neutron star mergers. *arXiv e-prints*, art. arXiv:2307.04837, July 2023. doi: 10.48550/arXiv.2307.04837.

A. Akmal, V. R. Pandharipande, and D. G. Ravenhall. Equation of state of nucleon matter and neutron star structure. *Phys. Rev. C*, 58(3):1804–1828, September 1998. doi: 10.1103/PhysRevC.58.1804.

R. Ardevol-Pulpillo, H. T. Janka, O. Just, and A. Bauswein. Improved leakage-equilibration-absorption scheme (ILEAS) for neutrino physics in compact object mergers. *MNRAS*, 485(4):4754–4789, June 2019. doi: 10.1093/mnras/stz613.

D. Argast, M. Samland, F. K. Thielemann, and Y. Z. Qian. Neutron star merg-

ers versus core-collapse supernovae as dominant r-process sites in the early Galaxy. *A&A*, 416:997–1011, March 2004. doi: 10.1051/0004-6361:20034265.

I. V. Artemova, G. Bjoernsson, and I. D. Novikov. Modified Newtonian Potentials for the Description of Relativistic Effects in Accretion Disks around Black Holes. *ApJ*, 461:565, April 1996. doi: 10.1086/177084.

Steven A. Balbus and John F. Hawley. A Powerful Local Shear Instability in Weakly Magnetized Disks. I. Linear Analysis. *ApJ*, 376:214, July 1991. doi: 10.1086/170270.

Steven A. Balbus and John F. Hawley. A Powerful Local Shear Instability in Weakly Magnetized Disks. IV. Nonaxisymmetric Perturbations. *ApJ*, 400: 610–621, December 1992. doi: 10.1086/172022.

James M. Bardeen and Jacobus A. Petterson. The Lense-Thirring Effect and Accretion Disks around Kerr Black Holes. *ApJ*, 195:L65, January 1975. doi: 10.1086/181711.

J. Barnes and D. Kasen. Effect of a High Opacity on the Light Curves of Radioactively Powered Transients from Compact Object Mergers. *ApJ*, 775: 18, September 2013. doi: 10.1088/0004-637X/775/1/18.

Thomas W. Baumgarte, Stuart L. Shapiro, and Masaru Shibata. On the Maximum Mass of Differentially Rotating Neutron Stars. *ApJ*, 528:L29–L32, Jan 2000. doi: 10.1086/312425.

R. D. Blandford and R. L. Znajek. Electromagnetic extraction of energy from Kerr black holes. *MNRAS*, 179:433–456, May 1977. doi: 10.1093/mnras/179.3.433.

S. W. Bruenn. Stellar core collapse - Numerical model and infall epoch. *ApJS*, 58:771–841, August 1985. doi: 10.1086/191056.

Mattia Bulla. The critical role of nuclear heating rates, thermalization efficiencies, and opacities for kilonova modelling and parameter inference. *MNRAS*, 520(2):2558–2570, April 2023. doi: 10.1093/mnras/stad232.

E. Margaret Burbidge, G. R. Burbidge, William A. Fowler, and F. Hoyle. Synthesis of the Elements in Stars. *Reviews of Modern Physics*, 29(4):547–650, Jan 1957. doi: 10.1103/RevModPhys.29.547.

A. Burrows and D. Vartanyan. Core-collapse supernova explosion theory. *Nature*, 589(7840):29–39, January 2021. doi: 10.1038/s41586-020-03059-w.

R. Chornock et al. The Electromagnetic Counterpart of the Binary Neutron Star Merger LIGO/Virgo GW170817. IV. Detection of Near-infrared Signatures of r-process Nucleosynthesis with Gemini-South. *ApJ*, 848:L19, October 2017. doi: 10.3847/2041-8213/aa905c.

I. M. Christie, A. Lalakos, A. Tchekhovskoy, R. Fernández, F. Foucart, E. Quataert, and D. Kasen. The role of magnetic field geometry in the evolution of neutron star merger accretion discs. *MNRAS*, 490(4):4811–4825, December 2019. doi: 10.1093/mnras/stz2552.

Riccardo Ciolfi and Jay Vijay Kalinani. Magnetically Driven Baryon Winds from Binary Neutron Star Merger Remnants and the Blue Kilonova of 2017 August. *ApJ*, 900(2):L35, September 2020. doi: 10.3847/2041-8213/abb240.

P. Colella. A Direct Eulerian MUSCL Scheme for Gas Dynamics. *SIAM Journal on Scientific and Statistical Computing*, 6(1):104–117, January 1985. doi: 10.1137/0906009.

Luciano Combi and Daniel M. Siegel. Grmhd simulations of neutron-star mergers with weak interactions: r-process nucleosynthesis and electromagnetic signatures of dynamical ejecta. *The Astrophysical Journal*, 944(1):28, feb 2023. doi: 10.3847/1538-4357/acac29. URL `https://dx.doi.org/10.3847/1538-4357/acac29`.

Luciano Combi and Daniel M. Siegel. Jets from neutron-star merger remnants and massive blue kilonovae. *arXiv e-prints*, art. arXiv:2303.12284, March 2023. doi: 10.48550/arXiv.2303.12284.

Gregory B. Cook, Stuart L. Shapiro, and Saul A. Teukolsky. Rapidly Rotating Neutron Stars in General Relativity: Realistic Equations of State. *ApJ*, 424: 823, April 1994. doi: 10.1086/173934.

B. Côté, C. L. Fryer, K. Belczynski, O. Korobkin, M. Chruślińska, N. Vassh, M. R. Mumpower, J. Lippuner, T. M. Sprouse, R. Surman, and R. Wollaeger. The Origin of r-process Elements in the Milky Way. *ApJ*, 855:99, March 2018. doi: 10.3847/1538-4357/aaad67.

Sean M. Couch. On the Impact of Three Dimensions in Simulations of Neutrino-driven Core-collapse Supernova Explosions. *ApJ*, 775(1):35, September 2013. doi: 10.1088/0004-637X/775/1/35.

Sean M. Couch and Christian D. Ott. Revival of the Stalled Core-collapse Supernova Shock Triggered by Precollapse Asphericity in the Progenitor Star. *ApJ*, 778(1):L7, November 2013. doi: 10.1088/2041-8205/778/1/L7.

John J. Cowan, Christopher Sneden, James E. Lawler, Ani Aprahamian, Michael Wiescher, Karlheinz Langanke, Gabriel Martínez-Pinedo, and Friedrich-Karl Thielemann. Origin of the heaviest elements: The rapid

neutron-capture process. *Reviews of Modern Physics*, 93(1):015002, January 2021. doi: 10.1103/RevModPhys.93.015002.

T. G. Cowling. The magnetic field of sunspots. *MNRAS*, 94:39–48, November 1933. doi: 10.1093/mnras/94.1.39.

P. S. Cowperthwaite et al. The Electromagnetic Counterpart of the Binary Neutron Star Merger LIGO/Virgo GW170817. II. UV, Optical, and Near-infrared Light Curves and Comparison to Kilonova Models. *ApJ*, 848:L17, October 2017. doi: 10.3847/2041-8213/aa8fc7.

Sanjana Curtis, Pablo Bosch, Philipp Mösta, David Radice, Sebastiano Bernuzzi, Albino Perego, Roland Haas, and Erik Schnetter. Outflows from Short-Lived Neutron-Star Merger Remnants Can Produce a Blue Kilonova. *arXiv e-prints*, art. arXiv:2305.07738, May 2023a. doi: 10.48550/arXiv.2305.07738.

Sanjana Curtis, Jonah M. Miller, Carla Fröhlich, Trevor Sprouse, Nicole Lloyd-Ronning, and Matthew Mumpower. Nucleosynthesis in Outflows from Black Hole-Neutron Star Merger Disks with Full GR(ν)RMHD. *ApJ*, 945(1):L13, March 2023b. doi: 10.3847/2041-8213/acba16.

Sebastiaan de Haas, Pablo Bosch, Philipp Mösta, Sanjana Curtis, and Nathanyel Schut. Magnetic field effects on nucleosynthesis and kilonovae from neutron star merger remnants. *arXiv e-prints*, art. arXiv:2208.05330, August 2022. doi: 10.48550/arXiv.2208.05330.

L. Dessart, C. D. Ott, A. Burrows, S. Rosswog, and E. Livne. Neutrino Signatures and the Neutrino-Driven Wind in Binary Neutron Star Mergers. *ApJ*, 690:1681–1705, January 2009. doi: 10.1088/0004-637X/690/2/1681.

M. R. Drout et al. Light curves of the neutron star merger GW170817/SSS17a: Implications for r-process nucleosynthesis. *Science*, 358:1570–1574, December 2017. doi: 10.1126/science.aaq0049.

Anshu Dubey, Katie Antypas, Murali K. Ganapathy, Lynn B. Reid, Katherine Riley, Dan Sheeler, Andrew Siegel, and Klaus Weide. Extensible component-based architecture for flash, a massively parallel, multiphysics simulation code. *Parallel Computing*, 35(10):512 – 522, 2009. ISSN 0167-8191. doi: https://doi.org/10.1016/j.parco.2009.08.001.

Matthew D. Duez, Yuk Tung Liu, Stuart L. Shapiro, Masaru Shibata, and Branson C. Stephens. Collapse of Magnetized Hypermassive Neutron Stars in General Relativity. *Phys. Rev. Lett.*, 96:031101, Jan 2006. doi: 10.1103/PhysRevLett.96.031101.

David Eichler, Mario Livio, Tsvi Piran, and David N. Schramm. Nucleosynthesis, neutrino bursts and γ-rays from coalescing neutron stars. *Nature*, 340 (6229):126–128, Jul 1989. doi: 10.1038/340126a0.

Charles R. Evans and John F. Hawley. Simulation of Magnetohydrodynamic Flows: A Constrained Transport Model. *ApJ*, 332:659, September 1988. doi: 10.1086/166684.

Steven Fahlman. Outflows, mergers, and tori, oh my! Master's thesis, University of Alberta, August 2019. doi: 10.7939/r3-6877-8m55.

Steven Fahlman and Rodrigo Fernández. Hypermassive Neutron Star Disk Outflows and Blue Kilonovae. *ApJ*, 869(1):L3, December 2018. doi: 10.3847/2041-8213/aaf1ab.

Steven Fahlman and Rodrigo Fernández. Long-term 3D-MHD simulations of black hole accretion disks formed in neutron star mergers. *MNRAS*, April 2022. doi: 10.1093/mnras/stac948.

Rodrigo Fernández. Three-dimensional simulations of SASI- and convection-dominated core-collapse supernovae. *MNRAS*, 452(2):2071–2086, September 2015. doi: 10.1093/mnras/stv1463.

Rodrigo Fernández and Brian D. Metzger. Delayed outflows from black hole accretion tori following neutron star binary coalescence. *MNRAS*, 435:502–517, October 2013. doi: 10.1093/mnras/stt1312.

Rodrigo Fernández and Brian D. Metzger. Electromagnetic Signatures of Neutron Star Mergers in the Advanced LIGO Era. *Annual Review of Nuclear and Particle Science*, 66(1):23–45, October 2016. doi: 10.1146/annurev-nucl-102115-044819.

Rodrigo Fernández, Daniel Kasen, Brian D. Metzger, and Eliot Quataert. Outflows from accretion discs formed in neutron star mergers: effect of black hole spin. *MNRAS*, 446:750–758, January 2015. doi: 10.1093/mnras/stu2112.

Rodrigo Fernández, Francois Foucart, Daniel Kasen, Jonas Lippuner, Dhruv Desai, and Luke F. Roberts. Dynamics, nucleosynthesis, and kilonova signature of black hole—neutron star merger ejecta. *Classical and Quantum Gravity*, 34:154001, August 2017. doi: 10.1088/1361-6382/aa7a77.

Rodrigo Fernández, Ben Margalit, and Brian D. Metzger. Nuclear-dominated accretion flows in two dimensions - II. Ejecta dynamics and nucleosynthesis for CO and ONe white dwarfs. *MNRAS*, 488(1):259–279, September 2019a. doi: 10.1093/mnras/stz1701.

Rodrigo Fernández, Alexander Tchekhovskoy, Eliot Quataert, Francois Foucart, and Daniel Kasen. Long-term GRMHD simulations of neutron star merger accretion discs: implications for electromagnetic counterparts. *MNRAS*, 482:3373–3393, Jan 2019b. doi: 10.1093/mnras/sty2932.

Rodrigo Fernández, Francois Foucart, and Jonas Lippuner. The landscape of disk outflows from black hole - neutron star mergers. *arXiv e-prints*, art. arXiv:2005.14208, May 2020.

Rodrigo Fernández, Sherwood Richers, Nicole Mulyk, and Steven Fahlman. Fast flavor instability in hypermassive neutron star disk outflows. *Phys. Rev. D*, 106(10):103003, November 2022. doi: 10.1103/PhysRevD.106.103003.

C. J. Fontes, C. L. Fryer, A. L. Hungerford, P. Hakel, J. Colgan, D. P. Kilcrease, and M. E. Sherrill. Relativistic opacities for astrophysical applications. *High Energy Density Physics*, 16:53–59, September 2015. doi: 10.1016/j.hedp.2015.06.002.

F. Foucart, M. D. Duez, L. E. Kidder, S. M. Nissanke, H. P. Pfeiffer, and M. A. Scheel. Numerical simulations of neutron star-black hole binaries in the near-equal-mass regime. *Phys. Rev. D*, 99(10):103025, May 2019. doi: 10.1103/PhysRevD.99.103025.

Francois Foucart, Evan O'Connor, Luke Roberts, Matthew D. Duez, Roland Haas, Lawrence E. Kidder, Christian D. Ott, Harald P. Pfeiffer, Mark A. Scheel, and Bela Szilagyi. Post-merger evolution of a neutron star-black hole binary with neutrino transport. *Phys. Rev. D*, 91(12):124021, June 2015. doi: 10.1103/PhysRevD.91.124021.

Francois Foucart, Matthew D. Duez, Francois Hebert, Lawrence E. Kidder, Harald P. Pfeiffer, and Mark A. Scheel. Monte-Carlo Neutrino Transport in Neutron Star Merger Simulations. *ApJ*, 902(1):L27, October 2020. doi: 10.3847/2041-8213/abbb87.

B. Fryxell, K. Olson, P. Ricker, F. X. Timmes, M. Zingale, D. Q. Lamb, P. MacNeice, R. Rosner, J. W. Truran, and H. Tufo. FLASH: An Adaptive Mesh Hydrodynamics Code for Modeling Astrophysical Thermonuclear Flashes. *ApJS*, 131:273–334, November 2000. doi: 10.1086/317361.

S. Fujibayashi, K. Kiuchi, N. Nishimura, Y. Sekiguchi, and M. Shibata. Mass Ejection from the Remnant of a Binary Neutron Star Merger: Viscous-radiation Hydrodynamics Study. *ApJ*, 860:64, June 2018. doi: 10.3847/1538-4357/aabafd.

Sho Fujibayashi, Yuichiro Sekiguchi, Kenta Kiuchi, and Masaru Shibata. Properties of Neutrino-driven Ejecta from the Remnant of a Binary Neutron Star Merger: Pure Radiation Hydrodynamics Case. *ApJ*, 846:114, September 2017. doi: 10.3847/1538-4357/aa8039.

Sho Fujibayashi, Masaru Shibata, Shinya Wanajo, Kenta Kiuchi, Koutarou Kyutoku, and Yuichiro Sekiguchi. Viscous evolution of a massive disk surrounding stellar-mass black holes in full general relativity. *Phys. Rev. D*, 102 (12):123014, December 2020a. doi: 10.1103/PhysRevD.102.123014.

Sho Fujibayashi, Masaru Shibata, Shinya Wanajo, Kenta Kiuchi, Koutarou Kyutoku, and Yuichiro Sekiguchi. Mass ejection from disks surrounding a low-mass black hole: Viscous neutrino-radiation hydrodynamics simulation in full general relativity. *Phys. Rev. D*, 101(8):083029, April 2020b. doi: 10.1103/PhysRevD.101.083029.

Sho Fujibayashi, Shinya Wanajo, Kenta Kiuchi, Koutarou Kyutoku, Yuichiro Sekiguchi, and Masaru Shibata. Postmerger Mass Ejection of Low-mass Binary Neutron Stars. *ApJ*, 901(2):122, October 2020c. doi: 10.3847/1538-4357/abafc2.

Sho Fujibayashi, Kenta Kiuchi, Shinya Wanajo, Koutarou Kyutoku, Yuichiro Sekiguchi, and Masaru Shibata. Comprehensive Study of Mass Ejection and Nucleosynthesis in Binary Neutron Star Mergers Leaving Short-lived Massive Neutron Stars. *ApJ*, 942(1):39, January 2023. doi: 10.3847/1538-4357/ac9ce0.

S. Goriely. Uncertainties in the solar system r-abundance distribution. *A&A*, 342:881–891, February 1999.

I. Hachisu. A Versatile Method for Obtaining Structures of Rapidly Rotating Stars. *ApJS*, 61:479, July 1986. doi: 10.1086/191121.

Matthias Hanauske, Kentaro Takami, Luke Bovard, Luciano Rezzolla, José A. Font, Filippo Galeazzi, and Horst Stöcker. Rotational properties of hypermassive neutron stars from binary mergers. *Phys. Rev. D*, 96:043004, August 2017. doi: 10.1103/PhysRevD.96.043004.

John F. Hawley. Global Magnetohydrodynamical Simulations of Accretion Tori. *ApJ*, 528(1):462–479, January 2000. doi: 10.1086/308180.

John F. Hawley and Steven A. Balbus. A Powerful Local Shear Instability in Weakly Magnetized Disks. II. Nonlinear Evolution. *ApJ*, 376:223, Jul 1991. doi: 10.1086/170271.

John F. Hawley and Julian H. Krolik. Global MHD Simulation of the In-

ner Accretion Disk in a Pseudo-Newtonian Potential. *ApJ*, 548(1):348–367, February 2001. doi: 10.1086/318678.

John F. Hawley and Julian H. Krolik. Magnetically Driven Jets in the Kerr Metric. *ApJ*, 641(1):103–116, April 2006. doi: 10.1086/500385.

Kota Hayashi, Sho Fujibayashi, Kenta Kiuchi, Koutarou Kyutoku, Yuichiro Sekiguchi, and Masaru Shibata. General-relativistic neutrino-radiation magnetohydrodynamic simulation of seconds-long black hole-neutron star mergers. *Phys. Rev. D*, 106(2):023008, July 2022. doi: 10.1103/PhysRevD.106.023008.

A. Heger, S. E. Woosley, and H. C. Spruit. Presupernova Evolution of Differentially Rotating Massive Stars Including Magnetic Fields. *ApJ*, 626(1): 350–363, June 2005. doi: 10.1086/429868.

J. Heinzel, M. W. Coughlin, T. Dietrich, M. Bulla, S. Antier, N. Christensen, D. A. Coulter, R. J. Foley, L. Issa, and N. Khetan. Comparing inclination-dependent analyses of kilonova transients. *MNRAS*, 502(2):3057–3065, April 2021. doi: 10.1093/mnras/stab221.

Fatemeh Hossein Nouri, Matthew D. Duez, Francois Foucart, M. Brett Deaton, Roland Haas, Milad Haddadi, Lawrence E. Kidder, Christian D. Ott, Harald P. Pfeiffer, Mark A. Scheel, and Bela Szilagyi. Evolution of the magnetized, neutrino-cooled accretion disk in the aftermath of a black hole-neutron star binary merger. *Phys. Rev. D*, 97(8):083014, April 2018. doi: 10.1103/PhysRevD.97.083014.

K. Hotokezaka, P. Beniamini, and T. Piran. Neutron Star Mergers as

sites of r-process Nucleosynthesis and Short Gamma-Ray Bursts. *preprint, arXiv:1801.01141*, January 2018.

Panagiotis Iosif and Nikolaos Stergioulas. Models of binary neutron star remnants with tabulated equations of state. *MNRAS*, 510(2):2948–2967, February 2022. doi: 10.1093/mnras/stab3565.

H. Thomas Janka and Andreas Bauswein. Dynamics and Equation of State Dependencies of Relevance for Nucleosynthesis in Supernovae and Neutron Star Mergers. *arXiv e-prints*, art. arXiv:2212.07498, December 2022. doi: 10.48550/arXiv.2212.07498.

O. Just, A. Bauswein, R. Ardevol Pulpillo, S. Goriely, and H.-T. Janka. Comprehensive nucleosynthesis analysis for ejecta of compact binary mergers. *MNRAS*, 448:541–567, March 2015. doi: 10.1093/mnras/stv009.

O. Just, S. Goriely, H. Th Janka, S. Nagataki, and A. Bauswein. Neutrino absorption and other physics dependencies in neutrino-cooled black hole accretion discs. *MNRAS*, 509(1):1377–1412, January 2022. doi: 10.1093/mnras/stab2861.

Oliver Just, Vimal Vijayan, Zewei Xiong, Andreas Bauswein, Stephane Goriely, Jérôme Guilet, Hans-Thomas Janka, and Gabriel Martínez-Pinedo. End-to-end kilonova models of neutron-star mergers with delayed black-hole formation. *arXiv e-prints*, art. arXiv:2302.10928, February 2023. doi: 10.48550/arXiv.2302.10928.

T. Kajino, W. Aoki, A. B. Balantekin, R. Diehl, M. A. Famiano, and G. J. Mathews. Current status of r-process nucleosynthesis.

Progress in Particle and Nuclear Physics, 107:109–166, July 2019. doi: 10.1016/j.ppnp.2019.02.008.

J. D. Kaplan, C. D. Ott, E. P. O'Connor, K. Kiuchi, L. Roberts, and M. Duez. The Influence of Thermal Pressure on Equilibrium Models of Hypermassive Neutron Star Merger Remnants. *ApJ*, 790:19, July 2014. doi: 10.1088/0004-637X/790/1/19.

D. Kasen, B. Metzger, J. Barnes, E. Quataert, and E. Ramirez-Ruiz. Origin of the heavy elements in binary neutron-star mergers from a gravitational-wave event. *Nature*, 551:80–84, November 2017. doi: 10.1038/nature24453.

Daniel Kasen, N. R. Badnell, and Jennifer Barnes. Opacities and Spectra of the r-process Ejecta from Neutron Star Mergers. *ApJ*, 774:25, September 2013. doi: 10.1088/0004-637X/774/1/25.

Daniel Kasen, Rodrigo Fernández, and Brian D. Metzger. Kilonova light curves from the disc wind outflows of compact object mergers. *MNRAS*, 450:1777–1786, June 2015. doi: 10.1093/mnras/stv721.

K. Kawaguchi, M. Shibata, and M. Tanaka. Radiative Transfer Simulation for the Optical and Near-infrared Electromagnetic Counterparts to GW170817. *ApJ*, 865:L21, October 2018. doi: 10.3847/2041-8213/aade02.

Kyohei Kawaguchi, Masaru Shibata, and Masaomi Tanaka. Diversity of Kilonova Light Curves. *ApJ*, 889(2):171, February 2020. doi: 10.3847/1538-4357/ab61f6.

Kyohei Kawaguchi, Sho Fujibayashi, Masaru Shibata, Masaomi Tanaka, and Shinya Wanajo. A Low-mass Binary Neutron Star: Long-term Ejecta Evo-

lution and Kilonovae with Weak Blue Emission. *ApJ*, 913(2):100, June 2021. doi: 10.3847/1538-4357/abf3bc.

Kyohei Kawaguchi, Sho Fujibayashi, Kenta Hotokezaka, Masaru Shibata, and Shinya Wanajo. Electromagnetic counterparts of binary-neutron-star mergers leading to a strongly magnetized long-lived remnant neutron star. *The Astrophysical Journal*, 933(1):22, jun 2022. doi: 10.3847/1538-4357/ac6ef7. URL `https://dx.doi.org/10.3847/1538-4357/ac6ef7`.

Kyohei Kawaguchi, Sho Fujibayashi, Nanae Domoto, Kenta Kiuchi, Masaru Shibata, and Shinya Wanajo. Kilonovae of binary neutron star mergers leading to short-lived remnant neutron star formation. *arXiv e-prints*, art. arXiv:2306.06961, June 2023. doi: 10.48550/arXiv.2306.06961.

K. Kiuchi, K. Kyutoku, and M. Shibata. Three-dimensional evolution of differentially rotating magnetized neutron stars. *PRD*, 86(6):064008, September 2012. doi: 10.1103/PhysRevD.86.064008.

Kenta Kiuchi, Sho Fujibayashi, Kota Hayashi, Koutarou Kyutoku, Yuichiro Sekiguchi, and Masaru Shibata. Self-consistent picture of the mass ejection from a one second-long binary neutron star merger leaving a short-lived remnant in general-relativistic neutrino-radiation magnetohydrodynamic simulation. *arXiv e-prints*, art. arXiv:2211.07637, November 2022. doi: 10.48550/arXiv.2211.07637.

Hannah Klion, Alexander Tchekhovskoy, Daniel Kasen, Adithan Kathirgamaraju, Eliot Quataert, and Rodrigo Fernández. The impact of r-process heating on the dynamics of neutron star merger accretion disc winds and their electromagnetic radiation. *MNRAS*, 510(2):2968–2979, February 2022. doi: 10.1093/mnras/stab3583.

Stefan M. Kolb, Matthias Stute, Wilhelm Kley, and Andrea Mignone. Radiation hydrodynamics integrated in the PLUTO code. *A&A*, 559:A80, November 2013. doi: 10.1051/0004-6361/201321499.

S. S. Komissarov. A Godunov-type scheme for relativistic magnetohydrodynamics. *MNRAS*, 303(2):343–366, February 1999. doi: 10.1046/j.1365-8711.1999.02244.x.

Oleg Korobkin, Ryan T. Wollaeger, Christopher L. Fryer, Aimee L. Hungerford, Stephan Rosswog, Christopher J. Fontes, Matthew R. Mumpower, Eve A. Chase, Wesley P. Even, Jonah Miller, G. Wendell Misch, and Jonas Lippuner. Axisymmetric Radiative Transfer Models of Kilonovae. *ApJ*, 910(2):116, April 2021. doi: 10.3847/1538-4357/abe1b5.

Christian J. Krüger and Francois Foucart. Estimates for disk and ejecta masses produced in compact binary mergers. *Phys. Rev. D*, 101(10):103002, May 2020. doi: 10.1103/PhysRevD.101.103002.

Takami Kuroda, Almudena Arcones, Tomoya Takiwaki, and Kei Kotake. Magnetorotational Explosion of a Massive Star Supported by Neutrino Heating in General Relativistic Three-dimensional Simulations. *ApJ*, 896(2):102, June 2020. doi: 10.3847/1538-4357/ab9308.

James M. Lattimer and Douglas F. Swesty. A generalized equation of state for hot, dense matter. *Nuclear Phys. A*, 535(2):331–376, December 1991. doi: 10.1016/0375-9474(91)90452-C.

Dongwook Lee. A solution accurate, efficient and stable unsplit staggered mesh scheme for three dimensional magnetohydrodynamics. *Journal of Computational Physics*, 243:269–292, Jun 2013. doi: 10.1016/j.jcp.2013.02.049.

Dongwook Lee and Anil E. Deane. An unsplit staggered mesh scheme for multidimensional magnetohydrodynamics. *Journal of Computational Physics*, 228(4):952–975, Mar 2009. doi: 10.1016/j.jcp.2008.08.026.

C. D. Levermore and G. C. Pomraning. A flux-limited diffusion theory. *ApJ*, 248:321–334, August 1981. doi: 10.1086/159157.

Li-Xin Li and Bohdan Paczyński. Transient Events from Neutron Star Mergers. *ApJ*, 507:L59–L62, November 1998. doi: 10.1086/311680.

Matthias Liebendörfer. A Simple Parameterization of the Consequences of Deleptonization for Simulations of Stellar Core Collapse. *ApJ*, 633(2):1042–1051, November 2005. doi: 10.1086/466517.

Matthias Liebendörfer, Anthony Mezzacappa, Friedrich-Karl Thielemann, O. E. Messer, W. Raphael Hix, and Stephen W. Bruenn. Probing the gravitational well: No supernova explosion in spherical symmetry with general relativistic Boltzmann neutrino transport. *Phys. Rev. D*, 63(10):103004, May 2001. doi: 10.1103/PhysRevD.63.103004.

J. Lippuner, R. Fernández, L. F. Roberts, F. Foucart, D. Kasen, B. D. Metzger, and C. D. Ott. Signatures of hypermassive neutron star lifetimes on r-process nucleosynthesis in the disc ejecta from neutron star mergers. *MNRAS*, 472: 904–918, November 2017. doi: 10.1093/mnras/stx1987.

Jonas Lippuner and Luke F. Roberts. r-process Lanthanide Production and Heating Rates in Kilonovae. *ApJ*, 815(2):82, December 2015. doi: 10.1088/0004-637X/815/2/82.

Jonas Lippuner and Luke F. Roberts. SkyNet: A Modular Nuclear Reaction

Network Library. *ApJS*, 233(2):18, December 2017. doi: 10.3847/1538-4365/aa94cb.

Federico G. Lopez Armengol, Zachariah B. Etienne, Scott C. Noble, Bernard J. Kelly, Leonardo R. Werneck, Brendan Drachler, Manuela Campanelli, Federico Cipolletta, Yosef Zlochower, Ariadna Murguia-Berthier, Lorenzo Ennoggi, Mark Avara, Riccardo Ciolfi, Joshua Faber, Grace Fiacco, Bruno Giacomazzo, Tanmayee Gupte, Trung Ha, Julian H. Krolik, Vassilios Mewes, Richard O'Shaughnessy, Jesús M. Rueda-Becerril, and Jeremy Schnittman. Handing off the outcome of binary neutron star mergers for accurate and long-term postmerger simulations. *Phys. Rev. D*, 106(8):083015, October 2022. doi: 10.1103/PhysRevD.106.083015.

A. Marek, H. Dimmelmeier, H. Th. Janka, E. Müller, and R. Buras. Exploring the relativistic regime with Newtonian hydrodynamics: an improved effective gravitational potential for supernova simulations. *A&A*, 445(1):273–289, January 2006. doi: 10.1051/0004-6361:20052840.

Ben Margalit and Brian D. Metzger. Time-dependent models of accretion discs with nuclear burning following the tidal disruption of a white dwarf by a neutron star. *MNRAS*, 461(2):1154–1176, September 2016. doi: 10.1093/mnras/stw1410.

Ben Margalit and Brian D. Metzger. The Multi-messenger Matrix: The Future of Neutron Star Merger Constraints on the Nuclear Equation of State. *ApJ*, 880(1):L15, July 2019. doi: 10.3847/2041-8213/ab2ae2.

B. D. Metzger and R. Fernández. Red or blue? A potential kilonova imprint of the delay until black hole formation following a neutron star merger. *MNRAS*, 441:3444–3453, July 2014. doi: 10.1093/mnras/stu802.

Brian D. Metzger. Kilonovae. *Living Reviews in Relativity*, 20:3, May 2017a. doi: 10.1007/s41114-017-0006-z.

Brian D. Metzger. Welcome to the Multi-Messenger Era! Lessons from a Neutron Star Merger and the Landscape Ahead. *arXiv e-prints*, art. arXiv:1710.05931, October 2017b. doi: 10.48550/arXiv.1710.05931.

Brian D. Metzger, Todd A. Thompson, and Eliot Quataert. A Magnetar Origin for the Kilonova Ejecta in GW170817. *ApJ*, 856:101, April 2018. doi: 10.3847/1538-4357/aab095.

Anthony Mezzacappa. Toward Realistic Models of Core Collapse Supernovae: A Brief Review. *IAU Symposium*, 362:215–227, January 2023. doi: 10.1017/S1743921322001831.

A. Mignone, T. Plewa, and G. Bodo. The Piecewise Parabolic Method for Multidimensional Relativistic Fluid Dynamics. *ApJS*, 160(1):199–219, Sep 2005. doi: 10.1086/430905.

A. Mignone, G. Bodo, S. Massaglia, T. Matsakos, O. Tesileanu, C. Zanni, and A. Ferrari. PLUTO: A Numerical Code for Computational Astrophysics. *ApJS*, 170(1):228–242, May 2007. doi: 10.1086/513316.

Andrea Mignone and Luca Del Zanna. Systematic construction of upwind constrained transport schemes for MHD. *arXiv e-prints*, art. arXiv:2004.10542, April 2020.

Jonah M. Miller, Benjamin R. Ryan, Joshua C. Dolence, Adam Burrows, Christopher J. Fontes, Christopher L. Fryer, Oleg Korobkin, Jonas Lippuner, Matthew R. Mumpower, and Ryan T. Wollaeger. Full transport model of

GW170817-like disk produces a blue kilonova. *Phys. Rev. D*, 100(2):023008, July 2019. doi: 10.1103/PhysRevD.100.023008.

Takahiro Miyoshi and Kanya Kusano. A multi-state HLL approximate Riemann solver for ideal magnetohydrodynamics. *Journal of Computational Physics*, 208(1):315–344, September 2005. doi: 10.1016/j.jcp.2005.02.017.

Elias R. Most, Antonios Nathanail, and Luciano Rezzolla. Electromagnetic Emission from Blitzars and Its Impact on Non-repeating Fast Radio Bursts. *ApJ*, 864(2):117, September 2018. doi: 10.3847/1538-4357/aad6ef.

Elias R. Most, L. Jens Papenfort, Samuel D. Tootle, and Luciano Rezzolla. On accretion discs formed in MHD simulations of black hole-neutron star mergers with accurate microphysics. *MNRAS*, 506(3):3511–3526, September 2021. doi: 10.1093/mnras/stab1824.

Philipp Mösta, Luke F. Roberts, Goni Halevi, Christian D. Ott, Jonas Lippuner, Roland Haas, and Erik Schnetter. r-process Nucleosynthesis from Three-dimensional Magnetorotational Core-collapse Supernovae. *ApJ*, 864 (2):171, September 2018. doi: 10.3847/1538-4357/aad6ec.

Philipp Mösta, David Radice, Roland Haas, Erik Schnetter, and Sebastiano Bernuzzi. A Magnetar Engine for Short GRBs and Kilonovae. *ApJ*, 901(2): L37, October 2020. doi: 10.3847/2041-8213/abb6ef.

Bernhard Müller, Hans-Thomas Janka, and Andreas Marek. A New Multidimensional General Relativistic Neutrino Hydrodynamics Code for Core-collapse Supernovae. II. Relativistic Explosion Models of Core-collapse Supernovae. *ApJ*, 756(1):84, September 2012. doi: 10.1088/0004-637X/756/1/84.

Ewald Müller and Matthias Steinmetz. Simulating self-gravitating hydrodynamic flows. *Computer Physics Communications*, 89(1):45–58, 1995. ISSN 0010-4655. doi: https://doi.org/10.1016/0010-4655(94)00185-5. URL https://www.sciencedirect.com/science/article/pii/0010465594001855. Numerical Methods in Astrophysical Hydrodynamics.

Vsevolod Nedora, Sebastiano Bernuzzi, David Radice, Boris Daszuta, Andrea Endrizzi, Albino Perego, Aviral Prakash, Mohammadtaher Safarzadeh, Federico Schianchi, and Domenico Logoteta. Numerical Relativity Simulations of the Neutron Star Merger GW170817: Long-term Remnant Evolutions, Winds, Remnant Disks, and Nucleosynthesis. *ApJ*, 906(2):98, January 2021. doi: 10.3847/1538-4357/abc9be.

David Neilsen, Steven L. Liebling, Matthew Anderson, Luis Lehner, Evan O'Connor, and Carlos Palenzuela. Magnetized neutron stars with realistic equations of state and neutrino cooling. *Phys. Rev. D*, 89(10):104029, May 2014. doi: 10.1103/PhysRevD.89.104029.

N. Nishimura, H. Sawai, T. Takiwaki, S. Yamada, and F. K. Thielemann. The Intermediate r-process in Core-collapse Supernovae Driven by the Magneto-rotational Instability. *ApJ*, 836(2):L21, February 2017. doi: 10.3847/2041-8213/aa5dee.

M. Obergaulinger and M. Á. Aloy. Magnetorotational core collapse of possible GRB progenitors - I. Explosion mechanisms. *MNRAS*, 492(4):4613–4634, March 2020. doi: 10.1093/mnras/staa096.

Evan O'Connor and Christian D. Ott. A new open-source code for spherically symmetric stellar collapse to neutron stars and black holes. *Classi-*

cal and Quantum Gravity, 27(11):114103, June 2010. doi: 10.1088/0264-9381/27/11/114103.

Evan P. O'Connor and Sean M. Couch. Two-dimensional Core-collapse Supernova Explosions Aided by General Relativity with Multidimensional Neutrino Transport. *ApJ*, 854(1):63, February 2018. doi: 10.3847/1538-4357/aaa893.

B. Paczyńsky and P. J. Wiita. Thick accretion disks and supercritical luminosities. *A&A*, 500:203–211, August 1980.

A. Perego, S. Rosswog, R. M. Cabezón, O. Korobkin, R. Käppeli, A. Arcones, and M. Liebendörfer. Neutrino-driven winds from neutron star merger remnants. *MNRAS*, 443:3134–3156, October 2014. doi: 10.1093/mnras/stu1352.

A. Perego, R. M. Cabezón, and R. Käppeli. An Advanced Leakage Scheme for Neutrino Treatment in Astrophysical Simulations. *ApJS*, 223(2):22, April 2016. doi: 10.3847/0067-0049/223/2/22.

A. Perego, F. K. Thielemann, and G. Cescutti. *r-Process Nucleosynthesis from Compact Binary Mergers*, pages 1–56. Springer Singapore, Singapore, 2020. ISBN 978-981-15-4702-7. doi: 10.1007/978-981-15-4702-7_13-1. URL `https://doi.org/10.1007/978-981-15-4702-7_13-1`.

Y. Z. Qian. Supernovae versus Neutron Star Mergers as the Major R-Process Sources. *ApJ*, 534(1):L67–L70, May 2000. doi: 10.1086/312659.

Geert Raaijmakers, Samaya Nissanke, Francois Foucart, Mansi M. Kasliwal, Mattia Bulla, Rodrigo Fernández, Amelia Henkel, Tanja Hinderer, Kenta Hotokezaka, Kamilė Lukosiūtė, Tejaswi Venumadhav, Sarah Antier, Michael W. Coughlin, Tim Dietrich, and Thomas D. P. Edwards. The Challenges Ahead

for Multimessenger Analyses of Gravitational Waves and Kilonova: A Case Study on GW190425. *ApJ*, 922(2):269, December 2021. doi: 10.3847/1538-4357/ac222d.

David Radice. Binary neutron star merger simulations with a calibrated turbulence model. *Symmetry*, 12(8), 2020. ISSN 2073-8994. doi: 10.3390/sym12081249. URL `https://www.mdpi.com/2073-8994/12/8/1249`.

David Radice and Sebastiano Bernuzzi. Ab-Initio General-Relativistic Neutrino-Radiation Hydrodynamics Simulations of Long-Lived Neutron Star Merger Remnants to Neutrino Cooling Timescales. *arXiv e-prints*, art. arXiv:2306.13709, June 2023. doi: 10.48550/arXiv.2306.13709.

David Radice, Albino Perego, Kenta Hotokezaka, Steven A. Fromm, Sebastiano Bernuzzi, and Luke F. Roberts. Binary Neutron Star Mergers: Mass Ejection, Electromagnetic Counterparts, and Nucleosynthesis. *The Astrophysical Journal*, 869(2):130, 2018. doi: 10.3847/1538-4357/aaf054.

David Radice, Sebastiano Bernuzzi, and Albino Perego. The dynamics of binary neutron star mergers and gw170817. *Annual Review of Nuclear and Particle Science*, 70(1):95–119, 2020. doi: 10.1146/annurev-nucl-013120-114541. URL `https://doi.org/10.1146/annurev-nucl-013120-114541`.

David Radice, Sebastiano Bernuzzi, Albino Perego, and Roland Haas. A new moment-based general-relativistic neutrino-radiation transport code: Methods and first applications to neutron star mergers. *MNRAS*, 512(1):1499–1521, May 2022. doi: 10.1093/mnras/stac589.

M. Rampp and H. T. Janka. Radiation hydrodynamics with neutrinos. Variable

Eddington factor method for core-collapse supernova simulations. *A&A*, 396: 361–392, December 2002. doi: 10.1051/0004-6361:20021398.

M. Reichert, M. Obergaulinger, M. Eichler, M. Á. Aloy, and A. Arcones. Nucleosynthesis in magneto-rotational supernovae. *MNRAS*, 501(4):5733–5745, March 2021. doi: 10.1093/mnras/stab029.

S. Richers, D. Kasen, E. O'Connor, R. Fernández, and C. D. Ott. Monte Carlo Neutrino Transport through Remnant Disks from Neutron Star Mergers. *ApJ*, 813:38, November 2015. doi: 10.1088/0004-637X/813/1/38.

Sherwood Richers, Hiroki Nagakura, Christian D. Ott, Joshua Dolence, Kohsuke Sumiyoshi, and Shoichi Yamada. A Detailed Comparison of Multidimensional Boltzmann Neutrino Transport Methods in Core-collapse Supernovae. *ApJ*, 847(2):133, October 2017. doi: 10.3847/1538-4357/aa8bb2.

Marko Ristic, Richard O'Shaughnessy, V. Ashley Villar, Ryan T. Wollaeger, Oleg Korobkin, Chris L. Fryer, Christopher J. Fontes, and Atul Kedia. Interpolated kilonova spectra models: necessity for a phenomenological, blue component in the fitting of AT2017gfo spectra. *arXiv e-prints*, art. arXiv:2304.06699, April 2023. doi: 10.48550/arXiv.2304.06699.

S. Rosswog and O. Korobkin. Heavy elements and electromagnetic transients from neutron star mergers. *arXiv e-prints*, art. arXiv:2208.14026, August 2022. doi: 10.48550/arXiv.2208.14026.

S. Rosswog and M. Liebendörfer. High-resolution calculations of merging neutron stars - II. Neutrino emission. *MNRAS*, 342(3):673–689, Jul 2003. doi: 10.1046/j.1365-8711.2003.06579.x.

M. Ruffert, H. T. Janka, and G. Schaefer. Coalescing neutron stars - a step towards physical models. I. Hydrodynamic evolution and gravitational-wave emission. *A&A*, 311:532–566, July 1996.

M. Ruffert, H.-T. Janka, K. Takahashi, and G. Schaefer. Coalescing neutron stars - a step towards physical models. II. Neutrino emission, neutron tori, and gamma-ray bursts. *A&A*, 319:122–153, March 1997.

B. R. Ryan, J. C. Dolence, and C. F. Gammie. bhlight: General Relativistic Radiation Magnetohydrodynamics with Monte Carlo Transport. *ApJ*, 807 (1):31, July 2015. doi: 10.1088/0004-637X/807/1/31.

Takayoshi Sano, Shu ichiro Inutsuka, Neal J. Turner, and James M. Stone. Angular momentum transport by magnetohydrodynamic turbulence in accretion disks: Gas pressure dependence of the saturation level of the magnetorotational instability. *The Astrophysical Journal*, 605(1):321, apr 2004. doi: 10.1086/382184. URL `https://dx.doi.org/10.1086/382184`.

A. S. Schneider, L. F. Roberts, and C. D. Ott. Open-source nuclear equation of state framework based on the liquid-drop model with Skyrme interaction. *prc*, 96(6):065802, December 2017. doi: 10.1103/PhysRevC.96.065802.

A. S. Schneider, C. Constantinou, B. Muccioli, and M. Prakash. Akmal-Pandharipande-Ravenhall equation of state for simulations of supernovae, neutron stars, and binary mergers. *prc*, 100(2):025803, August 2019. doi: 10.1103/PhysRevC.100.025803.

N. I. Shakura and R. A. Sunyaev. Black holes in binary systems. Observational appearance. *A&A*, 24:337–355, 1973.

M. Shibata and Y. Sekiguchi. Radiation Magnetohydrodynamics for Black Hole-Torus System in Full General Relativity: A Step toward Physical Simulation. *Progress of Theoretical Physics*, 127(3):535–559, March 2012. doi: 10.1143/PTP.127.535.

M. Shibata, S. Fujibayashi, K. Hotokezaka, K. Kiuchi, K. Kyutoku, Y. Sekiguchi, and M. Tanaka. Modeling GW170817 based on numerical relativity and its implications. *Phys. Rev. D*, 96(12):123012, December 2017. doi: 10.1103/PhysRevD.96.123012.

Masaru Shibata and Kenta Hotokezaka. Merger and mass ejection of neutron star binaries. *Annual Review of Nuclear and Particle Science*, 69(1):41–64, 2019. doi: 10.1146/annurev-nucl-101918-023625. URL `https://doi.org/10.1146/annurev-nucl-101918-023625`.

Masaru Shibata, Yu-Ichiro Sekiguchi, and Rohta Takahashi. Magnetohydrodynamics of Neutrino-Cooled Accretion Tori around a Rotating Black Hole in General Relativity. *Progress of Theoretical Physics*, 118(2):257–302, August 2007. doi: 10.1143/PTP.118.257.

Masaru Shibata, Sho Fujibayashi, Kota Hayashi, Kenta Kiuchi, and Shinya Wanajo. Mass ejection from neutron-star mergers. *Proceedings of the International Astronomical Union*, 16(S362):190–202, 2020. doi: 10.1017/S1743921322001351.

Masaru Shibata, Sho Fujibayashi, and Yuichiro Sekiguchi. Long-term evolution of a merger-remnant neutron star in general relativistic magnetohydrodynamics: Effect of magnetic winding. *Phys. Rev. D*, 103(4):043022, February 2021a. doi: 10.1103/PhysRevD.103.043022.

Masaru Shibata, Sho Fujibayashi, and Yuichiro Sekiguchi. Long-term evolution of neutron-star merger remnants in general relativistic resistive magnetohydrodynamics with a mean-field dynamo term. *Phys. Rev. D*, 104(6):063026, September 2021b. doi: 10.1103/PhysRevD.104.063026.

D. M. Siegel, R. Ciolfi, and L. Rezzolla. Magnetically Driven Winds from Differentially Rotating Neutron Stars and X-Ray Afterglows of Short Gamma-Ray Bursts. *ApJ*, 785:L6, April 2014. doi: 10.1088/2041-8205/785/1/L6.

Daniel M. Siegel. GW170817 -the first observed neutron star merger and its kilonova: Implications for the astrophysical site of the r-process. *European Physical Journal A*, 55(11):203, November 2019. doi: 10.1140/epja/i2019-12888-9.

Daniel M. Siegel. r-Process nucleosynthesis in gravitational-wave and other explosive astrophysical events. *Nature Reviews Physics*, 4(5):306–318, April 2022. doi: 10.1038/s42254-022-00439-1.

Daniel M. Siegel and Brian D. Metzger. Three-dimensional GRMHD Simulations of Neutrino-cooled Accretion Disks from Neutron Star Mergers. *ApJ*, 858:52, May 2018. doi: 10.3847/1538-4357/aabaec.

Daniel M. Siegel, Jennifer Barnes, and Brian D. Metzger. Collapsars as a major source of r-process elements. *Nature*, 569(7755):241–244, May 2019. doi: 10.1038/s41586-019-1136-0.

M. Aaron Skinner and Eve C. Ostriker. The Athena Astrophysical Magnetohydrodynamics Code in Cylindrical Geometry. *ApJS*, 188(1):290–311, May 2010. doi: 10.1088/0067-0049/188/1/290.

Nikolaos Stergioulas and John L. Friedman. Comparing Models of Rapidly Rotating Relativistic Stars Constructed by Two Numerical Methods. *ApJ*, 444:306, May 1995. doi: 10.1086/175605.

James M. Stone, James E. Pringle, and Mitchell C. Begelman. Hydrodynamical non-radiative accretion flows in two dimensions. *MNRAS*, 310(4):1002–1016, Dec 1999. doi: 10.1046/j.1365-8711.1999.03024.x.

K. Takahashi, M. F. El Eid, and W. Hillebrandt. Beta transition rates in hot and dense matter. *A&A*, 67(2):185–197, July 1978.

M. Tanaka et al. Kilonova from post-merger ejecta as an optical and near-Infrared counterpart of GW170817. *PASJ*, 69:102, December 2017. doi: 10.1093/pasj/psx121.

Masaomi Tanaka and Kenta Hotokezaka. Radiative Transfer Simulations of Neutron Star Merger Ejecta. *ApJ*, 775:113, October 2013. doi: 10.1088/0004-637X/775/2/113.

N. R. Tanvir et al. The Emergence of a Lanthanide-rich Kilonova Following the Merger of Two Neutron Stars. *ApJ*, 848:L27, October 2017. doi: 10.3847/2041-8213/aa90b6.

Alexander Tchekhovskoy, Ramesh Narayan, and Jonathan C. McKinney. Efficient generation of jets from magnetically arrested accretion on a rapidly spinning black hole. *MNRAS*, 418(1):L79–L83, November 2011. doi: 10.1111/j.1745-3933.2011.01147.x.

F. X. Timmes and F. D. Swesty. The Accuracy, Consistency, and Speed of an Electron-Positron Equation of State Based on Table Interpolation

of the Helmholtz Free Energy. *ApJS*, 126:501–516, February 2000. doi: 10.1086/313304.

Gábor Tóth. The $\nabla\cdot$ B=0 Constraint in Shock-Capturing Magnetohydrodynamics Codes. *Journal of Computational Physics*, 161(2):605–652, July 2000. doi: 10.1006/jcph.2000.6519.

P. Tzeferacos, M. Fatenejad, N. Flocke, G. Gregori, D. Q. Lamb, D. Lee, J. Meinecke, A. Scopatz, and K. Weide. FLASH magnetohydrodynamic simulations of shock-generated magnetic field experiments. *High Energy Density Physics*, 8(4):322–328, Dec 2012. doi: 10.1016/j.hedp.2012.08.001.

V. A. Villar, J. Guillochon, E. Berger, B. D. Metzger, P. S. Cowperthwaite, M. Nicholl, K. D. Alexander, P. K. Blanchard, R. Chornock, T. Eftekhari, W. Fong, R. Margutti, and P. K. G. Williams. The Combined Ultraviolet, Optical, and Near-infrared Light Curves of the Kilonova Associated with the Binary Neutron Star Merger GW170817: Unified Data Set, Analytic Models, and Physical Implications. *ApJ*, 851:L21, December 2017a. doi: 10.3847/2041-8213/aa9c84.

V. Ashley Villar, Edo Berger, Brian D. Metzger, and James Guillochon. Theoretical Models of Optical Transients. I. A Broad Exploration of the Duration-Luminosity Phase Space. *ApJ*, 849(1):70, Nov 2017b. doi: 10.3847/1538-4357/aa8fcb.

T. A. Weaver, G. B. Zimmerman, and S. E. Woosley. Presupernova evolution of massive stars. *ApJ*, 225:1021–1029, November 1978. doi: 10.1086/156569.

Leonardo R. Werneck, Zachariah B. Etienne, Ariadna Murguia-Berthier, Roland Haas, Federico Cipolletta, Scott C. Noble, Lorenzo Ennoggi, Fed-

erico G. Lopez Armengol, Bruno Giacomazzo, Thiago Assumpção, Joshua Faber, Tanmayee Gupte, Bernard J. Kelly, and Julian H. Krolik. Addition of tabulated equation of state and neutrino leakage support to Illinois-GRMHD. *Phys. Rev. D*, 107(4):044037, February 2023. doi: 10.1103/PhysRevD.107.044037.

Christopher J. White, James M. Stone, and Charles F. Gammie. An Extension of the Athena++ Code Framework for GRMHD Based on Advanced Riemann Solvers and Staggered-mesh Constrained Transport. *ApJS*, 225(2):22, August 2016. doi: 10.3847/0067-0049/225/2/22.

J. R. Wilson, R. Couch, S. Cochran, J. Le Blanc, and Z. Barkat. Neutrino flow and the collapse of stellar cores. In P. G. Bergman, E. J. Fenyves, and L. Motz, editors, *Seventh Texas Symposium on Relativistic Astrophysics*, volume 262, pages 54–64, October 1975. doi: 10.1111/j.1749-6632.1975.tb31420.x.

C. Winteler, R. Käppeli, A. Perego, A. Arcones, N. Vasset, N. Nishimura, M. Liebendörfer, and F. K. Thielemann. Magnetorotationally Driven Supernovae as the Origin of Early Galaxy r-process Elements? *ApJ*, 750(1):L22, May 2012. doi: 10.1088/2041-8205/750/1/L22.

S. E. Woosley, A. Heger, and T. A. Weaver. The evolution and explosion of massive stars. *Reviews of Modern Physics*, 74(4):1015–1071, November 2002. doi: 10.1103/RevModPhys.74.1015.

Meng-Ru Wu, Rodrigo Fernández, Gabriel Martínez-Pinedo, and Brian D. Metzger. Production of the entire range of r-process nuclides by black hole accretion disc outflows from neutron star mergers. *Monthly Notices of the*

Royal Astronomical Society, 463(3):2323–2334, 08 2016. ISSN 0035-8711. doi: 10.1093/mnras/stw2156. URL https://doi.org/10.1093/mnras/stw2156.